UNIVERSITA' DEGLI STUDI DI TORINO
SCUOLA DI DOTTORATO IN SCIENZE NATURALI
DOTTORATO IN FISICA ED ASTROFISICA

Study of the η meson transitions from $\Upsilon(4S)$ and $\Upsilon(5S)$ with the Belle Experiment

- Version 1 -

Relatore

Prof. Ezio Menichetti

Candidato

Umberto Tamponi

Correlatore

Dott. Roberto Mussa

December 2014

Contents

Chapter 1

The Belle Experiment at the KEKB collider

The term "B-factory" is used to denote a high luminosity e^+e^- collider with center of mass energy $\sqrt{s} \approx 10.580$ GeV/c^2 and asymmetric beam energy [1]. This type of accumulation ring was conceptually developed in the late 1980's in order to study the time-dependent CP violation effects in the B meson system. So far two $B-$factories have collected data, $KEKB$ at the KEK laboratory located in Tsukuba, Japan [2], and the $PEP-II$ complex at SLAC, USA [3]. In this chapter we will briefly describe the physical motivation that lead to the construction of these complexes and we will focus on the description of the KEKB accumulation ring, where the Belle experiment was located [1].

1.1 The $B-$factories

The e^+e^- colliders operating with a center-of-mass (CM) energy in the bottomonium region, ranging typically from 9.4 GeV to 11 GeV, have played a dominant role in the study of the CP-parity violating effects in

---

[1] For a more complete historical introduction, see [1]

the B meson system since the late 1980's.
Among all the bottomonium states that, having quantum numbers 1^{--}, can be directly produced in e^+e^- collisions, the $\Upsilon(4S)$ is located only 20 MeV above the threshold for the $B\bar{B}$ pair production and its dominant decay mechanism is the OZI-allowed process $\Upsilon(4S) \to B\bar{B}$ [2]. This reaction is characterized by a very low momentum transfer Q^2, thus the B mesons are produced coherently and almost at rest in the $\Upsilon(4S)$ reference frame. The advantages of the experiments at e^+e^- colliders with respect to the one hadronic machines, like HERA-B [4], are evident if we consider that there is no underlying event activity in the process $e^+e^- \to B\bar{B}$, that the background due to the QED process $e^+e^- \to q\bar{q}$, with $q = (u, d, s, c)$ can be greatly reduced by reconstructing one B meson in one of its dominant decay modes, and that the complete reconstruction of one of the B mesons allows to study the decay modes involving ν or, more generally, weakly or non-interacting particles like light dark matter candidates. On the other hand it must be noticed that the B meson production in pp collisions at high rapidity occur with large cross section, thus experiments located at hadronic colliders, like LHCb at the LHC [5], are able to collect much larger B meson samples.

The simultaneous violation of both the charge (C) and parity (P) symmetries, the CP violation (CPV), was first observed in the K^0 meson system in 1964 [6]. The theory describing these effects, developed in different stages by N.Cabibbo, M. Kobayashi and T. Maskawa (CKM theory)[7, 8], describes the mixing between different quark flavors in terms of an unitary, 3×3 matrix whose action is to transform the mass eigenstates $|d>$

---

[2] In the B meson sector the isospin violation is very small and, unlike what is observed in the D meson systems, the B^+B^- and $B^0\bar{B}^0$ threshold are almost degenerate. For the same reason the production rate of neutral and charged B is almost equal.

$, |s>, |b>$ into the weak interaction eigenstates $|d'>, |s'>, |b'>$:

$$\begin{pmatrix} u' \\ d' \\ s' \end{pmatrix} = V_{CKM} \begin{pmatrix} u \\ d \\ s \end{pmatrix} = \begin{pmatrix} V_{ud} & V_{us} & V_{ub} \\ V_{cd} & V_{cs} & V_{cb} \\ V_{td} & V_{ts} & V_{tb} \end{pmatrix} \begin{pmatrix} u \\ d \\ s \end{pmatrix}.$$

The elements of the CKM matrix are in general complex numbers whose squared module $|V_{qq'}|^2$ represent the probability of the transition $q \to q'$. The unitarity of V_{CKM} implies the validity of the relations:

$$\begin{gathered}
\frac{V^*_{ud}V_{cd}}{V^*_{us}V_{cs}} + \frac{V^*_{ub}V_{cb}}{V^*_{us}V_{cs}} + 1 = 0 \\
\frac{V^*_{ud}V_{td}}{V^*_{us}V_{ts}} + \frac{V^*_{ub}V_{tb}}{V^*_{us}V_{ts}} + 1 = 0 \\
\frac{V^*_{cd}V_{td}}{V^*_{cs}V_{ts}} + \frac{V^*_{cb}V_{tb}}{V^*_{cs}V_{ts}} + 1 = 0 \\
\frac{V_{ud}V^*_{us}}{V_{cd}V^*_{cs}} + \frac{V_{td}V^*_{ts}}{V_{cd}V^*_{cs}} + 1 = 0 \\
\frac{V_{td}V^*_{tb}}{V_{cd}V^*_{cb}} + \frac{V_{ud}V^*_{ub}}{V_{cd}V^*_{cb}} + 1 = 0 \\
\frac{V_{us}V^*_{ub}}{V_{cs}V^*_{cb}} + \frac{V_{ts}V^*_{tb}}{V_{cs}V^*_{cb}} + 1 = 0,
\end{gathered} \tag{1.1}$$

each one of whose can be represented on the imaginary plane as a triangle, called *unitary triangle*. As a consequence, the nine elements $V_{qq'}$ cannot be all independent from each other and V_{CKM} can be re-parametrized as function of 3 angles θ_{12}, θ_{13}, and θ_{23}, and one phase δ responsible for the CP violation. Our understanding of the CPV is thus intimately connected with the assumption that V_{CKM} is unitary. Experimentally, the unitarity test can be carried measuring the sides and the angles of each unitarity triangle, the latter ones being proportional to the phase of the ratios present in the unitarity relations.

Not all the unitary triangles, however, can be easily measured. Indeed V_{CKM} is nearly diagonal, and a hierarchy among the elements of V_{CKM} is observed with $s_{13} << s_{23} << s_{12} << 1$. An alternative parametrization of the V_{CKM} matrix, known as Wolfenstein parametrization [9], highlights this hierarchy. Instead of θ_{12}, θ_{13}, and θ_{23}, and one phase δ, it uses the four independent parameters A, ρ, η and $\lambda = \sin\theta_{12} = 0.22$, where θ_{12} is the Cabibbo angle responsible for the $u - s$ mixing. Since $\theta_{12} << 1$, a power expansion in terms of this parameter is possible obtaining:

$$V_{CKM} = \begin{pmatrix} 1-\lambda^2/2 & \lambda & A\lambda^3(\rho - i\eta) \\ -\lambda & 1-\lambda^2/2 & A\lambda^2 \\ A\lambda^3(1-\rho-i\eta) & -A\lambda^2 & 1 \end{pmatrix} + \mathcal{O}(\lambda^4).$$

Using this parametrization to re-write the unitarity constraints, it appears clear that only two unitary triangles, the second and the fifth, have all the sides of the same order and are not degenerate:

$$\begin{aligned} \frac{V^*_{ud}V_{cd}}{V^*_{us}V_{cs}} / \frac{V^*_{ub}V_{cb}}{V^*_{us}V_{cs}} &\approx \mathcal{O}(\lambda^{-4}) \\ \frac{V^*_{ud}V_{td}}{V^*_{us}V_{ts}} / \frac{V^*_{ub}V_{tb}}{V^*_{us}V_{ts}} &\approx \mathcal{O}(1) \\ \frac{V^*_{cd}V_{td}}{V^*_{cs}V_{ts}} / \frac{V^*_{cb}V_{tb}}{V^*_{cs}V_{ts}} &\approx \mathcal{O}(\lambda^{2}) \\ \frac{V_{ud}V^*_{us}}{V_{cd}V^*_{cs}} / \frac{V_{td}V^*_{ts}}{V_{cd}V^*_{cs}} &\approx \mathcal{O}(\lambda^{-4}) \\ \frac{V_{td}V^*_{tb}}{V_{cd}V^*_{cb}} / \frac{V_{ud}V^*_{ub}}{V_{cd}V^*_{cb}} &\approx \mathcal{O}(1) \\ \frac{V_{us}V^*_{ub}}{V_{cs}V^*_{cb}} / \frac{V_{ts}V^*_{tb}}{V_{cs}V^*_{cb}} &\approx \mathcal{O}(\lambda^{2}). \end{aligned} \tag{1.2}$$

The validity of the fifth unitarity relation, in particular, can be tested by measuring the Cabibbo mixing angle and the CP violation effects in the B meson sector [3]. The study of this relation become so important during

---

[3] In the early 1980's A.I. Sanda, A.R. Carter and I.I. Bigi highlighted that a large $B^0 - \bar{B}^0$ mixing rate could be connected with large CP- violation effects, of the order of 10%, few orders of magnitude larger than the effects observed in the Kaon sector, leading to a non degenerate unitarity triangle. The CP violation in B thus become one of the most important subjects for the test of the CKM theory. Thanks to a first generation of experiments at

time that it is the unitarity triangle par excellence (Figure 1.1), and the measurement of its angles $\phi_1 = arg(-\frac{V_{cd}V_{cb}^*}{V_{td}V_{tb}^*})$, $\phi_2 = arg(-\frac{V_{td}V_{tb}^*}{V_{ud}V_{ub}^*})$ and $\phi_3 = arg(-\frac{V_{ud}V_{ub}^*}{V_{cd}V_{cb}^*})$ become one of the fundamental tests of the CKM model [4].

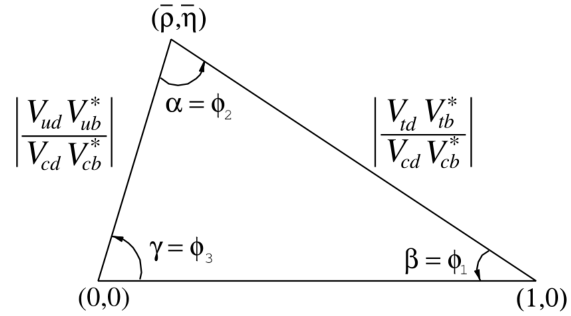

Figure 1.1: The unitary triangle.

We will now briefly review the strategy adopted for the measurement of ϕ_1, ϕ_2 and ϕ_3 [1, 10], showing how it determined all the main aspect of the B-factories and their detectors .

To measure ϕ_1 both the B meson resulting from $\Upsilon(4S) \to B^0\bar{B^0}$ decays msu be reconstructed, one in the CP violating final state, s_{CP}, and one in a final states that allows to determine the original flavor of the B, s_{tag}. With both the B fully reconstructed, the decay rate for the s_{CP} production can be written as:

$$\mathcal{P}(\Delta t, q; \mathcal{S}, \mathcal{A}) = \frac{e^{-|\Delta t|/\tau_{B0}}}{4\tau_{B^0}}(1 + q(\mathcal{S}\sin(\Delta m_d \Delta t) + \mathcal{A}\cos(\Delta m_d \Delta t))),$$

where Δt is the difference between the proper time of B_{CP} and B_{tag}, $q = \pm 1$ is determined by the flavor of B_{tag}, Δm_d and τ_{B^0} are respectively the mixing frequency and the lifetime of the B^0, and finally $\mathcal{A}$ and $\mathcal{S}$ are the amplitudes corresponding to direct and indirect CP- violation. Since in

---

e^+e^- colliders, first ARGUS at DORIS-II (DESY), then CLEO at CERS (Cornell), a large mixing rate between B^0 and $\bar{B^0}$ was observed, an a new generation of experiments become necessary in order to measure the angles of the unitarity triangle in the B meson sector.

[4] We use for the angles of the CKM matrix the naming convention used by the Belle collaboration. An alternative convention is $\alpha = \phi_2$, $\beta = \phi_1$, $\gamma = \phi_3$.

$B \to (c\bar{c})K$ decays $\mathcal{S} \propto \sin(2\phi_2)$ and a measurement of the transition rate would lead to the measurement of ϕ_1, the golden mode for this analysis was identified in the $B^0 \to J/\psi K^0$ process.

The requirement of a precise measure of Δt was one of the major drivers for the design of the $B-$ factories. Experimentally, this time can be deduced by the B decay length, i.e. from the distance between the production vertex and the decay vertex, therefore the main experimental challenge for the measurement of the B meson proper time is the ability to precisely identify and measure displaced vertexes in the event. In the $\Upsilon(4S)$ reference frame the average B meson flight path is $c\tau = 1.5 \cdot 10^{-12}$ m, well below the typical tracking precision archieved with the technology available when the $B-$factories where proposed. Therefore the B vertex were not distinguishable from the primary one if the $\Upsilon(4S)$ was produced at rest in the laboratory frame. The proposed solution was to produce the $B\bar{B}$ system in a boosted frame, with the result shown in Figure 1.2: the boost magnifies the paths in the laboratory frame, making them measurable with a sufficient precision. This is the reason why a typical feature of the B-factories is large energy asymmetry between the two colliding beams, with a consequent boost between the frame of the e^+e^- pair and the laboratory frame. Both PEP-II and KEKB had $E_{e^-} \approx 2E_{e^+}$.

In order to measure ϕ_2, processes involving the $b \to u$ transition are needed. The golden mode for the measurement of ϕ_2 was identified in the $B^0 \to \pi^+\pi^-$ decay which, despite the simple topology, suffers from significant background due to the continuum $e+e- \to q\bar{q}$, which is likely to produce back-to-back, high momentum tracks. Furthermore the process $B^0 \to K^+\pi^-$, occurring with a branching ratio almost four times larger than $B^0 \to \pi^+\pi^-$, can fake the signal when a $K^\pm$ is mis-identified as pion. In order to mitigate the first background an hermetic detector, capable of

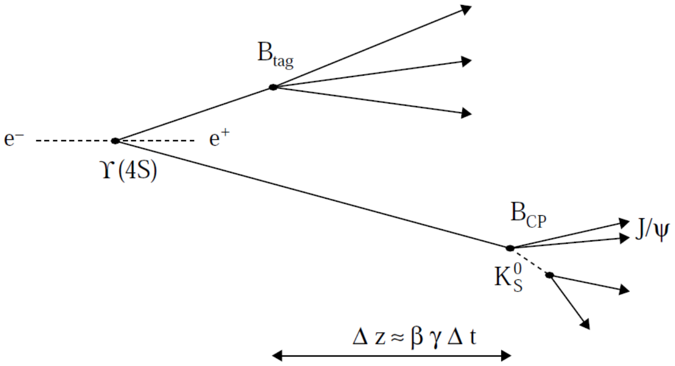

Figure 1.2: Topology of a $B \to J7\psi K^0$ event, with two displaced vertexes separated by a distance proportional to Δt.

precisely reconstruct the global event shape [5], is needed, while in order to reduce the second background an high K/π separation power is required.

Finally, the measurement of ϕ_3 requires to study the interference between $b \to \bar{u}cd$ and $b \to u\bar{c}d$ amplitudes. This can be archieved by studying the CP asymmetries in $B^\pm \to DK^\pm$, tagging the charge of the B meson sing the information of the $K^\pm$ and reconstructing the D meson in the same final state for both B^- and B^+. Different methods have been proposed in order to perform this measurement, either by reconstructing the $D \to K^+K^-$ modes or the $D \to K^-\pi^+$. Both methods require to collect a large data sample in order to obtain a significant measurements: in the first case the CP asymmetry effects are expected to be rather small, while in the second case, where large CP asymmetries are expected, Cabibbo-suppressed transition are always involved and thus the total branching fraction for the process is low. An high luminosity accelerator was therefore needed.

Even without exploring further the physics program of the $B-$ factories, the measurements of the tree angles of the unitary triangle already

---

[5] A more extensive discussion of the even shape observables and their usage for the rejection of the continuum events will be presented in chapter 3

determined all the mandatory features for this kind of complexes:

- A high luminosity, e^+e^- collider with $\sqrt{s} \approx 10.6$ GeV/c and asymmetric beam energies.
- A Detector with large solid angle coverage, needed for the full reconstruction of the $B^0\bar{B}^0$ pairs. Due to the asymmetry between the beam energies, this requirement was satisfied introducing a Forward/Backward asymmetry in the detector geometry.
- High precision tracking capabilities, in order to precisely measure the B meson decay vertex displacement with respect to the primary vertex [6]
- Precise particle identification over a broad range of transverse momenta, with a specific focus on the K/π separation, in order to identify the flavor of the B_{tag} and reduce the peaking backgrounds due to mis-reconstructed B decay modes.
- Electromagnetic calorimetry, in order to provide supplemental information for the $J/\psi \to e^+e^-$ events and for the reconstruction of photons.
- μ and K_L identification system.

1.2 The KEKB accelerator complex

The KEKB complex [2, 11], sketched in Figure 1.3, was an high-luminosity electron-positron collider located at the KEK (High Energy Accelerator Research Organization) consisting in a 600 m long linear accelerator (LINAC) connected with two storage rings. Electron and positron bunches were accelerated by the LINAC and then injected into the two separated rings;

---

[6] Herein, we will call primary vertex the position of the e^+e^- collision.

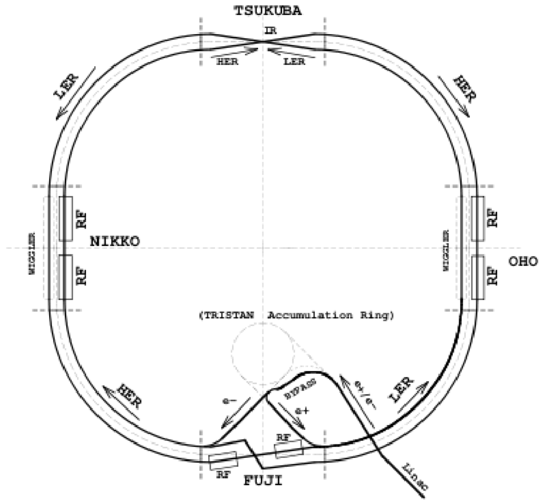

Figure 1.3: The KEKB accelerator complex

since the bunches acceleration was performed only by the LINAC, the injection could proceed continuously minimizing the detector dead time. During the Belle data taking the two beams were kept at different energies, providing non symmetric collisions; the electrons were injected in the High Energy Ring (HER) at the energy of $E_{HER} \approx 8$ GeV, while the positrons were injected in the Low Energy Ring (LER) with an energy of $E_{LER} \approx 3.5$ GeV. KEKB was able to provide collision at energies in the CM frame ranging from 9.4 to 11 GeV, keeping a constant boost between the CM and the laboratory frame. Table 1.1 summarizes the energies of the HER and LER beams used during the Belle experiment to provide different $\sqrt{s}$. Both the HER and LER energies were changed when changing $\sqrt{s}$ in order to keep the center-of-mass boost at the constant value of $\beta_{CM} = 0.39$.

After the injection three groups of radio-frequency cavities (two placed along the HER, one along the LER) were used to sustain the energy of the beams.

In order to avoid parasitic collisions and keep the beam background as

Table 1.1: HER and LER energies

$\sqrt{s}$ [GeV]	Resonance	HER energy [GeV]	LER energy [GeV]
9.4603	$\Upsilon(1S)$	7.1511	3.1286
10.023	$\Upsilon(2S)$	7.5750	3.3141
10.355	$\Upsilon(3S)$	7.8262	3.4240
10.579	$\Upsilon(4S)$	7.9988	3.4995
10.860	$\Upsilon(5S)$	8.2150	3.5941

low as possible the two beams had a crossing angle of 22 $mrad$ in the zy (horizontal) plane [12]. This choice has a problematic consequence for a high-luminosity experiment: a non-zero crossing angle between the two beams involves a reduction of the luminosity, which is maximum for head-on collisions. This problem was solved with a particular technology called *crab cavities* [13]. A group of special radio-frequencies cavities capable to provide transverse fields was installed near the interaction point: its effect was to rotate the beam bunches and provide the head-on collision despite the finite crossing angle between the lines. Figure 1.4 illustrates how the crab cavities work and how they effects the bunches' orientation. With this technology the total integrated luminosity delivered by the KEKB reached in June 2010 the 1000 fb^{-1} (Fig. 1.5), 711 fb^{-1} were taken with $\sqrt{s}$ =

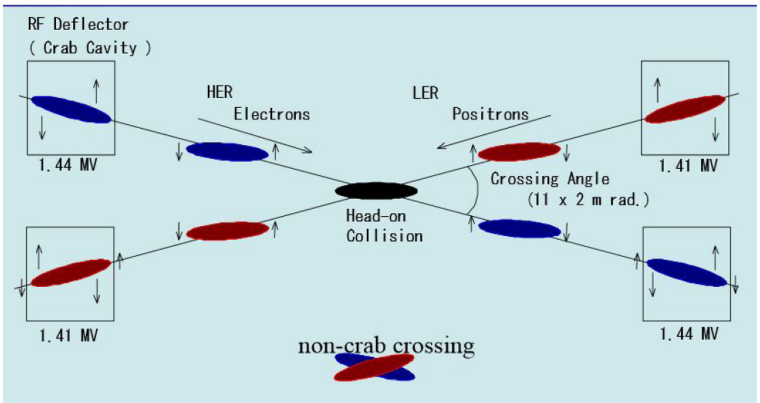

Figure 1.4: Crab collision scheme.

10.579 GeV/c^2, while the remaining 289 fb^{-1} at the energies of the other bottomonia states, obtaining the world largest sample of $\Upsilon(1S)$, $\Upsilon(2S)$, $\Upsilon(5S)$ and $e^+e^- \to q\bar{q}$ continuum.

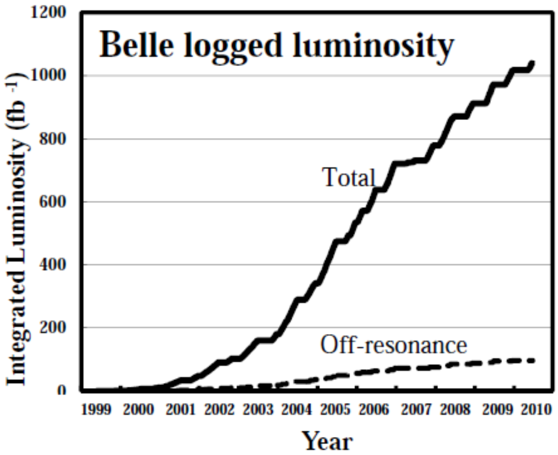

Figure 1.5: Evolution of the integrated luminosity collected by the Belle experiment.

1.3 The Belle Detector

The Belle Detector [14] was a cilindrical 4π multi-purpose spectrometer. It was divided into tree sections: a main central region (Barrel), located at mid-rapidity with respect to the interaction point, and two octagonal endcaps that extended the particle identification (PID) and calorimetric capabilities in the high rapidity region. The total angular coverage of the apparatus was 4π in the azimuthal angle ϕ, defined as the rotation angle along the beam axis, and between 17° and 150° in the polar angle θ.

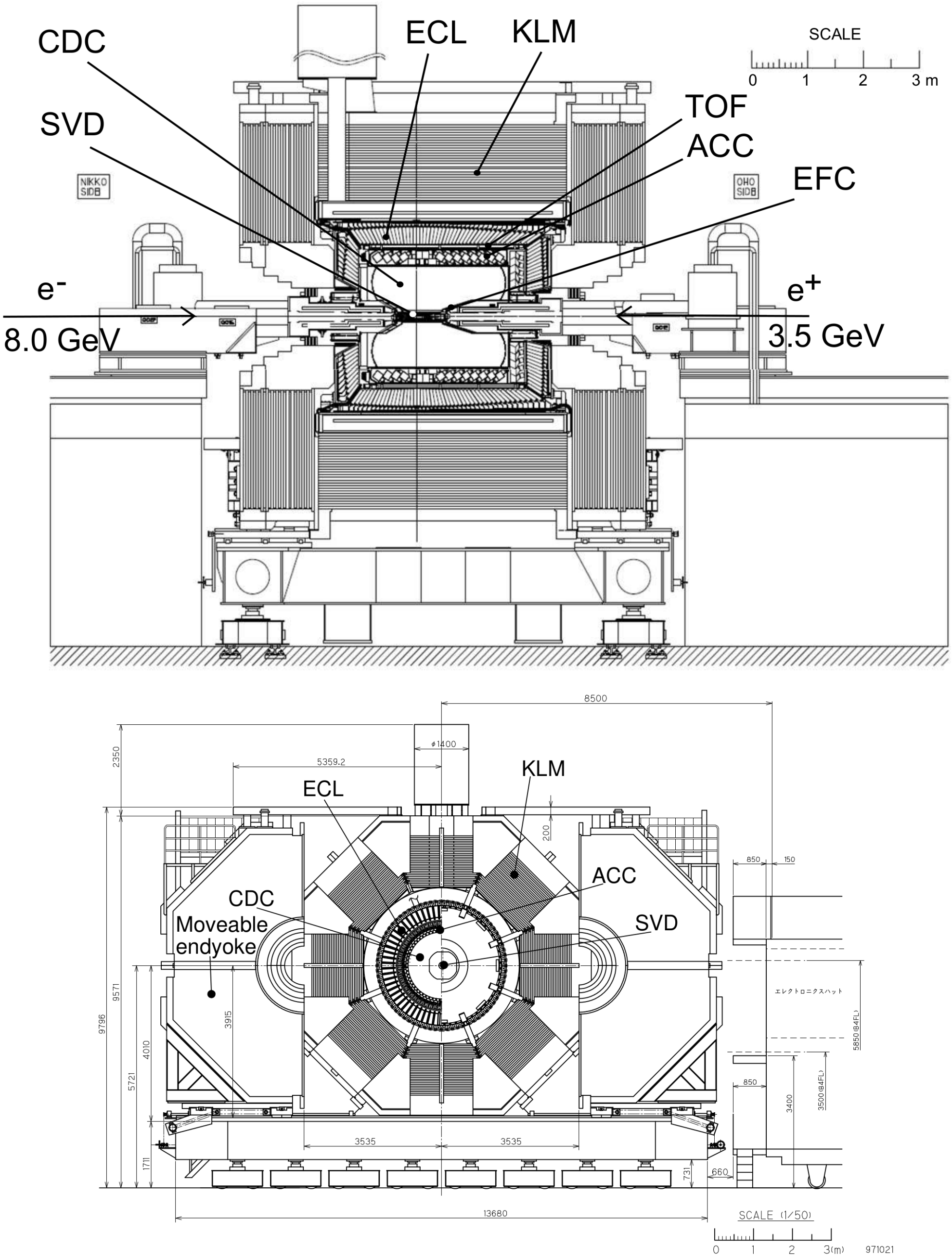

Figure 1.6: Belle detector layout

The tracking was performed by two sub-detector systems in a magnetic field parallel to the beam axis: a silicon vertex detector (SVD) located close to the beam pipe, surrounded by a large gas-filled drift chamber (CDC) able to provide information on both the particle's direction and their specific ionization. Two PID-dedicated detectors were arranged around the CDC: a time of flight counter (TOF) made with two layers of fast scintillators in the Barrel region and a Cherenkov threshold counter (ACC) which used aerogel tiles as radiator. The latter one was installed in the Forward and Backward end-caps as well. The photon and electron reconstruction was performed by an electromagnetic calorimeter (ECL) made of NaI(Tl) crystals and covering both the barrel and the two end-caps regions. A superconducting solenoid, providing a $1.5T$ magnetic field was located outside the ECL, while the μ and K_L reconstruction was performed by a system of RPC included in the iron return joke of the magnet (KLM). For a brief time, an extreme forward calorimeter (EFC) was installed to increase the ECL angular coverage.

1.3.1 Beam pipe and Silicon Vertex Detector

The innermost part of the Belle Detector, consisting in a low-Z beam pipe and a silicon-based tracking system (Silicon Vertex Detector, or SVD) underwent to major modification in the middle of the data taking period. The two phases are commonly denoted as SVD1 and SVD2 phases. During the first phase, which lasted from 1999 to 2003, a 20mm radius, double wall beryllium beam pipe was installed around the interaction point. A 10μm-thick gold coating was added to the inner wall in order to absorb the synchrotron radiation arising from the beams and prevent it to reach the innermost layer of the SVD. The SVD itself (shown in Figure 1.7) consisted in 3 layers of double-sided silicon strips (DSSD) arranged in a barrel-only geometry, with a polar angular coverage $23^\circ < \theta < 140^\circ$, smaller than the outer detector acceptance. The first layer of the detector was located at 30 mm from the interaction point, while the most external one was at 60mm from the IP.

The resolution on the impact parameter σ_{ip} reconstructed with a multilayer detector strongly depends on the ratio or the outer to the inner layer radii r_1 and r_2:

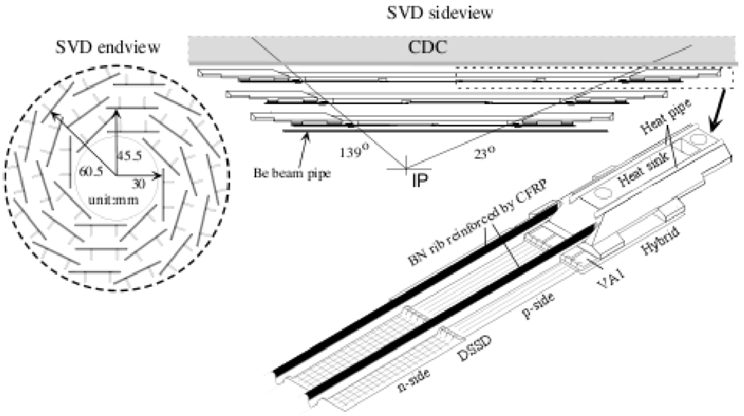

Figure 1.7: The Belle silicon vertex detector with the SVD1 configuration

$$\sigma_{ip} \propto \frac{\sqrt{1+\frac{r_1^2}{r_2^2}}}{1-\frac{r_1}{r_2}};$$

these considerations, together with the need for a more radiation-hard design and a larger angular coverage, lead to a radical modification of the SVD after four years of operation. A new beam pipe, with same geometry but reduced radius, was installed, and the SVD1 was replaced with a new detector (SVD2) consisting in 4 DSSD layers located at 20 mm, 44mm, 70 mm and 88mm from the interaction point, all of them covering the whole nominal detector acceptance (Figure 1.8). Thanks to the new geometry, a reduction of r_{in}/r_{ext} from 0.50 to 0.23 was obtained, significantly improving the impact parameter resolution. The electronics readout went as well under radical modification. The original VA chips produced in 1.2μm CMOS technology, capable of tolerate a 200krad dose, were replaced after one year of operation with a version in 0.8μm CMOS in order to archieve

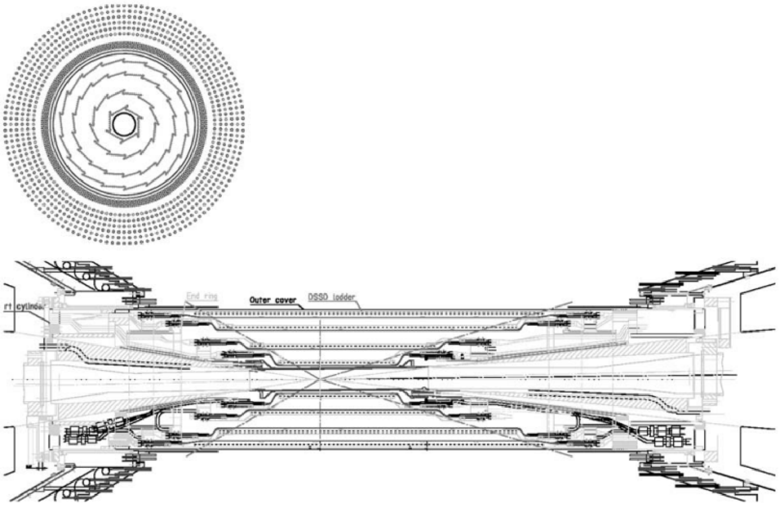

Figure 1.8: Upgraded SVD layout

stronger radiation tolerance (up to 1Mrad). In 2003 the dose accumulated in the first layer reached 900krad, and together with the replacement of the SVD1 with SVD2, the VA chips were replaced with the newer VA1TA, capable of resist up to 20Mrad. The new chips granted a faster signal shaping and a reduced dead time. Thanks to the constantly increasing instantaneous luminosity of the KEKB accelerator, at the end of the data taking only 15% of the data had been taken with the SVD1 configuration. The standard Belle MC simulation accounts for this changes in the tracking performances and reconstruction efficiency The performance in the impact parameter reconstruction is a function of the pseudo-momentum of the track, for both the z direction and the xy plane, as shown in Figure 1.9.

1.3.2 Central Drift Chamber

The Central Drift Chamber (CDC) was a gas-filled wire chamber. Wire were arranged in 50 super-layers, each one comprising from three to six either axial or stereo layers and three cathode strip layers, for a total of 8400 drift cells. In order to maximize the acceptance the CDC structure was asymmetric (Fig. 1.10), with a conical shape studied to keep the detector as close as possible to the interaction point. Having an inner radius of 88mm (increased to 103.55 mm after 2003 to provide the necessary space for the SVD2), the CDC was the main tracking apparatus in any kinematic range of interest for the experiment, with the SVD providing mainly additional information for the vertexing rather complementary tracking in the low transverse momentum region. Both the devices were operated in a 1.5T magnetic field. In addition to providing three dimensional reconstruction of the charge particle trajectories, the CDC was also designed to measure their specific ionization and thus contribute to the particle identification and to provide a fasts track reconstruction used by the global trigger logic.

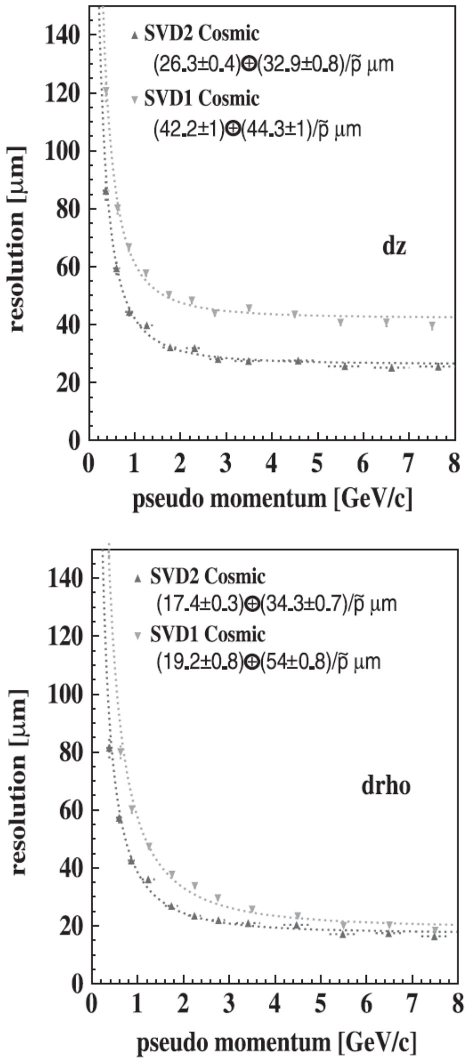

Figure 1.9: SVD performances in impact parameter measure. Top: z-axis direction; Bottom: xy plane. The triangles (circles) represent the resolution obtained with SVD 1.5 (2.0).

The gas mixture was chosen in order to minimize the coulomb scattering and the radiation absorption: the chosen 50% helium - 50% ethane mixture offered a long

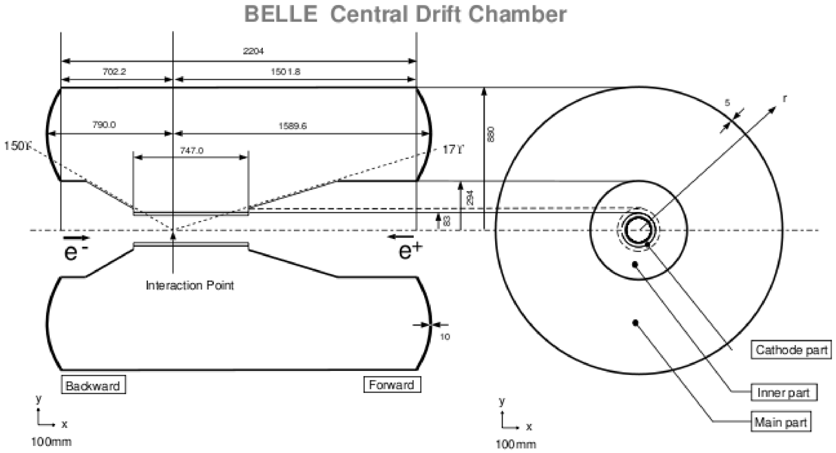

Figure 1.10: The Belle CDC

radiation length (640 m) and a velocity drift that saturates at the value of 4 $cm/\mu m$ with an electric field of 1.6 $kV/(cm \cdot atm)$.

The momentum resolution of the CDC has been measured with cosmic rays, obtaining the distribution shown in figure 1.11. The large ethane component provided a good dE/dx resolution (Fig. 1.12), estimated with beam tests to be 5.2% for 3.5 GeV/c pions. The dE/dx information contributes to the likelihoods used for the particle identification.

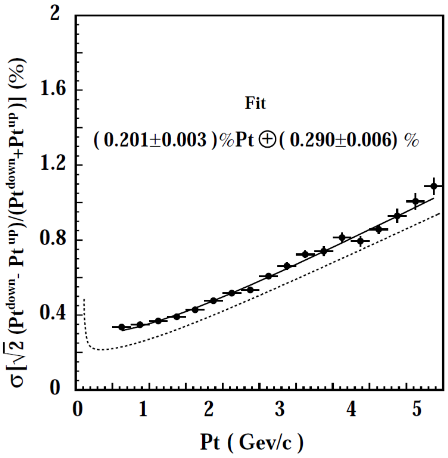

Figure 1.11: Transverse momentum resolution of the Belle drift chamber.

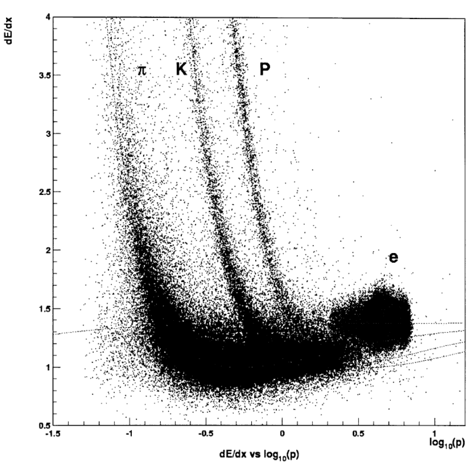

Figure 1.12: Specific ionization as function of the track momenutm in the Belle CDC, from beam data.

1.3.3 Aerogel counter and Time of flight detector

An Aerogel Cherenkov Counter System (ACC) and a Time Of Flight detector (TOF) were placed between the CDC and the electromagnetic calorimeter, as shown in Figure 1.13. The ACC system, consisting in 960 modules of hydrophobic aerogel with refraction index between 1.01 and 1.03, was optimized in order to separate kaons from pions in the range not covered by the dE/dx information. The TOF consisted in a 4 cm thick fast scintillator layer, with a time resolution of 100 ps for particle with momentum below 1.2 GeV/c. A layer of 0.5 cm thick scintillator (TSC) was used as coincidence system in order to avoid noise from accidental counts (Fig. 1.14). The TOF system is used as part of the trigger system for the other subsystems.

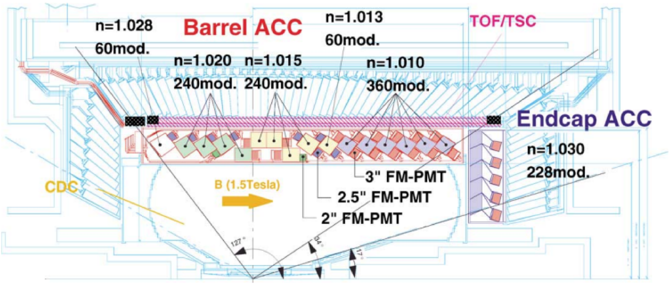

Figure 1.13: The Belle Aerogel counter.

The inner radius of the ACC was 0.880 m, so only particles with transverse momentum $p_t > 398$ MeV/c could reach this section of the detector.

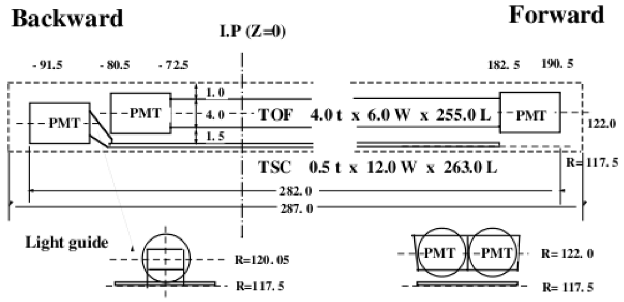

Figure 1.14: The Belle Time of Flight detector.

1.3.4 The electromagnetic calorimeter

The Belle Electromagnetic Calorimeter (ECL) was divided into three sections, the barrel and the two end-caps ("forward" and "backward" with respect to the HER beam direction). The total coverage is 91% of the solid angle, with a 3% of acceptance loss due to the gaps between barrel and end-caps that provides the pathway for the cabling system of the inner detectors. The ECL consisted in 8736 CsI(Tl) crystals with a typical dimension of (55x55)mm on the front face and 30 cm of depth, equivalent to 16.2 radiation lengths, arranged to point approximately to the primary verted region (Fig. 1.15) . The size of the crystals was arranged in such a way that approximately 80% of the total energy of a photon injected in its center remained contained in the crystal. The energy resolution studies were performed with electrons and photon beams, using 3x3 (Fig. 1.17) and 5x5 (Fig. 1.16) crystal blocks.

The energy resolution shape can be fitted with the quadratic sum of three terms obtaining, for a 5x5 block:

$$\frac{\sigma_E}{E} = \frac{0.0066(\%)}{E} + \frac{1.53(\%)}{E^{1/4}} + 1.18(\%).$$

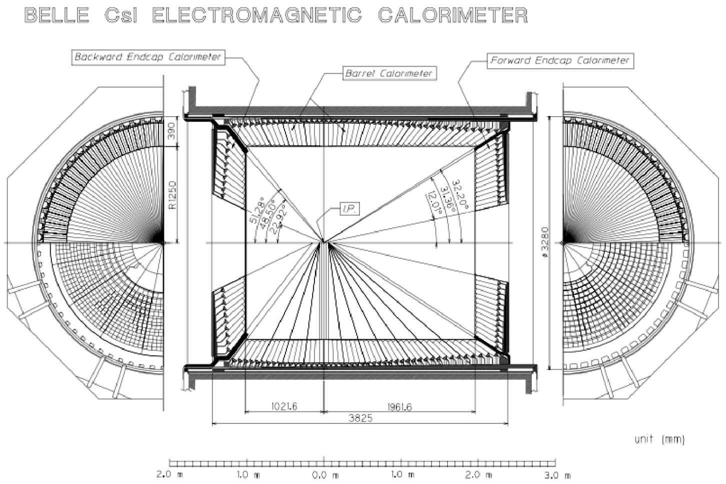

Figure 1.15: The Belle Calorimeter

For a 3x3 block the parameters are different but the functional form is the same:

$$\frac{\sigma_E}{E} = \frac{0.066(\%)}{E} + \frac{0.81(\%)}{E^{1/4}} + 1.34(\%)$$

The photon reconstruction algorithm uses both the 5X5 and 3X3 block information.

In addition to photon reconstruction, the ECL was used as luminosity monitoring detector by counting the rate of Bhabha events.

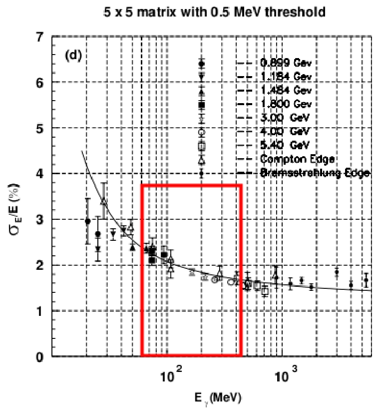

Figure 1.16: ECL energy resolution using a 5x5 block of crystals

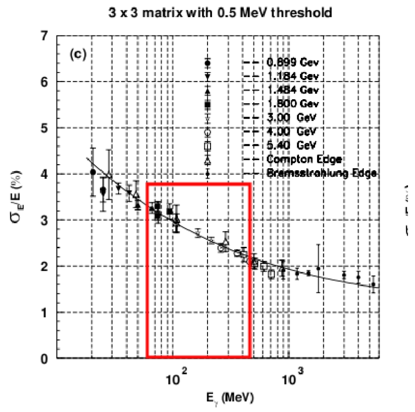

Figure 1.17: ECL energy resolution using a 3x3 block of crystals

The ECL resolution in measuring the invariant mass of photon pairs is a crucial feature in the study of transitions involving the η reconstruction. Figures 1.18 and 1.19 show the invariant mass distribution of reconstructed π^0's and η's in hadronic events, where the photon energy is required to be greater than 30 MeV/c^2.

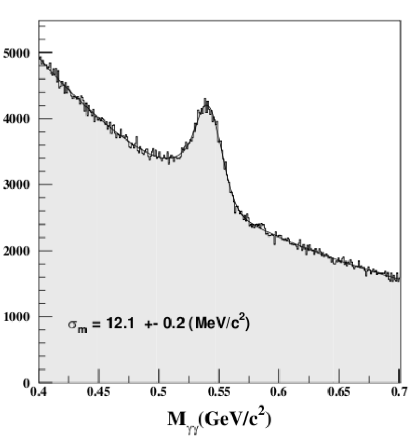

Figure 1.18: $\gamma\gamma$ pairs invariant mass in the η region, from hadronic events

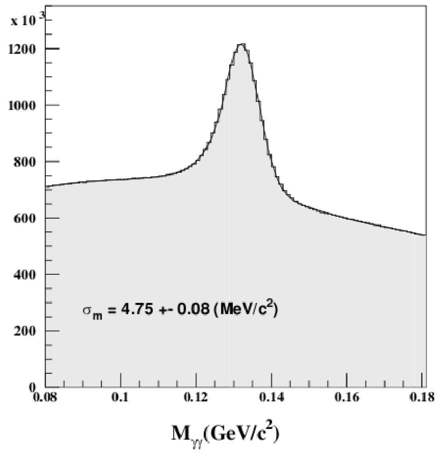

Figure 1.19: $\gamma\gamma$ pairs invariant mass in the π^0 region, from hadronic events

1.3.5 Kaons and Muons detection system

The KLM consists in alternating layers of charged particle detectors and 4.7 *cm*-thick iron plates, with a total absorption length or 3.9 interaction lengths.

The detection of charged particles is provided by a glass-electrode-resistive plate chambers, arranged in double layers called super-layers as shown in figure 1.20.

The KLM performances in muon detection were studied with cosmic rays with momentum greater than 500 MeV/c, since particles with lower momentum produced in the IP can not reach the KLM due to the presence of the 1.5 T magnetic field. The pions were selected from $K_s \to \pi^+\pi^-$

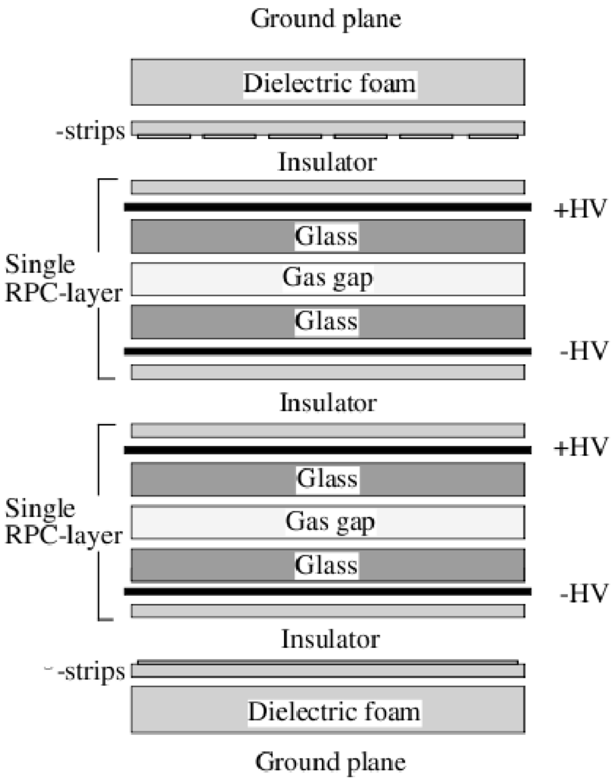

Figure 1.20: The Belle Kaon and Muon detector

events in e^+e^- collisions. For muon with momentum above 1.5 GeV/c the identification efficiency is over 90% and the fake rate is less than 5%.

1.4 Particle identification

The particle identification is performed combining the time of flight measured by the TOF, the Cherenkov light yield measured by the ACC, the specific ionization measured by the CDC and, eventually, the energy deposited in the ECL and the signal left by the track in the KLM sistem. Instead of absolute probability, the Belle PID classification for hadrons is based on binary likelihood ratios. Likelihood functions $\mathcal{L}_\alpha$ for different mass hypotheses α are calculated from the physical quantities measured by the PID subsystems accounting for the direction and momentum of the track, and then combined in the likelihood ratios

$$\mathcal{R}_{\alpha:\beta} = \frac{\mathcal{L}_{\alpha}^{TOF}\mathcal{L}_{\alpha}^{ACC}\mathcal{L}_{\alpha}^{CDC}}{\mathcal{L}_{\alpha}^{TOF}\mathcal{L}_{\alpha}^{ACC}\mathcal{L}_{\alpha}^{CDC} + \mathcal{L}_{\beta}^{TOF}\mathcal{L}_{\beta}^{ACC}\mathcal{L}_{\beta}^{CDC}}$$

where α and β are two mass assumpions. By construction $\mathcal{R}_{\alpha:\beta} \approx 1$ if α is the correct assumption and $\mathcal{R}_{\alpha:\beta} \approx 0$ if β is the correct assumption. For example, the tipical requirement for pion identification is $\mathcal{R}_{\pi:K} > 0.6$ and $\mathcal{R}_{\pi:p} > 0.6$.

For electrons and muons the strategy is slightly different, since only one binary ratio is constructed:

$$\mathcal{R}_{\mu,e} = \frac{\mathcal{L}_{\mu,e}}{\mathcal{L}_{\mu,e} + \mathcal{L}_{had}},$$

where $\mathcal{L}_{had} = \mathcal{L}_{\pi} + \mathcal{L}_{K} + \mathcal{L}_{p}$ and in $\mathcal{L}_{\mu,e}$ is included also the information provided by either the KLM for muons or the ECL for electrons. The performances of the PID logic are reported in Figure 1.21

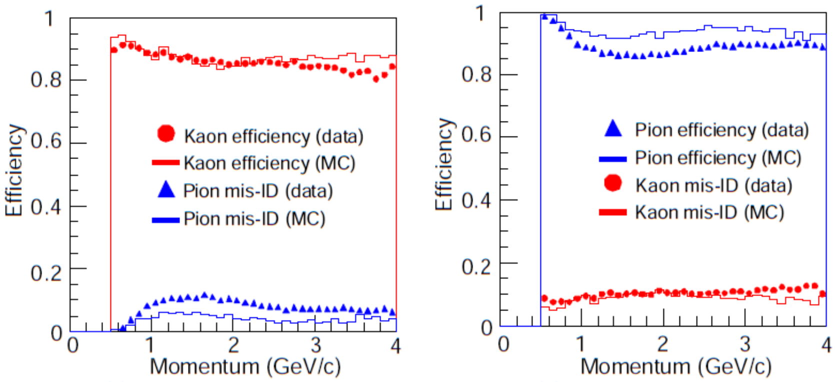

(a) Kaon identification. (b) Pion identification.

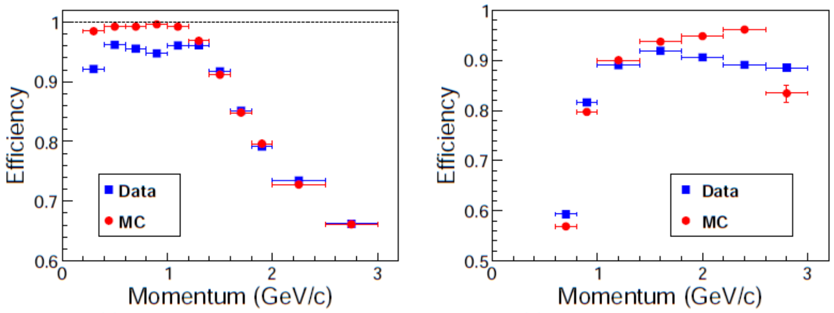

(c) Proton identification. (d) Electron identification.

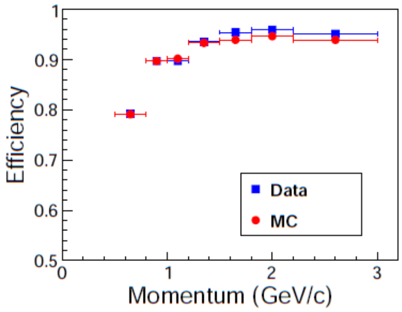

(e) Muon identification

Figure 1.21: Summary of the PID performance of the Belle Experiment.

1.5 Data taking conditions and data samples

The Belle datasets are divided into *experiments*, each one lasting several months and including data taken at different energies. Between one experiment and the following, a major shutdown for either maintenance or upgrades occurred. Each experiment is further divided into *runs*, each one lasting from few minutes to few hours and comprising events recorded at a single beam energy. When a data acquisition (DAQ) error or a beam dump occurred, the run was stopped and a new one was started. The datasets devoted to physics studies can be divided into three general categories: *scan*, *on-resonance* and *continuum*. *On-resonance* data are taken on the peak of one of the bottomonium resonances, and represent roughly 90% of the total events. In order to fine-tune the beam energy around the resonant peak position, a short *scan* was performed. The beam energy was changed by few tens of MeV around the nominal position to determine the maximum of the hadronic cross section, identified as the optimal data taking point. Furthermore physics-dedicated scans were performed in the region between the $\Upsilon(4S)$ and the $\Upsilon(6S)$ changing the beam energy by either 100-MeV or 10-MeV wide steps, in order to measure the hadronic cross section in this region. Finally for each data taking period on resonance a set of *continuum* data, usually consisting in $\approx$ 10% of the corresponding *on-resonance* sample, was taken lowering the CM energy by 60 MeV in order to allow the study of the $q\bar{q}$ background. During the periods in which the beams were not available, cosmic ray events were recorded for calibration and alignment purposes.

The luminosity integrated by Belle is summarized in Table 1.2

Table 1.2: Summary of the integrated luminosity collected by the Belle experiment, in units of fb^{-1}. The data taken for brief scans or machine studies are not reported.

Energy region	*on-resonance*	*continuum*	Physics *scan*
$\Upsilon(1S)$	5.7	1.2	
$\Upsilon(2S)$	24.9	1.7	
$\Upsilon(3S)$	2.9	0.2	
$\Upsilon(4S)$	702.6	89.4	
$\Upsilon(5S)$	121.1	1.7	
$\Upsilon(5S)$-$\Upsilon(6S)$ scan			27.6

Chapter 2

Bottomonium

In this chapter we will give an overview of the physics of the heavy quark bound states, generally called quarkonia, with a specific focus on the most recent developments in the bottomonium sector. We will start with a short review of the basic properties of the theory of strong interactions, the *quantum chromodynamics* [15], and we will show how these properties determine the shape of the QCD non-relativistic potential used in the description of quarkonia. In the second section we will then give an overview of the basic bottomonium properties as they can be deduced from a naive potential model, with a particular focus on the energy levels and the relevance of the relativistic corrections. The final part is devoted to the most recent developments, both theoretical and experimental, that revived this sector of particle physics making it a new and fertile frontier for the study of low-energy QCD [16, 17]. After discussing the discovery of new states that do not fit either the predicted spectra and cannot even be described as pure $Q\bar{Q}$ bound states, we will focus on the problems faced by our experimental search: the puzzle of the hadronic transitions, the role of the Heavy quark spin symmetry in bottomonium, and the interpretation of the hyperfine splittings in the $1P$ and $1S$ levels.

2.1 Basic properties of Quantum Chromodynamics

The *quark model* was introduced by Gell-Man [18] and Zweig [19, 20] to describe the recurrences in the mass spectra of the hadrons known in the middle 1960s. Hadron were supposed to be composed of fundamental fermions with fractional charge, the quarks, each on having a new quantum number, the *flavor*. In this scheme the hadrons obey a symmetry, partially broken by the mass difference between the three quarks, based on the $SU(3)$ group.

The theory of the interaction among these new fundamental particles is the quantum chromodynamics (QCD) , whose basic properties can be inferred by some experimental observations.

Since the processes dominated by the strong interaction were observed to occur on a timescale of the order of the electromagnetic ones, it is reasonable to assume that the mediator for such interaction is a massless boson. However, unlike QED, one single *charge* is not enough to explain the properties of hadrons. Indeed in the quark constituent model the Δ^{++} baryon, whose spin is $3/2$, is interpreted as a bound state of 3 quarks u with same spin alignment, therefore the total wave-function of the three quarks is completely symmetric, which is forbidden for 3 identical fermions by the Fermi principle. In order to make the wave-function completely anti-symmetric, an additional degree of freedom was introduced, the *color*, an equivalent of the electric charge for strong interaction. The minimal number of colors required to antisimmetrize the Δ^{++} wave-function is three, therefore the underlying symmetry of the QCD must be $SU(3)$ and not simply $U(1)$ as happens in the case of QED. This $SU(3)_{\text{color}}$ symmetry is a perfect symmetry of the theory, and must not be confused with the $SU(3)_{\text{flavor}}$ accidental symmetry introduced by the quark model for the low mass hadrons. The full QCD Lagrangian can be written as

$$\mathcal{L}_{QCD} = \sum_f \bar{q}_f (i\not{D} - m_f) q_f - \frac{1}{4} G^a_{\mu\nu} G^{a\mu\nu},$$

Where q_f are six massive Dirac fields representing the six quarks, each one having mass m_f, $\not{D}$ is the covariant derivative containing the coupling between quarks an the gauge fields and $\frac{1}{4} G^a_{\mu\nu} G^{a\mu\nu}$ controls the dynamic of the gluonic fields only. The covariant derivative depends on the gluon fields A_μ, which is representable as a 3x3 matrix, as

$$\not{D} = \gamma^\mu (\partial_\mu - igA_\mu),$$

where g is a coupling constant. Since the underling symmetry of the QCD is $SU(3)$, in total 8 gluonic fields are present, each one corresponding to one generator of the $SU(3)$ group which can be represented by the Gell-Mann matrices λ^a, so that $A_\mu = \frac{1}{2} \sum_{a=1}^{8} A^a_\mu \lambda^a$. While in the QED Lagrangian the photon is neutral and interacts only with charged particles, the gluons are colored objects that can interact with themselves, originating purely gluonic vertexes. This is perhaps the most relevant feature of QCD, and has deep consequences. *Asymptotic freedom* is the name given to the peculiar behavior of the QCD coupling constant, which is found to be large at low momentum transfer and decrease with increasing energy. In the coordinate space, α_s is small at short distances and surprisingly increases with increasing distance, therefore behaving oppositely to the QED coupling constant α. This behavior, as shown in Figure 2.1 has been confirmed in multiple experimental conditions. The first evidence for this behavior was found in deep-inelastic scattering reactions in 1969 [22], while the theoretical explanation came in 1973 in terms of renormalization and running coupling constant [23, 24][1]. In the case of QED

---

[1] For an historial review, see [25]

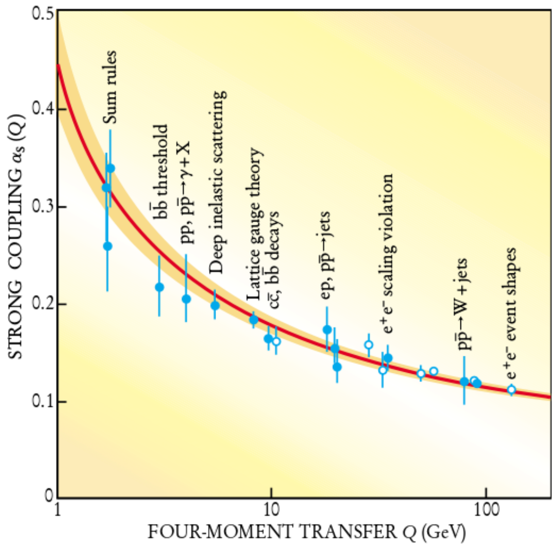

Figure 2.1: α_s as function of the transferred momentum Q, from [21]. The measurements from different experiments are superimposed to the theoretical prediction

the quantum fluctuation of vacuum are reabsorbed in the coupling constant, which becomes function of the transferred momentum. In the case of QCD the same effect occurs, but the vacuum polarization is composed by different contributions, due to either quark or gluonic loops. While the first ones have a screening effect, decreasing the effective strength of the interaction, the second one act in the opposite direction, increasing it. Two typical diagrams with screening and anti-screening contribution are shown in Figure 2.2 The net result is that the strong coupling constant

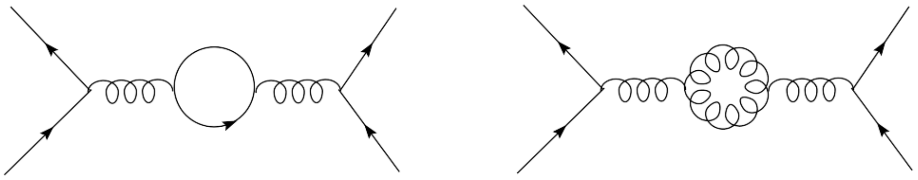

Figure 2.2: *Left:* 1-loop diagram with quark loop. *Right:* example of purely gluonic loop.

decreases with increasing transferred momentum, therefore the QCD is treatable perturbatively at high energies only:

$$\alpha_s(r) = \frac{2\pi}{9ln\frac{1}{r\Lambda_{QCD}}}$$

$\Lambda_{QCD} \approx 250$ MeV is the *QCD scale parameter* and r is a distance.

The second peculiar feature of QCD is the *confinement* [26, 27]: all the observable hadrons are color singlets, i.e. colorless, and no free colored object can exist at distance scales larger than $1/\Lambda_{QCD}$ [2]. This property, which is introduced by the lack of experimental observations of free quarks, is deeply connected with the asintotic freedom : to understand, at least quaitatively, this process let us assume to have two quarks in color singlet configuration, and let's try to obtain one free quark by pulling them apart, as shown in Figure 2.3. While they separate, the QCD coupling increases and with it the energy associated to the gluonic field, which is confined to

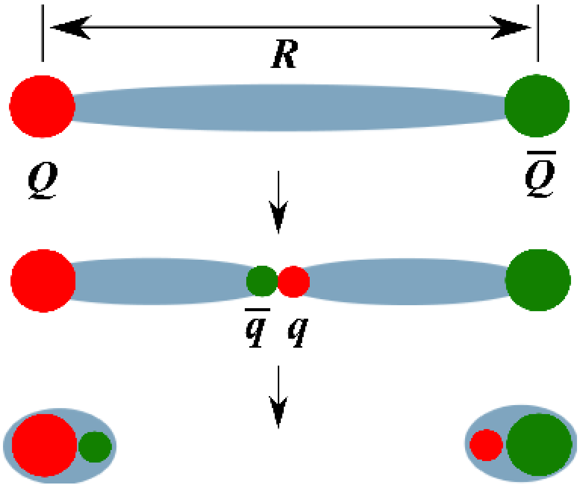

Figure 2.3: Graphical representation of two quarks being pulled apart. As the distance increases the color flux tube connecting them gets stretched until a new $q\bar{q}$ pair is created

---

[2] The assistance of free quarks and gluon at larger distances, known as *deconfinment*, is possible only for extremely dense or hot systems, like heavy ions collisions.

a tube-like configuration, the *color flux tube* [29, 30]. At a certain distance, the energy associated to the field is large enough to allow the creation of a new pair of quarks from the vacuum with consequent decreasing of the field energy. the process can be iterated an arbitrary number of times: every time we try to separate two quarks, a new pair appears from the vacuum and saturate the total color, so that no colorless objects can be create [3].

2.2 The Heavy quarkonium: foundations

The quarkonium, a bound state of two heavy quarks, is a quite unique environment to study the structure of the quark-quark interaction. This particular sector of particle physics was suddenly born with the discovery, in 1974, of two new mesons with quantum numbers $J^{PC} = 1^{--}$ and mass of approximatively 3.1 GeV/c^2[31] and 3.7 GeV/c^2[32, 33]. Shortly after a second family of mesons, with mass greater than 9 GeV/c^2 was observed [34]. The new states were rather quickly identified as bound states of a charm quark c and its anti-quark $\bar{c}$ [35] (*charmonium*) and of a bottom quark b and its anti-quark $\bar{b}$ (*bottomonium*), providing for the first time a strong confirmation of the quark model. In the years following the discovery of the J/ψ and the Υ, a rich population of new states was discovered and a peculiar pattern appeared. All the states seemed to fit a mass spectrum arrangement similar to the positronium, and strong selection rules were observed in the transitions among different states, suggesting that the orbital angular momentum is a good quantum number, as shown in Figure 2.4 and 2.5. In this framework each state is labeled with its momentum eigenvalue J, its radial excitation number n and the number of possible $q\bar{q}$ spin configurations $2S+1$, where $S = s_q + s_{\bar{q}}$. Since the quarks

---

[3] This picture is widely used in the simulation of the hadronization processes, i.e. the process that lead from quarks to observable hadrons

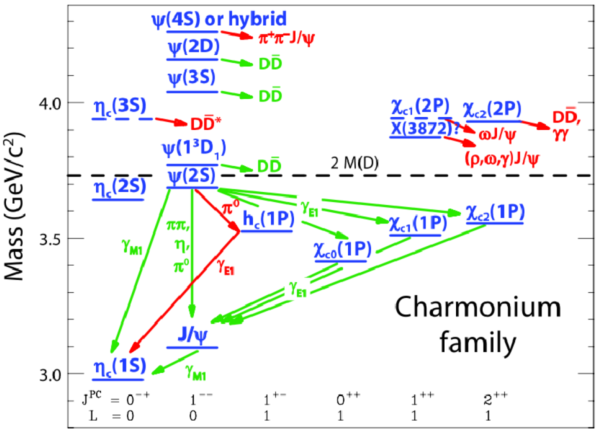

Figure 2.4: Charmonium spectrum, from [36].

have spin $s = 1/2$, like in the positronium case both spin singlets ($S = 0$) and spin triplets ($S = 1$) are possible.[4].

The patterns in the energy levels of these new state suggests that the dynamic of their constituent quarks is fundamentally non-relativistic. Indeed the average velocity of the heavy quark inside a meson can be roughly estimated by the mass difference between the ground state and the first radial excitation [40]; assuming that the mass of the ground state $M(1S)$ is proportional to $2m_Q$, and that in the first radial excitation a correction due to additional kinetic energy is present, such that $M(2S) = m_{Q\bar{Q}} = 2m_Q + m_Q v_Q^2$, the mass difference between the ground state and the first excitation $\Delta M$is proportional to $m_Q v_Q^2$, therefore

$$< v_Q^2 > \approx \frac{\Delta M}{M(1S)}.$$

---

[4] In describing these states a notation similar to the one used for positronium is adopted: we usually refer to the mass difference between a spin-triplet and a spin-singlet state in the same radial excitation as *hyperfine splitting*, and we name *fine splitting* the mass difference between the different states with same total angular momentum. In this case the naming scheme is misleading. While in the hydrogen atom the fine splitting is much larger of the hyperfine one, in bottomonium they are of the same size and, in some cases, the hyperfine splitting is even larger than the fine splitting in the same radial excitation. The spin singlet states are sometimes called *paraquarkonia*, and the spin triplet ones as *ortoquarkonia*

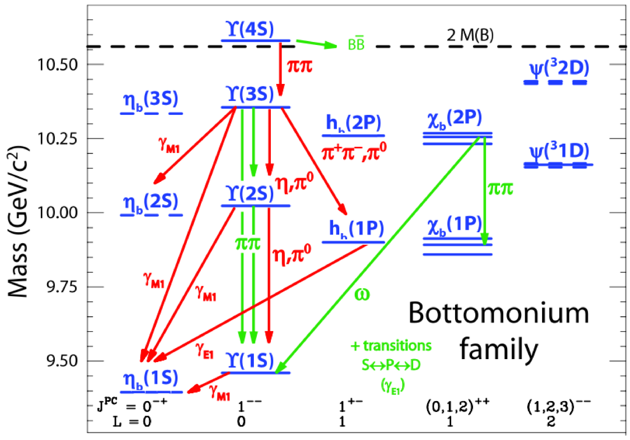

Figure 2.5: Bottomonium spectrum, from [36].

In both charmonium and bottomonium $\Delta M \approx 0.6$ GeV$/c^2$, therefore $< v_c^2 >\approx 0.2$ and $< v_b^2 >\approx 0.05$. Therefore, while in the low mass meson spectrum the quark mass is much smaller than the binding energy and the relative quark motion is intrinsically relativistic, in the case of heavy quark the system is non relativistic and the value of the orbital angular momentum can be assumed as a good quantum number,an a first description of the state spectrum can be obtained in the non-relativistic limit by solving a Schrödinger equation with a suitable potential. Relativistic effects, responsible for fine and hyperfine splittings, can be introduced afterwards as v^2 order correction.

2.2.1 The QCD static potential

Despite the similarities between bottomonium and positronium, a major difference arises from the nature of the binding potential. While the positronium is essentially an electromagnetic state, describable in terms of classical potential or, looking for a more suitable framework, using the QED perturbative approach, in this energy regime the QCD coupling constant α_s is much larger than the QED coupling constant α, thus the electromagnetic interaction can be safely neglected, and the properties of the bottomonium are completely determined by the QCD structure. At short distances QCD is perturbative, and we can assume that the single gluon exchange is the dominant processes. If this is true, the QCD in this regime resembles the electromagnetic interaction, and we can model it with a Coulombic-like potential function of the quark distance r, $V_{short} = \gamma\frac{\alpha_s}{r}$. The asintotic freedom and the confinement however require the potential to keep increasing with increasing r, so an additional term in the potential is needed. Historically the confining term is chosen to be a linear function of r, $V_{long} = \sigma r$. The potential obtained with this assumption, whose shape is shown in Figure 2.7, is known as *Cornell potential*[37]:

$$V(r) = -\frac{4\alpha_s}{3r} + \sigma r,$$

Intuitively the presence of a linear-like term at long distances and of a Coulombic-like one at short distances can be inferred by the comparison between the quarkonium spectra, the linear oscillator one and the positronium one, as shown in Figure 2.6. The quarkonium spectrum indeed exhibits both the typical feature originated by a purely linear potential, like the absence of degeneration between the D and P wave states, while the Coulombic term prevents the S and D states with same radial excitation number to have same mass.

Another possible choice is the logarithmic potential[38], which interpolates the long and short range behaviors:

$$V(r) = -C\log r.$$

This latter choice was motivated by the observation of very similar energy level spacings between charmonium and bottomonium, with $\frac{m_{\Upsilon(2S)} - m_{\Upsilon(1S)}}{m_{\psi'} - m_{J/\psi}} =$

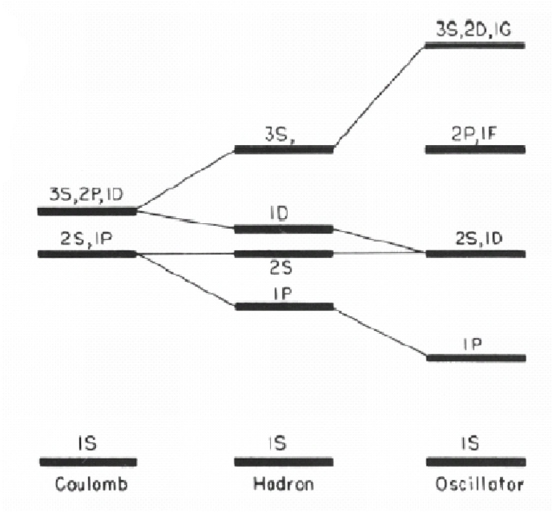

Figure 2.6: The charmonium energy levels compared with the predictions obtained with a Coulombic-like or harmonic potential.

0.955 and $\frac{m^{cog}_{\chi_b(1P)} - m_{\Upsilon(1S)}}{m^{cog}_{\chi_c(1P)} - m_{J/\psi}} = 1.010$. While the Cornell potential reproduces these similarities only for charmonium and bottomonium, the logarithmic one predicts the same spacing for any family[5].

2.2.2 Relativistic corrections: the hyperfine splitting

The non-relativistic approach clearly describes only the most general features of the bottomonium spectrum. The presence of a finite hyperfine splitting among the $1S$ states clearly shows that a spin-spin interaction, arising from relativistic effects, must be included for a more accurate description. However, these relativistic corrections can be included as perturbations of the static potential and treated in the Breit-Fermi approximation. At the v^2/c^2 order in the relativistic expansion the potential gets the

---

[5] This difference was particularly important when the bottomonium was discovered, since a third family of quarkonia, made of a $t\bar{t}$ pair, was still expected to appear. For an historical overview of the potential models in the early quarkonium era, see [39]

additional terms

$$V_1(\vec{r}) = V_{LS}(\vec{r})(\vec{L}\cdot\vec{S}) + V_T(\vec{r})(S(S+1) - \frac{3(\vec{(S)}\cdot\vec{r})(\vec{(S)}\cdot\vec{r})}{r^2}) + V_{SS}(\vec{r})(S(S+1) - 3/2),$$

where V_T is a tensor term, V_{LS} is the spin-orbit term and V_{SS} is the spin-spin interaction term [40]. The former ones are responsible for the fine splitting, while the latter one alone controls the hyperfine splitting. In order to get an analytical expression for these three potentials, one can try to model the whole QCD interaction in term of exchange of mediator particles with definite spin. The short range part, obviously, corresponds to the exchange of a vector massless particle and the corresponded potential is V_V. The long term interaction has been modeled in many different ways, usually as exchange of single scalar particles corresponding to the scalar potential V_S [36] [6]. This approach is purely phenomenological: the scalar, long range potential V_S is a single particle exchange model that mimics the effects introduced by the gluon-gluon interactions that originate the confining mechanism. With this formalism, the relativistic corrections can be written as functions of the static long-range and short-range potentials:

$$V_{LS}(\vec{r}) = \frac{1}{2m_b^2 r}(3\frac{dV_V}{dr} - \frac{dV_S}{dr}),$$

$$V_T(\vec{r}) = \frac{1}{6m_b^2}(\frac{d^2V_V}{dr^2} - \frac{1}{r}\frac{dV_S}{dr}),$$

$$V_{SS}(\vec{r}) = \frac{1}{3m_b^2}\nabla^2 V_V.$$

Assuming $V_V = -4/3\frac{\alpha_s}{r}$, the spin-spin interaction term becomes

$$V_{SS}(\vec{r}) = \frac{16\pi\alpha_s}{9m_b^2}\delta^3\vec{r},$$

---

[6] Alternatives based on the exchange of vector state [41] or mixtures of vector and scalar states [42] have also been proposed.

and a very simple yet powerful prediction on the hyperfine splittings can be obtained: the hyperfine splitting is therefore proportional to the value of the $b\bar{b}$ wave-function evaluated in the origin. $\Delta_{HF} \propto |\psi(0)|^2$ [43]. This means that Δ_{HF} is different from zero only for the states with even radial excitation number, and that its measurement is sensitive to both the Lorentz structure of the QCD static potential.

2.2.3 General properties of bottomonium

Assuming that the single gluon exchange to be the dominant interaction among the quark pairs, many general properties of bottomonium can be inferred by quite simple considerations.

In the quantum mechanical treatment of hydrogenoid atom, the average distance between the proton and the electron in the fundamental state is the Bohr radius, function of the interaction coupling and the electron mass, $R_B = \frac{1}{m_e \alpha}$. Since the short term QCD interaction is modeled after QED, we can estimate the bottomonium radius as

$$R_{b\bar{b}} \approx \frac{1}{\alpha_s m_b} \approx 0.1\text{fm}.$$

More complex calculations including also the long term interaction confirm this picture [44, 45]: the bottomonium is a compact state, as shown in Figure 2.7, and therefore the dominant component of the potential interaction, at least for the ground states, is the short-range one. However with increasing mass the radius also increases and the contribution due to the confining term becomes more and more important. This feature, as we will show briefly, has a major limiting role in our understanding of the hadronic transitions among quarkonia but also makes the bottomonium a unique system for studying the transitions from the short-range to the long-range potential or, in other words, the confinement effects.

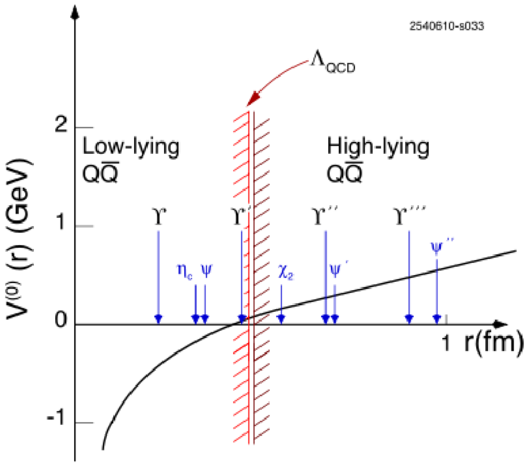

Figure 2.7: A Cornell-like potential tuned for bottomonium states. The potential parameters are extracted from the $\Upsilon(1S)$ and $\Upsilon(2S)$ experimental data. The radii of different bottomonium states are reported

Bottomonium states are usually divided in two families, according to their mass. The states with mass lower than twice the B meson mass are named *narrow quarkonia*, and are characterized by natural widths ranging from few tens of keV to few MeV. The states with mass above the $2m_B$ threshold are much broader, with widths of the order of tens of MeV. This striking difference is explained by the Okubu-Zweig-Iizuka (OZI) rule [46, 47]: the amplitude A for a strong annihilation is proportional to the number n of gluons emitted in the process, so that $A \propto \alpha_s^n$. The more massive is the initial state the more energetic are the gluons, and the lower is α_s. In the case of narrow bottomonia the only possible decay mode is thorugh the annihilation of the $b\bar{b}$ quark pair in either 2 or 3 gluons according to the quantum numbers, since the single-gluon annihilation is forbidden since the $b\bar{b}$ pair is a color single state, while the gluons belong to the color octet. The two amplitudes are, respectively, $A_{gg} \propto \alpha_s^2$ and $A_{ggg} \propto \alpha_s^3$, therefore we can immediately conclude that the vector states such $\Upsilon(nS)$ and $h_b(nP)$, which are forced to decay in three gluons, must be significantly narrower than the pseudo-scalars, like $\chi_{b0}(nP)$ and $\eta_b(nS)$, that can decay in two gluons since $\frac{A_{ggg}}{A_{gg}} \approx \alpha_s$, in an energy regime in which $\alpha_s << 1$.

When we then consider states with mass larger than $2m_b$, the annihilation of the $b\bar{b}$ pair is not the only decay mode, since the bottomonium can dissociate with the emission of a soft gluon that creates a pair of light quarks that, together with the original b quarks, originates a $B\bar{B}$ pair. In this case not only on single gluon is emitted, but its energy is significantly lower than the energy of the gluon emitted in an annihilation process. The ratio of the annihilation amplitude to the amplitude for the decay in $B\bar{B}$ pair can be written as

$$\frac{A_{ggg}}{A_{BB}} \approx \frac{\alpha_s^3(O(GeV))}{\alpha_s(O(MeV))}.$$

Since $\alpha_s(O(GeV)) << 1$ and $\alpha_s(O(MeV)) \approx 1$, we immediately see that the annihilation mode is suppressed, and therefore the natural width of these states is much larger than the one of the states below the *open flavor* threshold.

Besides the annihilations into gluons, the excited quarkonia can undergo a decay, either electromagnetic or strong, in which a lower mass quarkonium state is produced in association to a photon or a light meson system. The QCD an QED Lagrangian are completely invariant under charge and parity transformations, therefore the corresponded quantum numbers are strictly preserved by any strong or electromagnetic interaction. This property allows to set a number of selection rules that determine which kind of transitions, both radiative and hadronic ones, are allowed and which are forbidden [36]:

- Radiative transitions $(b\bar{b})' \to \gamma(b\bar{b})$ are possible only between states that differs by a unit of angular momentum ($|\Delta l| = 1$), so the possible transitions are $P \leftrightarrow S$ and $D \leftrightarrow P$ and $^3S \leftrightarrow ^1 S$. The same kind of transition can obviously happen with the emission of a vector meson like the ω [48, 49].

- Hadronic transitions with a single scalar meson (π^0, η, η') can connect, if we consider only the angular momentum conservation, each pair of states. On the other hand the conservation of C- and P-parity forbids processes like $1^{--} \leftrightarrow (0, 1, 2)^{-+}$, namely $\Upsilon(nS) \rightarrow \pi^0, \eta\chi_{bJ}(mP)$, while transitions like $\Upsilon(nS) \rightarrow (\pi^0, \eta)(\Upsilon(mS), h_b(mP))$ are still possible. Since all these transition are mediated by the strong interaction, we must take into account also the (partial) conservation of the Isospin that greatly suppress the π^0 transition with respect to the η, η' ones.

- Hadronic transitions with two scalar mesons ($\pi^+\pi^-$, $\pi^0\pi^0$) are the dominant transitions between $\Upsilon(nS)$ states below the open beauty threshold. The conservation of the isospin requires $\mathcal{B}(Y(nS) \rightarrow \pi^+\pi^-\Upsilon(mS)) \approx 2 \times \mathcal{B}(Y(nS) \rightarrow \pi^0\pi^0\Upsilon(mS))$.

2.3 Heavy quarkonium: recent progresses

In the last section we presented the basic properties of bottomonium, and we showed how they can be described by a static potential with additional relativistic corrections. However the description of the fine structures of quarkonia, and especially of their transitions, required the development of more complex tools and theoretical models. For an exhaustive review on this subject, see [15, 16, 17].

2.3.1 Quarkonium as a multi-scale system

The description of quarkonium is a rather challenging task for QCD. At high energies analytical solutions of the QCD Lagrangian can be found with a perturbative expansion in α_s, leading to quite precise results. Some aspects of quarkonium, like formation and annihilation, can be described with this approach as well, as they ar characterized by energies of the order of $m_b \approx 4.8$ GeV, but this is note the case of the hadronic transitions, were the involved energies are $O(0.1)$ GeV and the expansion the Lagrangian in powers of α_s is either converging very slowly or not converging at all.

For this reason a massive theoretical effort has been devoted to create alternative theories. One of the most fruitful idea is to replace the QCD Lagrangian with an effective Lagrangian that is treatable with a power expansion in some observable other than α_s, obtaining a faster convergence of the perturbative series. These family of theories are collectively knows as *effective field theories* (EFT) [15, 50, 51, 52]. The starting point for the construction of the most used EFTs is the presence of a natural hierarchy of scales in quarkonium, as a consequence of the non-relativistic nature of this system. The quark velocity v is a sufficiently small parameter that naturally leads to a hierarchical arrangement of different dynamical scales. The gluons emitted in the annihilation of a bottomonium state have energy of the order of the quark mass m_b. This scale, which is treatable perturbatively, is the *hard scale*. The quark-anti-quark interaction is characterized by the exchange of gluons at an energy scale of mv, usually called *Mid scale*, while the corrections due to the gluon-gluon interaction belong to the *soft scale* mv^2. An example of the interplay between the different scales is given in Figure 2.8. The QCD Lagrangian of a non-relativistic system can be rearranged ordering the different contributions from the different scales. Since a given physical process is usually dominated by a certain scale, the effective field theories can be constructed integrating

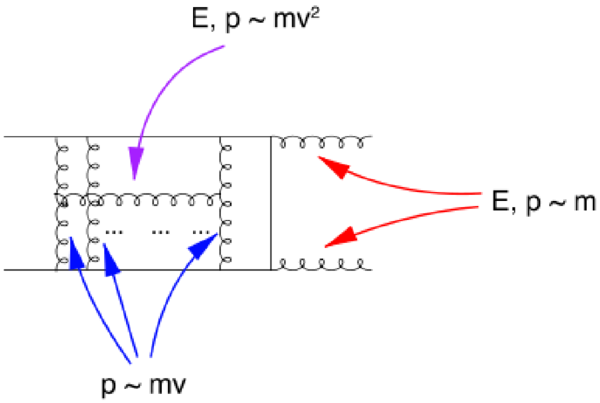

Figure 2.8: A Feynman diagram showing interaction at different energy scales

out all the contributions due to scales harder or equal to the one of interest, factorizing the non-perturbative effects in a set of operators that can be evaluated numerically. Following this approach, the first scale to be integrated is the hard one, and the correspondent effective theory is the Non-Relativistic QCD (NRQCD)[53, 54, 55]. This approach is suitable for the study of all the processes that take place at this scale m, such the annihilation or the production of bottomonium. The underlying idea is to factorize all the effects at the scale m by introducing a cutoff μ, and encode the softer scale effects in local operators $O_n(\mu, mv, mv^2, ...)$. Therefore the NRQCD Lagrangian basically reads as a power expansion in m:

$$\mathcal{L}_{NRQCD} = \sum_n \frac{c_n(\alpha(m), \mu)}{m^n} \times O_n(\mu, mv, mv^2, ...),$$

where the contributions due to the m scale are comprised in the Wilson coefficients c_n. The local operators O_n model the non-relativistic, non-perturbative effects and depends on the scale mv

A further step is to integrate the $mv \approx r^{-1}$ scale, obtaining a theory suitable for the study of the fine structures of the spectra known as potential-NRQCD (pNRQCD) [56]. Its Lagrangian somehow recalls the structure of the NRQCD one, since the basic approach is similar:

$$\mathcal{L}_{pNRQCD} = \int dr \sum_n \sum_k \frac{c_n(\alpha(m),\mu) \times V_k(\mu,\mu',r)}{m^n r^{-k}} O_k(\mu', mv^2, ...),$$

where μ' is an additional cutoff, $V_k(\mu,\mu',r)$ are Wilson coefficients encoding the effects at the scale mv and $O_k(\mu', mv^2, ...)$ are the pNRQCD operators, evaluable on the lattice.

The *lattice QCD* is a numerical approach to the strong interaction problem based on the path integral formalism. Originally delevoped for the study of the low mass states (glueballs in particular [57]) [58, 59, 60], it has been re-adapted to the description of the heavy quarks too [61, 62]. The basic assumption of this approach is that the transition amplitude between two states can be expressed as the sum of single amplitudes calculated on every possible path in the phase space that connects the initial and the final states, each one weighted by the value of its classical action. This theory can be used, under the additional assumption that the most probable path is the classical one and that the whole amplitude can be expressed as a perturbative series in the phase space around the classical path, to perform analytical calculation, obtaining the same results that can be obtained by the perturbative approach. The general aspect of a path integral can be shown also in the simplest case: a single particle propagator in one dimension, from the position x_0 at the time t_0 to the point x_1 at time t_1 can be expressed by:

$$< x_1, t_1 | x_0, t_0 >= \lim_{n\to\infty} k^{n/2} \int \; Dx \; exp[\int \mathcal{L}_{QCD} dt]$$

Where $\int Dx$ represents the sum over all the possible path joining (x_0, t_0) and (x_1, t_1), $k = \frac{m}{2\pi i \hbar \Delta t}$ is the normalization constant and $\int \mathcal{L}_{QCD} dt$ is the classical action associated to each path. Even if the integration is usually performed by introducing a series expansion that makes possible the factorization of the interaction terms leaving a sum of free particle propagators, this is in principle an exact theory. Therefore it is possible to perform numerical calculations and obtain matrix elements also for soft or ultra-soft scale processes in QCD, that are inaccessible with a perturbative approach.

From the numerical point of view, the key of this technique is the evaluation of the quantum operators on a discretized phase space; the transition amplitude is calculated by the path integration along concatenated loops. The computational resource required to perform those calculations are the major limiting factor to the use of this technique. A complete lattice calculation of a $b\bar{b}$ bound state is required to satisfy very stringent limits imposed by the presence of many different energy scales, with non-trivial interplay between each other: the lattice spacing must be at least of the size of the De Broglie length of the b quark, i.e. $a < m_b^{-1} \approx 0.04$ fm, and the overall grid of size but be larger than the bottomonium size, therefore $L \approx 1$ fm[7]. The calculations on such a large grid is still a challenging task for the the available computational power, and can be considered practically still unfeasible[8]. However the NRQCD and pNRQCD operators do not depend on all the energy scales, and can therefore be evaluated on much smaller lattices, finally matching the current computational power [63].

---

[7] In terms of energy energy scales, the problem arises from the large difference between the mass of the b quark and the typical energy of the exchanged gluons. Similar problems are not present in the low mass meson sector, where the mass of the state is on the same scale of the binding energy.

[8] These requirements should be interpreted as minimal. In order to reduce the systematic uncertainty on the prediction, lattice spacing as low as 0.005 fm are actually required.

2.3.2 A new hadron spectroscopy

Aa new rich phenomenology consisting in new exotic states, unexpected transitions or sizable corrections to the energy levels above the threshold has been discovered in the last years, challenging the available theoretical models and triggering wide discussion in both the theoretical and experimental communities [15, 16, 17]. The common denominator of all the new, unexpected effects is the presence of light degrees of freedom not accounted by the simple $b\bar{b}$ model. Their presence is not an absolute surprise. The fact that thresholds located nearby a resonant state can shift its mass [64, 65] or modify its decay is known since long time as *coupled channel effect*. For example near the threshold for the open flavor, the diagrams describing the quarkonium states or their transitions can get contributions from virtual meson loops similar to the one shown in Figure 2.9. To understand the size and the relevance of these effects, it is useful to compare the spectrum of the known states with the theoretical predictions obtained within the same potential model, turning either on and off the couple channel effects[66] (Figure 2.10).

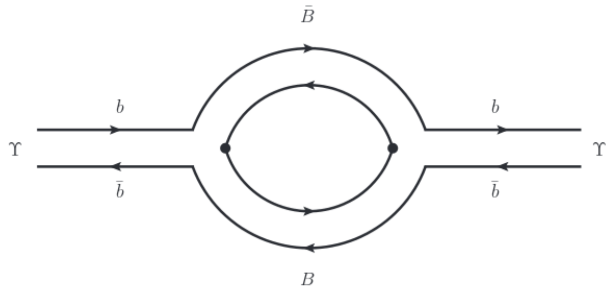

Figure 2.9: An example of a bubble diagram with virtual B mesons, contributing to the description of the $\Upsilon(nS)$ states near the threshold, from [66].

The presence in the quarkonium of light degrees of freedom, more and more important approaching the open flavor threshold, is therefore

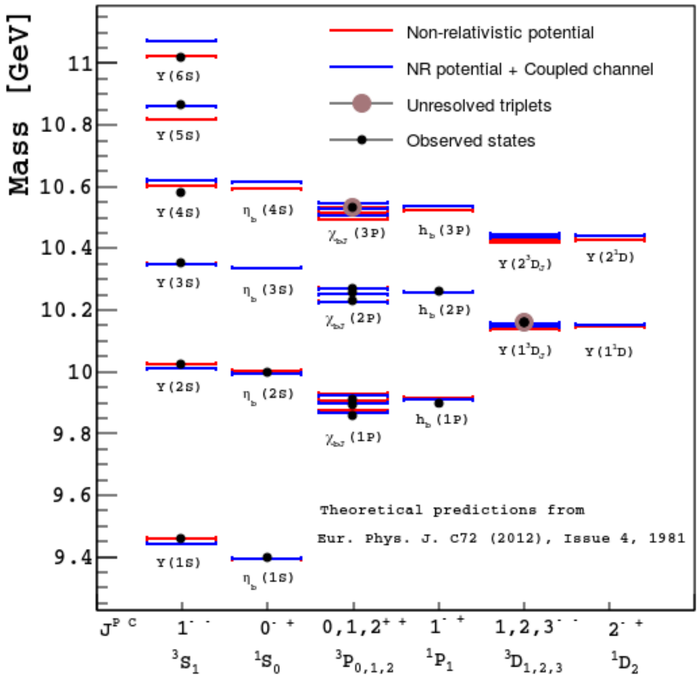

Figure 2.10: Prediction on the bottomonium energy levels with and without accounting for the coupling channel effects, from [66]. The experimental results are superimposed to the theoretical predictions.

not a new or unexpected phenomenon in the quarkonium sector, and the couple channel effects were already included in early descriptions of the dipion transitions from the $\Upsilon(3S)$ [67, 68]. What was surprising in the last years is the manifestation of light quark effects in a number of different ways, perhaps the most spectacular one being the rising of large number of unpredicted states with exotic quantum numbers in both the bottomonium and charmonium sector.

The quark model, already in its very first formulation, was expected to produce states other than the ordinary mesons and baryon. Indeed in principle other quark combination (collectively known as *QCD exotics* or simply *exotica*) can realize color singlets such $qq\bar{q}\bar{q}$, $qqqqq$, $qqq\bar{q}\bar{q}\bar{q}$ [18], respectively known as *tetra-quarks*, *penta-quarks* and *di-baryons*. Also more complex combinations of gluons and quarks (*hybrids*), or gluons only (*glue-*

balls) are allowed by QCD and should appear in the hadronic spectrum as states that do not fit the standard meson and baryon patterns.

The quest for these states was extensively carried on in the light hadron sector for several decades, always resulting in non-conclusive results[69]. The main reason for this unsuccessful search is probably in the structure itself of the low mass hadrons. In this region, as we pointed out, the mass of the constituent quark is much smaller than the binding energy therefore the systems are completely relativistic and the mixing among different states is allowed. In addition to that, both the baryon an meson spectrum are quite densely populated by numerous radial excitations of the same ground states, whose separation is usually comparable with their natural width. In other words, in this region the identification of the resonant states themselves can be rather complex and not trivial, and the QCD exotic could actually be overshadowed by either mixing effects or by the presence of quark-model candidates nearby.

On the other hand, the quarkonium spectrum is much more simple: the presence of unexpected states below the threshold or particularly narrow states above it, the observation of states with quantum numbers that do not fit the $q\bar{q}$-based predictions or, finally, the observation of charged states with heavy flavor content are all striking evidences of some new phenomenology or new family of states. The first manifestly exotic state was observed by Belle in the $B \to K\pi^+\pi^- J/\psi$ decay as a narrow resonance in the $J/\psi\pi^+\pi^-$ final state with mass of 3.872 GeV/c^2 [70]. The $X(3872)$ was shortly after observed in be produced promptly in high energy $p\bar{p}$ collisions at Tevatron [71, 72], and then confirmed in different final states at the B-factories [73, 74, 75, 76].

After the $X(3872)$ many other exotic states were observed, both in B meson decays or in hadronic transitions among charmonia: the $Z(4430)^\pm$ was the first charged-charmonium like state to be observed, again by Belle, decaying into $\psi'\pi^{\pm}$ [77, 78, 79]. Its strong decay into a charmonium state requires the initial state to already contain a $c\bar{c}$ pair, but on the other hand its electric charge can be justified only by the presence of at least other two quarks, likely to be light. The interpretation of the $Z(4430)^{\pm}$ as an exotic state took quite long to be accepted. The BaBar collaboration [80] studied the same decay with a data sample smaller than the Belle's one, observing the same deviation from the phase-space flat distribution but ascribing it to interference effects due to excited $K^{\star}$ resonances in the $K\pi$ channel not accounted by Belle.

While the debate on the existence of the $Z(4430)$ was going on, Belle observed an enhanced rate in the dipion transitions $\Upsilon(5S) \to \Upsilon(1S, 2S, 3S)$ and the totally unexpected transitions $\Upsilon(5S) \to \pi^{+}\pi^{-}h_{b}(1P, 2P)$ [81]. The latter ones especially were expected not be sizable , since they require a spin flip of the heavy quark, but were observed to be of the same size of the non-spin flipping processes $\Upsilon(5S) \to \pi^{+}\pi^{-}\Upsilon(1S, 2S, 3S)$. We will come back again on the role of the heavy quark spin symmetry (HQSS) in the description of the hadronic transition and on the anomalous dipion transitions from the $\Upsilon(5S)$ in the section devoted to the discussion of the phenomenology of the hadronic transitions. For the moment, we wish simply to remark that the presence of these unexpected transitions triggered an investigation on the possible HQSS breaking mechanism occurring at the $\Upsilon(5S)$. The analysis of the single pion recoil spectrum in $\Upsilon(5S) \to \pi^{+}\pi^{-}h_{b}(1P, 2P)$ and $\Upsilon(5S) \to \pi^{+}\pi^{-}\Upsilon(1S, 2S, 3S)$ events showed the presence of two narrow peaks, the $Z_{b}(10610)$ and $Z_{b}(10650)$, with masses of 10607.2 ± 2.0 and 10652.2 ± 1.5 GeV/c^{2} [82]. The mass and the width of these states measured in processes with quite different phase-space volume as $\Upsilon(5S) \to \pi^{+}\pi^{-}\Upsilon(1S)$ and $\Upsilon(5S) \to \pi^{+}\pi^{-}\Upsilon(3S)$, were found to be completely in agreement, strongly suggesting that the Z_{b} are not artifacts due to interference effects or final state interactions. For the first time a plainly exotic, charged structure was observed and widely accepted by both the theoretical and the experimental community.

Finally, also the $Z(4430)^{\pm}$ has started being considered as a true exotic resonance when the LHCb collaboration applied to its data samples both the fit proposed by Belle and the one proposed by BaBar, confirming the resonance interpretation given originally by Belle [83]. Despite its controversial history, the $Z(4430)^{\pm}$ is now regarded as the first discovered tetraquark candidate in the quarkonium sector.

Experimentally the study of the exotic charmonium states is much easier than the bottomonium ones. The former one can both be produced in $e^{+}e^{-}$ collisions, B meson decays or complete $p\bar{p}$ annihilations[9], while for the latter one only the first option is available [10]. It is therefore quite natural that the largest fraction of the exotic states have been observed in the charmonium sector. Alongside with the $Z(4430)$ other six exotic charged structures have been observed by different experiments: $X(4020)$ (BESIII [89]), $X(4050)$ and $X(4250)$ (Belle [90], not confirmed by BaBar [91]), $X(4240)$ (LHCb [83]) $Z_c(4200)$ (Belle [92]), all with mass above the open flavor threshold [11]. The most recent, strong evidence of a tetra-quark-like state in the charmonium family came from the observation of the $Z_c(3900)$ by BESIII and Belle as a $J/\psi\pi^{\pm}$ resonance in $Y(4260) \to \pi^{\pm}\pi^{\mp}J/\psi$ [93, 94] and as a $(D\bar{D}^{\star})^{\pm}$ enhancement in $Y(4260) \to \pi^{\mp}(D\bar{D}^{\star})^{\pm}$ [95]. Figure 2.11 shows the charmonium spectrum after the addition of the newly discovered states.

---

[9] The study of charmonium in complete $p\bar{p}$ annihilation was carried on at the CERN intersecting storage rings [84] and more recently at Femilab [85, 86] until 2000. The proposed Panda experiment [87] at the FAIR facility [88] should resume this kind of research in the future.

[10] We intentionally omit from this list the hadronic colliders. A part from the $X(3872)$, no other exotic state has ever been observed in prompt production from pp or $p\bar{p}$ collisions, and the studies of the charmonium-like states at the LHC or the Tevatron has been almost entirely performed reconstructing them in B meson decays.

[11] In this context the open flavor threshold is not a fixed value, but is different for each quantum number.

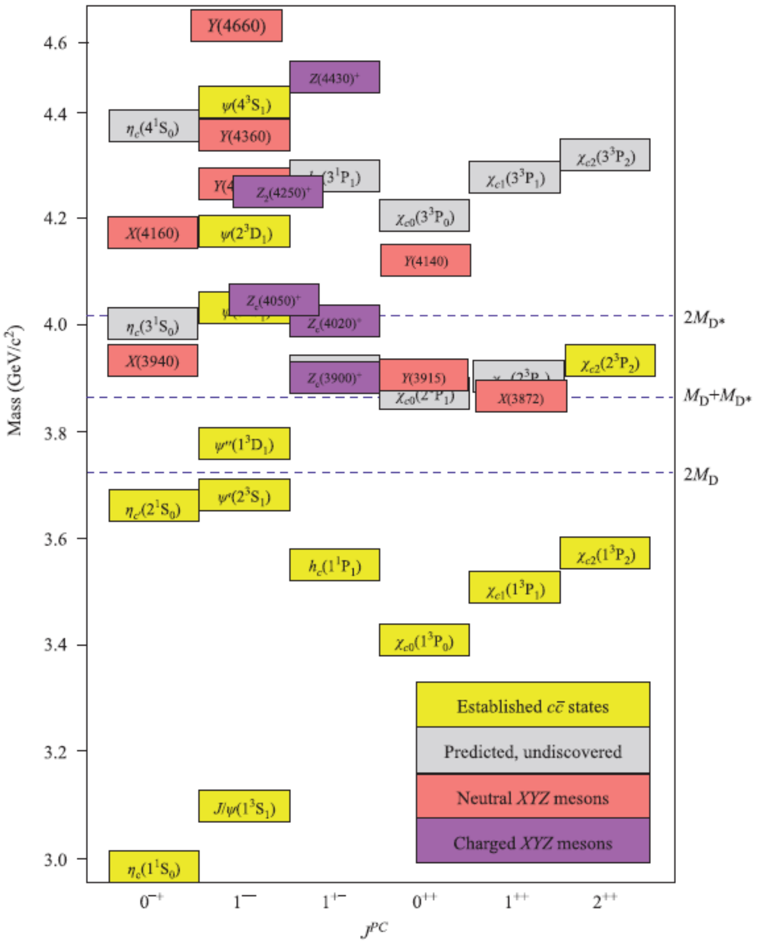

Figure 2.11: Spectrum of charmonium and charmonium-like states

2.3.3 Tetraquarks, molecules, and other models

The theoretical interpretation of these states, both in charmonium and bottomonium is still controversial [96]. Unfortunately all the exotica are located in the region above the threshold, where even the conventional state are broader and the theoretical prediction on their position is less precise, due to the larger and larger effect of the light degrees of freedom. For some state such the $X(3872)$ and the $Z(3915)$ interpretation as conventional charmonium [97] or the result of the mixing between a conventional state and and exotic state nearby [98] have been investigated [99, 100, 101].

Also in the case of charged quarkonia-like, for whom the conventional interpretation is impossible, many proposals have been made. Some authors remark the fact that many of these states are located close to a threshold for B or D meson pair production or that their decay mode prefers the open rather than the hidden flavor modes, and interpret them as loosely-bound, molecular like object, composed by two flavored mesons binded by a residual strong interaction [102, 103][12]. This could be the case of the Z_bs [105], which are both located at less than 2 MeV from the $B\bar{B}^\star$ and $B^\star\bar{B}^\star$ thresholds respectively, and have as dominant decay $Z_b(10610) \rightarrow B\bar{B}^*$ and $Z_b(10659) \rightarrow B^\star\bar{B}^\star$. The behavior of the despite the $Z_b(10659)$, that do not decay into $B\bar{B}^*$ despite the larger phase-space, supports its interpretation as a weakly bound $B^\star\bar{B}^\star$ molecule and suggest a similar picture for the $Z_b(10610)$.

Other authors are more keen to interpret the charged states as tetraquarks, bound states of four quarks that all interact through gluon exchange. In the tetraquark model the for quarks constituting the exotic state ar arranged in two $SU(3)_{color}$ octet states, the di-quarks, instead that in two $SU(3)_{color}$ single pairs as happens in the molecular model [106, 107, 108, 109]. The tetraquark model is certainly more appealing for its direct connection with the fundamental QCD properties, since the diquark-diquark is the actual QCD interaction and not a residual Vandeer-Waals like interaction among neutral objects as the one assumed in the molecular model. As confirmation of its validity, the tetraquark approach was recently successfully used to explain the peculiar features of the $SU(3)_{flavor}$ nonet of scalar mesons [110]. Some experimental observation strongly support the tetraquark model: the narrow width of the $X(3872)$ and its production rate at high transverse momentum in $p\bar{p}$ and

---

[12] The original proposal of weakly bound states formed by light mesons, such as (KK), was made by Tornquist in the early 1980s [104], and later extended to the heavy mesons sector. For a compared review of the molecular model and the other proposals, see [96] and the references therein.

pp collisions in the TeV regime are hardly justified by the molecular model. Furthermore after the discovery of the $Z(4430)$ another tetraquark state with mass $m_Z = m_{Z(4430)} - (m_{\psi'} - m_{J/\psi}) \approx 3900$ MeV/c^2 was predicted [111], easily identifiable as the newly discovered $Z_c(3900)$.

A final model we wish to report is the hadro-charmonium, which describes the exotica as conventional charmonium states surrounded by a "cloud" of light quarks [112]. Pictorially the difference between tetraquarks and molecule can be represented as in Figure 2.12.

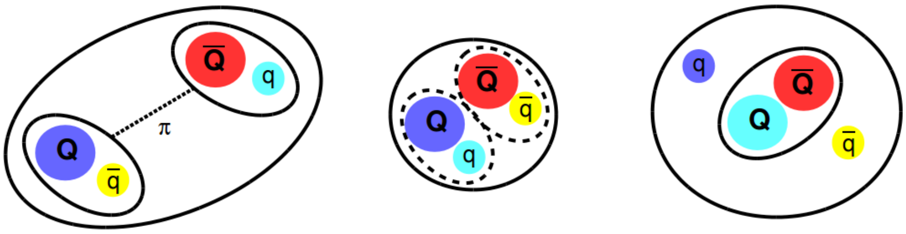

Figure 2.12: Cartoon depicting three different models for the exotic heavy hadrons. The solid circles represent the color singlets, while the dashed one represents the color octet configurations. On the left, a heavy meson molecule: two color singlets interact thorugh a residual color field. In the middle, a tetraquark: the four quarks are arranged in two diquarks. In the right the hadro-quarkonium model, in which a heavy meson is surrounded by light quarks, constituting a light meson.

Unfortunately so far none of these group was able to identify a striking experimental feature able to distinguish among different models, and the debate on the nature of the exotic is still very active.

On a more general level, whatever the exact nature of these exotic states is, it's certainly true that they are all the result of the presence of light degrees of freedom inside the $Q\bar{Q}$ states, which can definitively not be neglected in the revetment of the states above threshold. This is perhaps the most relevant aspect of these discoveries: while the quarkonium below threshold is a quite straightforward system and allows to make precision test of the basic properties of QCD in the non-perturbative regime, the region above the threshold is showing all its potential to study the ultra-soft dynamics of light quarks without many of the theoretical and experimental complications present in the low mass hadrons.

2.3.4 The hadronic transitions puzzle

QCD multipole expansion

The hadronic transitions among quarkonia are very hard to describe in the α_s pertubative expansion, since they consist in the emission of low-momentum hadrons that can be interpreted as the emission of soft gluons (at least two, in order to have a global color singlet state), with energy of few hundreds of MeV, that subsequently hadronize into one or few mesons, as depicted in Figure 2.13. This situation is however very similar to the one encountered in the description of the transitions among atomic levels in QED: in this case, a low energy photon is emitted by the de-excitation of an electron, and a quite successful theoretical description is given by the QED *multipole expansion*. The transition probability Γ between

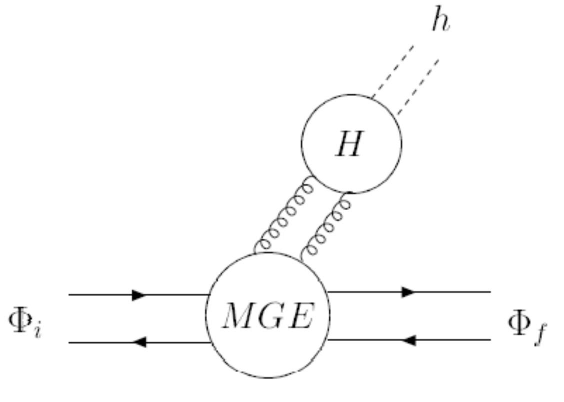

Figure 2.13: Sketch of an hadronic transition among two bottomonium states ϕ_i and ϕ_f. The gluon emission and the subsequent hadronization take place in two different vertexes assume dot be independent.

a state ψ_a an a state ψ_b in QED is proportional to

$$\Gamma \propto < \psi_b | \epsilon e^{i\vec{k}\vec{r}} | \psi_a >,$$

where ϵ is the polarization vector, $\vec{k}$ is the photon momentum and r is the source radius. If the condition $kr << 1$ is met a power expansion is possible and

$$\Gamma \propto < \psi_b | \epsilon | \psi_a > + i < \psi_b | \epsilon \vec{k} \vec{r} | \psi_a > + ...$$

The terms of the expansion are traditionally named *electric* (E) or *magnetic* (M), so that first term is the electric dipole or $E1$ one, the second one is the magnetic dipole or $M1$, the third term is the electric quadrupole or $E2$ term, and so on.

When dealing with hadronic transitions among quarkonia the situation is somehow similar. Soft gluons with momentum k are emitted by a small source of radius r, and for many transitions $kr << 1$. Therefore the QCD interaction Hamiltonian can be expanded in a series of multipoles, reminding the usual electromagnetic multipole series expansion:

$$H_I = \int d^3 x Q(x) t^n [x \cdot E_a(x) + \sigma \cdot B_a(x)] Q(x) + ...[\text{checkthis...doyouneedit?}]$$

where t^a are the SU(3) generators and the E and B fields are the chromoelectric and chromomagnetic fields.This theory is known as QCD multiple expansion (QCDME) [113, 114, 115, 116, 117, 118, 119, 120]. The presence of the SU(3) generators make a single H_I interaction able to change the color state of a $Q\bar{Q}$ state from singlet to octet: this means that every physical transition must include at least two single interactions: the first one turns the singlet state into octet, and the second one re-turns the octet state into an observable state. This behavior, which is not present in the electromagnetic interaction, can be interpreted as the emission of at least two gluons in hadronic transition, while electromagnetic transitions can proceed via a single photon emission. As it happens for the QED multipole expansion, this approach is suitable if the size of the *emitting source*, in this case the initial bottomonium state, is smaller than the De Broglie length of the emitted gluon. In this sense the fact that the bottomonium is, as anticipated, a very compact system is crucial for this model, but the increasing $b\bar{b}$ separation as the mass of the state increases fixes a limit to its applicability. Figure 2.14 shows the radii at which $kr = 1$, for different gluon momenta k.

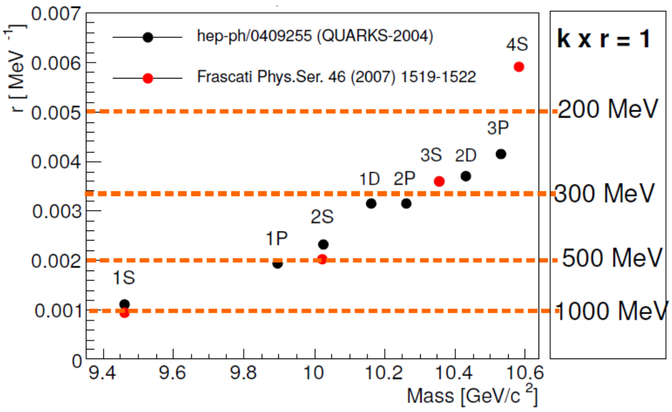

Figure 2.14: Threshold of applicability of the QCDME for different gluon momenta, compared to the bottomonium radii evaluated in the potential model.

QCDME models the gluon emission as a two step process: the emission of the first gluon turns the initial color singlet $b\bar{b}$ into a color octet state, which subsequently emits the second gluon and turn back into a color singlet. Finally the hadronization of the gluons into the final state hadrons is assumed to be completely independent from the gluon emission vertex. Clearly the description of the intermediate states plays a crucial role in this formalism, but also makes these prediction sensitive to the presence of exotic states nearby the transition region. In the early stages of QCDME the energy levels intermediate states were computed using potential models [119], while more recent works threth the intermediate state as a $b\bar{b}g$ system, where the two quarks are connected by a color string, and identify its energy levels with the vibrational level of the string [120, 121].

It can be useful here to explicit report a possible expression [120] for the $\pi\pi$ transitions among S^3 states, which is at the leading order a pure $E1E1$ processes [13]:

$$\mathcal{A}_{E1E1} = i\frac{g_E^2}{6}\sum_{K,L}\frac{< \Phi_I|\vec{x}_k|K,L >< K,L|\vec{x}_l|\Phi_f >}{E_I - E_{KL}} < \pi\pi|E_kE_l|0 >,$$

In which the gluon emission is factorized from the $\pi\pi$ creation, represented by the $< \pi\pi|E_kE_l|0 >$ term. The intermediate states $|K,L >$ are a complete set of color octet states that represent a transitional phase of the bottomonium state, which turns from color-singlet to color octet after the first gluon emission and turns back into color single after the second gluon emission. g_E is the effective coupling constants of the chromoelectric gluon and the quark. It must be notice that the evaluation of the $b\bar{b}$ separation $\vec{r}$ is usually carried out with a potential model, whose choice influences the results of QCDME.

The amplitude for the η transition among the same states gets contribution both from the $E1M1$ and the $M1M2$ processes, and it's dominated by the first one. The amplitude reads similarly to the one for the $\pi\pi$ transition, with a major difference represented by an overall multiplicative factor Λ_{QCD}/m_b, that greatly suppresses the η transition with respect to the $\pi\pi$ one. This factor is connected to the flip of the third component of the heavy quark spin, and accounts for the violation of the *heavy quark spin symmetry* (HQSS). Clearly the spin-flipping amplitude vanishes in the limit $m_Q \to \infty$, in which the HQSS is strictly preserved.

---

[13] Here the quark confining string model is assumed for the description of the intermediates states, that are assumed to be $b\bar{b}g$ hybrids

Experimental puzzles

This work is devoted to the study of the η transitions from the $\Upsilon(4S)$ and $\Upsilon(5S)$ to lower bottomonium states.

We already introduce dthe idea that the study of the hadronic transition is tightly entangled with the study of the exotic states: if the latter one are the direct manifestation of the presence of light quarks in the bottomonium not only as virtual pairs emerging from the vacuum, but as actual valence quarks, the former are sensitive to virtual quark loops, exotic intermediate states or rescattering effects that can enhance them. A paradigmatic example of this tight interaction is given by the history of the discovery of the Z_b. The first anomaly in the $\Upsilon(5S)$ was observed as an unpredicted high branching ratio for the transitions $\Upsilon(5S) \to \pi^+\pi^-\Upsilon(1S)$, which was observed by Belle during an early scan of the $\Upsilon(5S)$ region. As discussed in the previous sections, naïvely the transitions from above the threshold to narrow states were expected to be negligible. Also surprisingly, the maxima of the $e^+e^- \to \pi^+\pi^-\Upsilon(1S)$ and $e^+e^- \to hadrons$ cross sections were not coinciding [122], and for some time the hypothesis of the presence of two overlapping resonances instead of one single bottomonium state was proposed [123] [14]. Only as a consequence of these observations additional studies were performed on larger data samples, and the unexpected transitions $\Upsilon(5S) \to \pi^+\pi^- h_b(1P)$ were discovered. Finally, from the analysis of the $\pi^+\pi^- h_b(1P, 2P)$ and $\pi^+\pi^-\Upsilon(1S, 2S)$ dalitz plots, the Z_bs were discovered.

Another peculiar characteristic of the hadronic transitions from above the threshold is a large violation of the HQSS. The ratios between the η and $\pi\pi$ transitions among $\Upsilon(3S)$, $\Upsilon(2S)$ and $\Upsilon(1S)$, $\mathcal{R}^{3S,2S\to 1S}_{\eta,\pi\pi}$ is of the

---

[14] A Recent, more precise and fine-grained measurement by Belle of the R ratio and of $\sigma[e^+e^- \to \pi^+\pi^-\Upsilon(nS)]$ in this region seem to suggest that the shift is due to the interference between the continuum and the resonant cross section [124]. The problem of the modeling of the structures in this region and their understanding is, however, still open.

order of $\Lambda^2_{QCD}/m_b^2 \approx 4 \times 10^{-3}$ as predicted from the QCDME model: $\mathcal{R}^{2S\to 1S}_{\eta,\pi\pi} = (1.6 \pm 0.2) \times 10^{-3}$ [125, 126, 127] and $\mathcal{R}^{3S\to 1S}_{\eta,\pi\pi} < 2.1 \times 10^{-3}$ [126]. At the $\Upsilon(4S)$ energy the situation is completely reversed. The BaBar collaboration measured $\mathcal{R}^{4S\to 1S}_{\eta,\pi\pi} < 2.4 \pm 0.5$ [128], therefore the spin flipping process is even enhanced with respect to the non spin-flipping one. Soon after a similar behavior was also observed in the $\Upsilon(5S)$ decays, where the η transitions [129] are of the same order of magnitude of the $\pi\pi$ ones: $\mathcal{R}^{5S\to 1S}_{\eta,\pi\pi} = 0.13 \pm 0.10$ and $\mathcal{R}^{5S\to 2S}_{\eta,\pi\pi} = 0.49 \pm 0.37$. Despite the QCDME model is expected to be not reliable for wide states, such a spectacular violation of the HQSS triggered the interest of the theoretical community. Table 2.1, 2.2 and 2.3 show a tentative summary of the most recent predictions on the $\pi\pi$ and η transitions and on their ratios. The predictions reported by Kuang [120] and Segovia and collaborators [121, 130] are obtained using the QCDME with different models for the intermediate hybrid states. The results by Simonov and Veselov [131, 132, 133] are obtained using the field-correlator approach [134]. The prediction by Voloshin [40] is obtained scaling the results obtained in the charmonium to the bottomonium, assuming the QCDME. Meng and collaborators [135] use a rescattering model with intermediate scalar states while, finally, Guo and collaborators [136] use the QCDME with an EFT-based treatment of the B meson loops.

In the $\pi\pi$ transition sector there is always at least one theoretical model that seems to properly describe separately each the experimental measurement. However these works are focused either on the transitions below the threshold or on the transitions above the threshold. The only attempt made to apply a unified approach to all the $\pi\pi$ transitions [130] is largely underestimating the widths of the $\Upsilon(4S)$ and $\Upsilon(5S)$ decays. The overall impression is that either we are still lacking a unified approach to all the hadron transitions from the different states due to theoretical incompre-

Table 2.1: Theoretical prediction on the partial widths of the $\pi\pi$ transitions among bottomonium states, from different authors.

Process	[120]	[131]	[132]	[135]	[130]	PDG
$\Upsilon(2S) \to \Upsilon(1S)$	13	0.46 ± 0.33			5.14	5.75 ± 0.47
$\Upsilon(3S) \to \Upsilon(1S)$	1.0	0.68 ± 0.48			1.10	0.89 ± 0.08
$\Upsilon(3S) \to \Upsilon(2S)$	0.3	1.1 ± 0.8			0.26	0.57 ± 0.06
$\Upsilon(4S) \to \Upsilon(1S)$		1.9 ± 1.4		1.47 ± 0.03	1.52	1.7 ± 0.2
$\Upsilon(4S) \to \Upsilon(2S)$		0.02 ± 0.02		1.14 ± 0.22	0.19	1.8 ± 0.3
$\Upsilon(5S) \to \Upsilon(1S)$			1400	327 ± 100	7.15	292 ± 152
$\Upsilon(5S) \to \Upsilon(2S)$			670	422 ± 160	10.5	429 ± 230
$\Upsilon(5S) \to \Upsilon(3S)$			32	319 ± 160	3.19	264 ± 167
$\Upsilon(4S) \to h_b(1P)$						< 8
$\Upsilon(5S) \to h_b(1P)$						193 ± 115
$\Upsilon(5S) \to h_b(2P)$						330 ± 200

Table 2.2: Theoretical prediction on the partial widths of the η transitions among bottomonium states, from different authors.

Process	[40]	[120]	[133]	[135]	[121]	[136]	PDG
$\Upsilon(2S) \to \Upsilon(1S)$ $[\times 10^{-3}]$	14	22	60 ± 40				9.3 ± 1.5
$\Upsilon(3S) \to \Upsilon(1S)$ $[\times 10^{-3}]$		11	3600 ± 2200		20		< 3
$\Upsilon(4S) \to \Upsilon(1S)$			2.3 ± 1.4		6.05		4.0 ± 0.8
$\Upsilon(5S) \to \Upsilon(1S)$			8.8 ± 5.2	$20 - 150$			40 ± 23
$\Upsilon(5S) \to \Upsilon(2S)$				$10 - 100$			209 ± 111
$\Upsilon(4S) \to h_b(1P)$					37.9	≈ 20	
$\Upsilon(5S) \to h_b(1P)$							
$\Upsilon(5S) \to h_b(2P)$							

Table 2.3: Theoretical prediction on the ratios $\mathcal{R}_{\eta,\pi\pi}$ for different transitions among bottomonium states, from different authors.

Process	[40]	[120]	[135]	[121]	PDG
$\Upsilon(2S) \to \Upsilon(1S)$ $[\times 10^{-3}]$	2.3	1.7			(1.6 ± 0.2)
$\Upsilon(3S) \to \Upsilon(1S)$ $[\times 10^{-3}]$		11		25.7	< 2.1
$\Upsilon(4S) \to \Upsilon(1S)$			$1.8 - 4.5$	2.38	2.4 ± 0.5
$\Upsilon(5S) \to \Upsilon(1S)$					0.13 ± 0.10
$\Upsilon(5S) \to \Upsilon(2S)$					0.49 ± 0.37
$\Upsilon(4S) \to h_b(1P)$					
$\Upsilon(5S) \to h_b(1P)$					
$\Upsilon(5S) \to h_b(2P)$					

hensions, or the physical mechanism generating the transition is strikingly different in the two mass regions.

While the transitions from above the threshold seems to be overall well described by the introduction of coupled channel effects, loops or hybrid states as HQSS breaking mechanism in the QCDME, the theoretical landscape is surprisingly confused in the region below the threshold, where these effects are expected to be small and the HQSS should be dominant. For $\Upsilon(3S) \to \Upsilon(1S)$ we observe an overall good description of the dipion transition by different models, while the branching ratio of the η one is systematically overestimated by all the authors. Also in the $\Upsilon(2S)$ case the η transition seems to be generally overestimated, while for the $\pi\pi$ one different predictions, quite far one from the other, are reported. From the point of view of the test of the HQSS, the predictions on $\mathcal{R}_{\eta\pi\pi}$ are expected to be theoretically more precise than the estimation of the partial widths. Indeed in the $\Upsilon(2S)$ case both the prediction are in good agreement with the experimental measurement. In the $\Upsilon(3S)$ however we observe that the η suppression is underestimated by the theory by at least a factor of five. In a recent proposal E.Eichten [137] suggested that the coupled channel effects are negligible only in the $\Upsilon(2S) \to \Upsilon(1S)$ transitions since the $\Upsilon(2S)$ is, among all the bottomonium or charmonium vector states, the only on far enough from the open flavor threshold. Therefore the QCDME free parameters should be fixed using this transition and not, as was historically done, using the $\psi' \to J/\psi$ ones. Extensive theoretical predictions based on this assumption are, unfortunately, still not available at the present time.

While the experimental and theoretical effort on the transitions among spin triplet states produced a quite complete picture, we still have few informations about the transitions among spin triplet and spin singlet states, namely $\Upsilon \to h_b$. The only strong evidences for transitions in this sector are for the $\Upsilon(5S) \to \pi\pi h_b(1P, 2P)$ processes observed by Belle. The same analysis was performed at the $\Upsilon(4S)$, but no evidence for a dipion transition to the $h_b(1P)$ was found. Both the $\pi\pi$ and η transitions among these states are spin-flipping processes, therefore the HQSS would predict branching ratios of the same order of magnitude [15]. The only predictions available are about the $\Upsilon(4S) \to \eta h_b(1P)$. Guo and collaborators [136] suggest a branching ratio of the order of 10^{-3}, and proposed to compare the size of the η and π^0 transitions to estimate the mass difference between the u and d quark. However the π^0 transition is suppressed by the isospin conservation and is beyond the sensitivity of the current data samples. A second calculation is provided by Segovia and collaborators [121], but this result came after a preliminary result from Belle was released, and should therefore be seen as a theoretical confirmation rather than a prediction.

2.3.5 Other open problems in bottomonium physics

In this last part we will collect some other aspect of the bottomonium physics that have not been discussed so far, but that are faced by our experimental work.

The $h_b(1P) \to \gamma\eta_b(1S)$ transition and the $\eta_b(1S)$ hyperfine splitting puzzle

In the discussion of the relativistic corrections to the potential model, we highlighted that the hyperfine splittings are extremely sensitive to the Lorentz structure of the potential, in particular to the presence of a non-scalar long range potential and to the value of the radial wavefunction evaluated at $r = 0$. For these reasons this quantity has been object of countless theoretical predictions from many different groups using differ-

---

[15] Actually the η transition is expected to be always suppressed with respect to the $\pi\pi$ one not only by the HQSS breaking, but also by the $SU(3)_{flavor}$ breaking effects.

ent models, since the early days of quarkonium physics [16]. The spin triplet states, $\Upsilon(nS)$ and $\chi_b(mP)$ are well known and their masses have been precisely measured. Therefore the challenge of the measurement of the hyperfine splitting is basically a problem of identification and measurement of the parameters of the spin singlet states, $\eta_b(mS)$ and $h_b(mP)$ We saw that the $h_b(1P, 2P)$ were only recently accessed trough dipion transitions from the $\Upsilon(4S, 5S)$. The ground state $\eta_b(1S)$ can be produced at e^+e^- colliders either by the transition $\Upsilon(mS) \to \gamma\eta_b(nS)$ or by $h_b(mP) \to \gamma\eta_b(nS)$. In the QED multipole expansion at the leading order $\Upsilon(mS) \to \gamma\eta_b(nS)$ is an M1 transition, whose amplitude is suppressed by a factor $1/m_b^2$ [139]:

$$\Gamma(\Upsilon(nS) \to \gamma\eta_b(mS)) = \frac{4}{3}k^3\alpha\frac{e_b^2}{m_b^2}(< f|j_0(kr/2)|i >)^2,$$

where k is the photon momentum, e_b and m_b are respectively the b quark charge and mass, α is the fine-structure constant, and $< f|j_0(kr/2)|i >$ accounts for the overlap of the initial and final states wave functions. Despite the low branching fraction, compensated by the large data samples of $\Upsilon(2S, 3S)$ collected by the B-factories and by CLEO, these transitions were first used to study the $\eta_b(1S)$ and measure its mass.

Experimental measurements based on the electric-dipole transitions $h_b(1P, 2P) \to \gamma\eta_b(1S, 2S)$ became possible only recently, with the discovery of the $\Upsilon(5S) \to \pi\pi h_b(1P, 2P)$ transitions [141]. In this case the transition amplitude is much large than in the M1 case, with

$$\Gamma(h_b(nP) \to \gamma\eta_b(mS)) = \frac{4}{9}k^3\alpha e_b^2(< f|r)|i >)^2,$$

corresponding to the branching ratio estimation $\mathcal{B}[h_b(1P) \to \gamma\eta_b(1S)] = (35 \pm 8)\%$ [140]. The experimental measurement by Belle of $(49 \pm 8)\%$

---

[16] The works by Godfrey and Rosner report a nice summary of the theoretical predictions made before the year 2000 on the hyperfine splittings in the S and P wave systems

[142] is barely compatible with this prediction. Later studies including hadronic loop corrections [143] seems to be able to reduce this discrepancy, but still further experimental confirmations are required.

Concerning the measurement of the $\eta_b(1S)$ mass, a 3σ-level discrepancy between the result obtained in the $E1$ and the ones from the $M1$ processes is present, and yet not completely understood. Figure 2.15 shows the comparison between the different measurements and some of the most recent theoretical predictions.

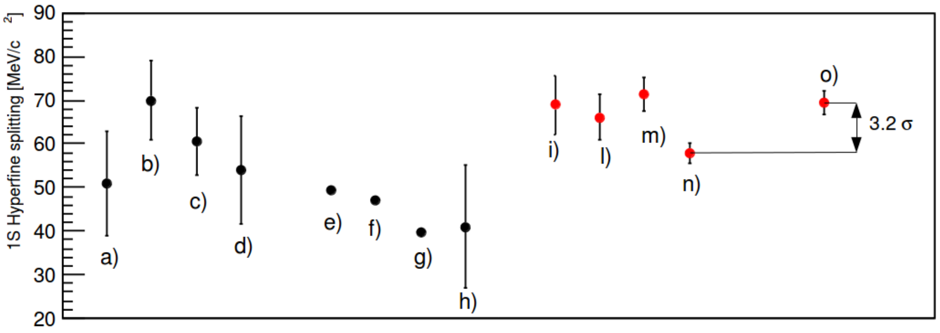

Figure 2.15: Summary of the experimental measurements of the $1S$ hyperfine splitting in bottomonium (red dots), compared with a selection of the most recent theoretical predictions (black dots). The theoretical prediction are: a) Aarts et al. (2014) [144], b) Dowdall et al. (2012) [145], c) Meinel (2012) [146], d) Burch et al. (2010) [147], e) Wei-Zhao et al. (2013) [148], f) Gupta et al. (1994) [149], g) Radford and Repko (2007) [150], h) Kniehl et al. (2004) [151]. The experimental measurements are: i) CLEO collaboration (M1 transition $\Upsilon(3S) \to \gamma\eta_b(1S)$) [152], l) BaBar Collaboration (M1 transition $\Upsilon(3S) \to \gamma\eta_b(1S)$) [153], m) BaBar Collaboration (M1 transition $\Upsilon(2S) \to \gamma\eta_b(1S)$) [154], n) Belle Collaboration (E1 transitions $h_b(1P, 2P) \to \gamma\eta_b(1S)$) [142]. The last point, o) is the average of the measurements obtained using the M1 transitions.

The $\Upsilon(1D)$ triplet

Chapter 3

Montecarlo studies

The primary scope of this work is to search for the new processes $\Upsilon(4,5S) \to \eta h_b(1,2P)$ and, exploiting the subsequent radiative transitions $h_b(1P,2P) \to \gamma\eta_b(1S,2S)$, to measure the mass and width of the bottomonium ground state.

This chapter is devoted to the description of the analysis strategy and the selection criteria adopted for the search of η transitions among $\Upsilon(4S,5S)$ and the lower bottomonium states, as well as the E1 radiative transition between parabottomonia $h_b(1P) \to \gamma\eta_b(1S)$.

3.1 Analysis overview

The search for η transitions from $\Upsilon(4S,5S)$ to spin singlet bottomonium states is particularly challenging. No $h_b(1,2P)$ exclusive decay modes are known to have a large branching fraction or a clear experimental signature, thus a full reconstruction of the final state is not possible and the analysis must be performed inclusively. Since these transitions are two body processes, their signature is the emission, in the $\Upsilon(4S,5S)$ reference frame, of a mono-energetic η meson, eventually associated to an almost mono-energetic photon due to the $h_b(nP) \to \gamma\eta_b(mS)$ transition. The energy distribution of photon is not monochromatic as the initial η transition and will boost the h_b rest frame. This doppler shift prevents to have a simple Gaussian peak in the inclusive photon energy spectrum.

Instead of studying the η and γ energy spectrum in the Center of Mass frame, we use the *recoil mass* or *missing mass* technique which has been successfully exploited in previous Belle analyses [141, 142] and allows to study both single and cascade decays. The η meson is reconstructed in the two dominant decay modes $\eta \to \gamma\gamma$ and $\eta \to \pi^+\pi^-\pi^0$, therefore the inclusive η and $\eta\gamma$ recoil mass spectrum is expected to be dominated by a large, smooth background distribution due either to random $\gamma\gamma$ and $\pi^+\pi^-\pi^0$ combinations or real η arising from background processes. The description of the stategies adoped for the reduction of this combinatorial backgroud will be the main subject of this chapter. We will first describe how the ECL cluster associated to photons are distinguisched from spurious ECL clusters due to the soft beam activity, the hadronic interactions, the electronic noise or the reconstruction-induced artifacts. We will show that the π^0 reconstruction plays a crucial role not only for the $\eta \to 3\pi$ mode but also for the $\eta \to \gamma\gamma$ reconstruction, since photons arising from π^0 decays are likely to be a major source of background in the $\eta \to \gamma\gamma$ reconstruction, requiring a dedicated veto algorithm. At $\Upsilon(4S)$ and $\Upsilon(5S)$ energy the largest fraction of the hadronic evens is due to the non resonant reaction $e^+e^- \to q\bar{q}$, therefore an event selection based on the topology of the final state will be implemented in order to select only the event likely to be associated to a gluon fragmentation.

The radiative corrections to the production of $\Upsilon(4S, 5S)$, which are known to distort the monochromatic η recoil mass peaks, will be modeled and included in the analysis. Finally, in order to precisely measure the $\eta_b(nS)$ mass and width, the absolute photon energy calibration must be studied in details using control samples as $\pi^0 \to \gamma\gamma$, $D^{*0} \to \gamma D^0$ and $\eta \to \gamma\gamma$

itself.

In principle many η transitions are expected to produce peaking structures in the η recoil mass, as well as different radiative transitions could be seen in the $\eta\gamma$ recoil spectrum, as shown in Figure 3.1. The transtions to $h_b(1P, 2P)$ are the primary target of this analysis. As we reported in the previous chapter, the $\Upsilon(5S) \to \eta\Upsilon(1S, 2S)$ and $\Upsilon(4S) \to \eta\Upsilon(1S)$ reactions have been observed and may serve as validation of the analysis procedure. The transitions to and from the $\Upsilon(1D)$ triplet have not been observed, but are favored by the quantum numbers and therefore included in our analysis. Finally we also consider $\chi_{b0}(2P) \to \eta\eta_b(1S)$ since it has been proposed as gateway to the $\eta_b(1S)$. The $\Upsilon(1D)$ can be produced by either double radiative cascades through the $\chi_{bJ}(2P, 3P)$ states or via di-pion transitions, while the $\chi_{b0}(2P)$ can result from unobserved radiative decays

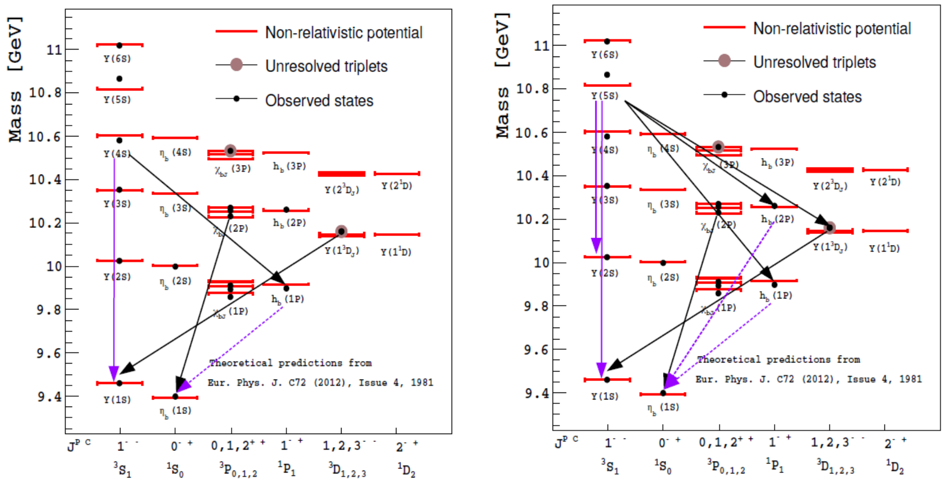

Figure 3.1: *Left:* Radiative (dashed) and η (solid) transitions that can appear in the recoil spectra at the $\Upsilon(4S)$ energy. The black lines indicate unobserved transitions, while the purple one refers to known processes. *Right:* The transition pattern at the $\Upsilon(5S)$ energy.

of $\Upsilon(4S,5S)$. The complete list of transition assumed in this analysis is:

$$\begin{aligned}
&\Upsilon(5S) \to \eta h_b(2P)[\to \gamma\eta\eta_b(1S,2S)]\\
&\Upsilon(5S) \to \eta h_b(1P)[\to \gamma\eta\eta_b(1S)]\\
&\Upsilon(5S) \to \eta\Upsilon(1D)\\
&\Upsilon(5S) \to \eta\Upsilon(2S)\\
&\Upsilon(5S) \to \eta\Upsilon(1S)\\
&\Upsilon(4S) \to \eta h_b(1P)[\to \gamma\eta\eta_b(1S)]\\
&\Upsilon(4S) \to \eta\Upsilon(1S)\\
&\Upsilon(4S) \to \gamma\gamma\Upsilon(1D) \to \gamma\gamma\eta\Upsilon(1S)\\
&\Upsilon(4S) \to \gamma\chi_{b0}(2P) \to \gamma\eta\eta_b(1S)
\end{aligned}$$

In addition to the transitions reported above, the $\Upsilon(2S) \to \eta\Upsilon(1S)$ could appear. However, given the low branching fraction for this transition combined with the low yield of $\Upsilon(2S)$ arising from either hadronic transitions or initial state radiation production, we don't expect any significant signal and we neglect this contribution.

We will now review some theoretical aspects of the analysis, describing in detail the kinematic calculations involved in missing mass technique and the impact of the radiative corrections to the $\Upsilon(4S,5S)$ production. A final paragraph will be devoted to the description of the statistical methods used for the calculation of significances and upper limits.

3.1.1 The missing mass technique

The missing mass technique is widely used in the study of hadronic transitions among quarkonia when the full reconstruction of the final state is not possible.

In order to describe this method, let us assume the process

$$e^+e^- \to A \to hB \to X,$$

where A and B are heavy mesons, h is an hadronic state constituted by one or more light hadrons that subsequently decay[1]. The final state X consists in n stable or semi-stable particles[2] arising from both the decay of h and B. Among all these tracks, we are interested only in measuring the momenta of the n_r arising from the decay of h, so that the 4-momentum $P_h = \sum_{i=0}^{i<n_r} P_i$ is known. If also the 4-momentum P_{in} of the initial e^+e^- pair is known the total 4-momentum of the not reconstructed part P_{miss} , corresponding to the 4-momentum of B P_B, can be written as :

$$P_{miss} = P_{in} - P_h.$$

Therefore the invariant mass of B $M_B^2 = (P_{in} - P_h)^2$ can be measured neglecting the B decay products and reconstructing only a small fraction of the event, with a dramatic increase of the overall reconstruction efficiency. For example, in the search for $\Upsilon(4S, 5S) \to \eta(b\bar{b})' \to \eta X$ the signals appear as Gaussian-like peaks in the $M_{miss}(\eta)$ distribution, over a large smooth background resulting from both mis-reconstructed η and real η emerging from the $(b\bar{b})'$ hadronization. While the central values of these peaks is uniquely determined by the invariant mass of the bottomonium state B produced in the transition, their width is the result of a non-trivial combination of different effects. Here we will assume the simple case in which B has negligible natural width, which is the case for all the transitions considered in this analysis. In order to explicitly separate the different resolution contribution, it's first convenient to re-write M_{miss}^2 in the CM frame, where $P_{in}^* = (\sqrt{s}, \vec{0})$ and $P_h^* = (E_h^*, \vec{p}_h^*)$, as function of $\sqrt{s}$, $\vec{p}_h^* = \sum_{i=0}^{i<n_r} \vec{p}_i^*$ and $E_h^* = \sum_{i=0}^{i<n_r} \sqrt{p_i^{*2} + m_i^2}$ (from here until the end of the paragraph we will omit the CM notation, and all the variables will be understood to be

---

[1] Typically $h = \eta, \pi^0, \omega, (\pi^0\pi^0), (\pi^+\pi^+)$

[2] For the kinematic condition of a B-factory, $\mu^\pm$, $\pi^\pm$, $K^\pm$ and K_L can be assumed to be stable, since they are likely to either leave the detector or interact with it before decaying.

expressed in the center of mass of the e^+e^- pair):

$$M^2_{miss} = E^2_h - \vec{p}^2_h + \sqrt{s}^2 - 2\sqrt{s}E_h.$$

Therefore, applying the usual rules for the propagation of Gaussian uncertainties, we can obtain:

$$\sigma^2_{M^2_{miss}} = (2E_h\sigma_{E_h})^2 + (2p_h\sigma_{p_h})^2 + (2\sqrt{s}\sigma_{\sqrt{s}})^2 + (2\sqrt{s}\sigma_{E_h})^2 + (2E_h\sigma_{\sqrt{s}})^2,$$

where σ_x is the error on x. In order to further separate the different contributions, the expression obtained above can be further re-written as function of the momenta p_i of the reconstructed particles and their variances $\sigma^2_{p_i}$. Since $\sigma^2_{E_h} = \sum_{i=0}^{i<n_r} \sigma^2_{p_i} \frac{{p_i}^2}{m_i^2+{p_i}^2}$ and $\sigma^2_{p_h} = \sum_{i=0}^{i<n_r} \sigma^2_{p_i}$, the total uncertainty on M^2_{miss} is:

$$\sigma_{M^2_{miss}} = (4({E_h}^2 + s) \sum_{i=0}^{i<n_r} \frac{{p_i}^2}{m_i^2 + {p_i}^2} + {p_h}^2)\sigma^2_{p_i} + 4({E_h}^2 + s)\sigma^2_{\sqrt{s}},$$

where the contributions due to the tracking of calorimetric performances are finally separated from the contribution due to the beam energy resolution. While all the single uncertainties have a clear meaning, $\sigma_{\sqrt{s}}$ should be interpreted as the uncertainty on the mass of the initial state, which is related to both the beam energy resolution and the natural width of the initial state. If the initial state us much broader than the beam energy spread σ_{beam}, like in the case of $\Upsilon(4S)$, this is the main contributor to the uncertainty on the initial state kinematics and $\sigma_{\sqrt{s}} \approx \sigma_{beam}$. In the case of a narrow state such $\Upsilon(2S)$, on the contrary, $\sigma_{\sqrt{s}}$ should be replaced by the natural with $\Gamma_{\Upsilon(2S)} = 23\ \mathrm{KeV}/c^2$, making the correspondent contribution in the error budget negligible. If the investigated process is a two body decay like in our case, an additional mass constraint on P_h can be applied with a kinematic fit, resulting in an effective reduction of the σ_{p_i} and an improvement in the recoil mass resolution. Figure 3.2 shows the impact of a kinematic fit which constrains the $\gamma\gamma$ pair invariant mass to the η mass value on the η recoil mass resolution in $\Upsilon(4S) \to \eta[\to \gamma\gamma]h_b(1P)$ simulated events. Thanks to the kinematic fit the resolution on M_{miss} can be improved by a factor 3.

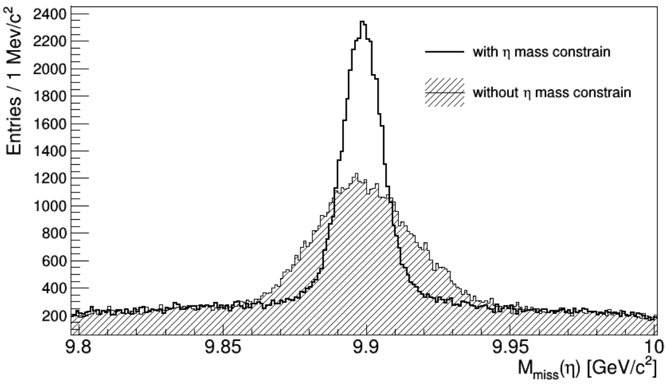

Figure 3.2: η recoil mass in $\Upsilon(4S) \to \eta[\to \gamma\gamma]h_b(1P)$ MC events. The Gaussian-like peak is due to the η emitted in the transition, while the smooth background is due to η mesons produced in the $h_b(1P)$ annihilation. The Gaussian resolution archived constraining the η mass is $\sigma_f = 7$ MeV$/c^2$, while without the constraint we obtain $\sigma_{nf} = 20$ MeV$/c^2$.

Under certain approximations, the recoil mass method can be also applied to cascade processes $H \to xH^{'} \to xyH^{''}$, where x and y are either photons or hadrons emitted by two consecutive transitions and H, $H^{'}$ and $H^{''}$ are heavy mesons. In those cascade processes it's possible to construct, starting from the 4-momenta of x and y, two missing masses variables with well determined value: $M_{miss}(x) = M_{H'}$ and $M_{miss}(yx) = M_{H''}$. Therefore a signature for the full decay chain $(b\bar{b}) \to X(b\bar{b})^{'} \to XY(b\bar{b})^{''}$ can be searched study the distribution of $M_{miss}(x)$ as function of $M_{miss}(xy)$, where the signal would appear as a 2D Gaussian-like structure.

Unfortunately the fit of $M_{miss}(x)$ in bins $M_{miss}(xy)$ is problematic since in general these two variables are strongly correlated, as shown in Figure 3.3

and as appears in the explicit expression of $M_{miss}(xy)$:

$$M_{miss}(xy) = \sqrt{(P_{in} - P_x - P_y)^2} = \sqrt{M_{miss}(x)^2 + m_y^2 - 2P_{miss}(x)P_y}.$$

However, we will show that under certain approximations this dependence can be largely mitigated. In particular, we will focus on the case in which $m_H - m_{H'} \approx m_x$, $m_{H'} \approx m_{H''}$ and $m_{H'} >> m_y$. These are the conditions met by the $\Upsilon(4S) \to \eta h_b(1P) \to \eta\gamma\eta_b(1S)$ transitions.
First, we construct the invariant quantity $\Delta M_{miss} = M_{miss}(xy) - M_{miss}(x)$, and by substituting the explicit expression of $M_{miss}(xy)$ and $M_{miss}(x)$ in the CM frame we obtain

$$\Delta M_{miss} = M_{miss}(x)\sqrt{1 + \frac{m_y^2}{M_{miss}^2(x)} - \frac{2P_{miss}(x)P_y}{M_{miss}^2(x)}} - M_{miss}(x).$$

Since by construction $M_{miss}(x) = M_{H'}$, if the condition $m_{H'} >> m_y$ is met we can neglect the term $\frac{m_y^2}{M_{miss}^2(x)}$, obtaining the simplified expression

$$\Delta M_{miss} \approx M_{miss}(x)\sqrt{1 - \frac{P_{miss}(x)P_y}{M_{miss}^2(x)}} - M_{miss}(x).$$

A further approximation is possible if $\frac{P_{miss}(x)P_y}{M_{miss}^2(x)} << 1$. To see in which conditions this quantity is small, we first write it explicitly:

$$\frac{P_{miss}(x)P_y}{M_{miss}^2(x)} = \frac{E_{miss}(x)E(y) - \vec{p}_{miss}(x)\cdot\vec{p}(y)}{M_{miss}^2(x)} = \frac{E_{miss}(x)E(y)}{M_{miss}^2(x)} - \frac{\vec{p}_{miss}(x)\cdot\vec{p}(y)}{M_{miss}^2(x)}.$$

We can now observe that if $m_H - m_{H'} \approx m_x$, which implies $p_{miss}(x) << E_{miss}(x) \approx M_{miss}(x)$, and $m_{H''} \approx m_{H'}$, which implies $E_y << M_{miss}(x)$, this ratio is expected to be much smaller than 1. Indeed in the transitions we are going to analyze in this work $\frac{P_{miss}(x)P_y}{M_{miss}^2(x)} \approx 0.1$ and a Taylor series expansion can be applied, obtaining the approximate expression 3.4.

$$\Delta M_{miss} \approx M_{miss}(x) - \frac{P_{miss}(x)P_y}{M_{miss}(x)} - M_{miss}(x) = -\frac{2P_{miss}(x)P_y}{M_{miss}(x)},$$

or, explicitly

$$\Delta M_{miss} = \frac{E_{miss}(x)E_y - \vec{p}_{miss}(x) \cdot \vec{p}_y}{M_{miss}(x)} = \frac{E(y)(E_{miss}(x) - p_{miss}(x)\cos\theta_{miss,y})}{M_{miss}(x)},$$

where $\cos\theta_{miss,y}$ is the angle between the x and y missing momenta. Since our scope is to determine whatever the central value of the ΔM_{miss} depends on $M_{miss}(x)$ we can eliminate the dependence on $\cos\theta_{miss,y}$ performing an integration over $\theta_{miss,y}$ and obtaining the average value:

$$< \Delta M_{miss} > \approx E(y)\frac{E_{miss}(x)}{M_{miss}(x)}.$$

Assuming $m_{h_b(1P)} = 9.900$ GeV$/c^2$ and $m_{\eta_b(1S)} = 9.400$ GeV$/c^2$, a variation of 10 MeV$/c^2$ in $M_{miss,\eta}$, which is of the same order of the experimental resolution, corresponds to a variation of the order of 0.1 MeV$/c^2$ on the central value of ΔM_{miss}, far below the expected experimental resolution. Figure 3.4 shows a Toy-MC simulation for the distribution of ΔM_{miss} as function of M_{miss} in $\Upsilon(4S) \to \eta h_b(1P) \to \eta\gamma\eta_b(1S)$. .

3.1.2 Initial State Radiation corrections

The production of a vector state V in e^+e^- collision at $\sqrt{s} \approx 10$ GeV can be completely described neglecting the small contribution due the Z boson exchange as a pure electromagnetic process. If the radiative corrections consisting in the emission of photons in the initial state are neglected, this interaction can be represented by the Feynman diagram in Figure 3.5. The corresponding cross section can be obtained using the Breit-Wigner

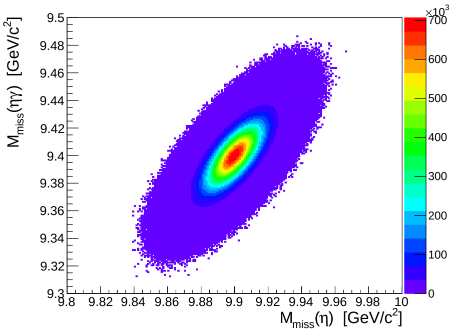

Figure 3.3: $M_{miss}(\eta\gamma)$ as function of $M_{miss}(\eta)$ in simulated $\Upsilon(4S) \to \eta h_b(1P) \to \eta\gamma\eta_b(1S)$ events.

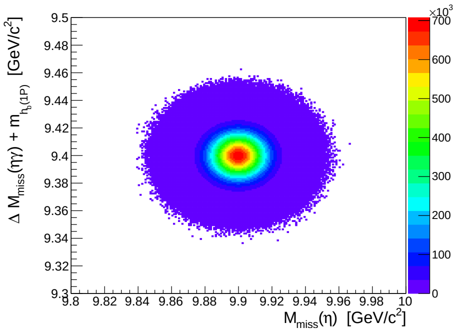

Figure 3.4: $\Delta M_{miss}(\eta\gamma)$ as function of $M_{miss}(\eta)$ in simulated $\Upsilon(4S) \to \eta h_b(1P) \to \eta\gamma\eta_b(1S)$ events. For convenience the $\Delta M_{miss}(\eta\gamma)$ value is shifted by $m_{h_b(1P)}$.

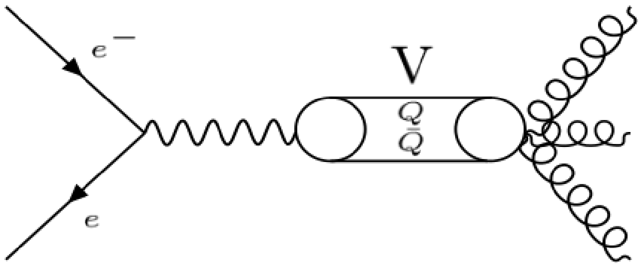

Figure 3.5: Feynman diagram for the reaction $e^+e^- \to V$ at the tree-level

formula

$$\sigma_0(s) = \frac{12\pi B_{ee}}{m_V^2} \frac{m_V^2\Gamma_V^2}{(s - m_V^2)^2 - m_V^2\Gamma_V^2},$$

where $\sqrt{s}$ is the CM energy of the e^+e^- pair, B_{ee} is the branching ratio of the decay $V \to e^+e^-$, and Γ_V is the total width of the vector state and m_V is its mass.

At the first order, the process is described by Feynman diagram of the class shown in Figure 3.6, where a real photon with energy E_γ is emitted by either the electron or the positron in the initial state, resulting in a decrease of the effective energy in the e^+e^- center of mass to the value $\sqrt{s}' = \sqrt{s}(1 - E_\gamma/\sqrt{s})$. Therefore the direct production of vector states

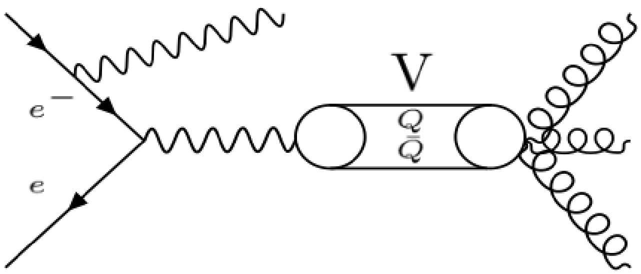

Figure 3.6: Feynman diagram of the first order radiative correction to the reaction $e^+e^- \to V$

with mass much lower than $\sqrt{s}$ can occur at e^+e^- collider through the process $e^+e^- \to \gamma V'$. This effect, known as initial state radiation (ISR), allowed to perform many studies on charmonium production at B-Factories [155]. For such events, in which $\sqrt{s} \approx 10$ GeV and $\sqrt{s}' \approx 4$ GeV, already the first order corrections in α give a satisfactory agreement with the data. At this order the formula for the cross section $\sigma_1(s,x)$ is factorized in two parts, one accounting for the emission of a photon of energy E_γ with direction $\cos(\theta)$ with respect to the beam direction, usually expressed as function of $x = E_\gamma/\sqrt{s}$, and one accounting for the production of the resonant state at the energy $\sqrt{s}(1 - E_\gamma/\sqrt{s})$:

$$\frac{d\sigma_1}{d\cos\theta dx} = \frac{2\alpha}{\pi x}\frac{(1 - x + x^2/2)\sin^2\theta}{(\sin^2\theta + \frac{m_e^2}{E^2}\cos^2\theta)^2} \cdot \sigma_0(s(1-x)),$$

where E is the energy of the electron (or positron) in the e^+e^- CM frame, $s = 4E^2$, and m_e is the electron mass. If the detection of the photon inside the detector volume is not required, we can integrate over all the possible emission angle and introduce the *radiator function* $W(s,x)$ defined as

$$W(s,x) = \int_{-1}^{1} d\cos\theta \frac{ds_1}{d\cos\theta dx} = \frac{2\alpha}{\pi x}(2\ln\frac{\sqrt{s}}{m_e} - 1)(1 - x + x^2/2).$$

The differential cross section can be thus rewritten as

$$\frac{d\sigma_1}{dx} = W^I(s,x) \cdot \sigma_0(s(1-x)).$$

We see that the radiative correction is completely determined by the behavior of the radiator $W^I(s,x)$, that can be interpreted as a probability density function for the emission of a photon with fractional energy x.
This approximation, already suitable for the description of the production of states with mass much lower than $\sqrt{s}$, fails to model the emission of soft photons, since $W(s,x)$ is both infrared divergent and not-integrable over the whole x domain. This effect is particularly important for the study of $\Upsilon(5S)$ and $\Upsilon(4S)$ decays: even with $\sqrt{s} = m_{\Upsilon(nS)}$, the large natural width of these states allow the process $e^+e^- \to \gamma_{soft}\Upsilon(nS)$, with $E_{\gamma_{soft}} \approx 10$ MeV, to occur, resulting in the production of an $\Upsilon(4S,5S)$ states with boost different from the nominal value of the e^+e^- pair. This distortion of the initial kinematics reflects in a distorted shape of the recoil mass peaks in the two body decays of such states, and is thus relevant to our analysis. The soft ISR emission is better modeled by the next-to-next-to-leading-order (NNLO) formula for the production cross section:

$$\frac{d\sigma_2}{dx} = W^{II}(s,x) \cdot \sigma_0(s(1-x)),$$

where the second order radiator $W^{II}(s,x)$ can be expressed as

$$W^{II}(s,x) = (\Delta\beta x^{\beta-1} + \frac{\beta^2}{8}((2-x)(3\ln(1-x) - 4\ln x) - 4\frac{\ln(x-1)}{x} - 6 + x)) \cdot \sigma_0(s(1-x))$$

with

$$\begin{aligned}
&\Delta = 1 + \tfrac{\alpha}{\pi}(3L/2 + \pi^2/3 - 2) + \tfrac{\alpha^2}{\pi^2}\delta_2,\\
&\delta_2 = (\tfrac{9}{8} - 2\zeta_2)L^2 - (\tfrac{45}{16} - \tfrac{11}{2}\zeta_2 - 3\zeta_3)L - \tfrac{6}{5}\zeta_2^2 - \tfrac{9}{2}\zeta_3 - 6\zeta_2 \ln 2 + \tfrac{3}{8}\zeta_2 + \tfrac{57}{12},\\
&\beta = \tfrac{2\alpha}{\pi}(L-1),\\
&L = 2\ln\tfrac{\sqrt{s}}{m_e},\\
&\zeta_2 = 1.64493407, \zeta_3 = 1.2020569.
\end{aligned}$$

Figure 3.9 shows the behavior of the LO and NLO radiator[3]

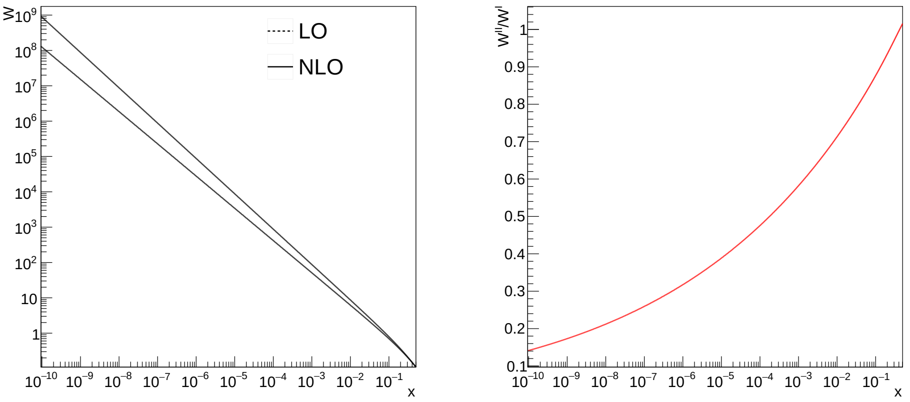

Figure 3.7: *Left:* shape of the radiator functions at the LO (W^I) and NLO (W^{II}) ISR, as function of $x = E_\gamma/\sqrt{s}$. *Right:* Ratio between W^I and W^{II}, as function of x. The α^2 corrections are particularly important in the soft emission regime, while for $x > 0.1$ the LO ISR formula is already precise within 10%.

In order to study, as an example, the cross section for the $\Upsilon(4S)$ in e^+e^- collision at its mass, we assume that σ_0 can be modeled in the Breit-Wigner approximation by the expression

$$\sigma_0(x) = \frac{12\pi B_{ee}}{m^2_{\Upsilon(4S)}} \frac{m^2_{\Upsilon(4S)}\Gamma^2_{\Upsilon(4S)}}{(s(1-x) - m^2_{\Upsilon(4S)})^2 - m^2_{\Upsilon(4S)}\Gamma^2_{\Upsilon(4S)}},$$

---

[3] The radiator itself appears as a NLO correction to the cross section. For this reason we will refer to expression at order α as either the NLO cross section or the LO ISR cross section, while the α^2 approximation will be called either NNLO cross section or NLO ISR. Following this convention, we will refer to the radiator expression at the order α as LO radiator, and to the one at the order α^2 as NLO radiator.

where s is the CM energy of the beams $s = 10.580^2\ \text{GeV}^2$, $B_{ee} = 1.57 \times 10^{-5}$ is the branching ratio of $\Upsilon(4S) \to e^+e^-$, and $\Gamma_{\Upsilon(4S)} = 20.5\ \text{MeV}/c^2$ is the total $\Upsilon(4S)$ width. The behavior of the differential cross section for $\Upsilon(4S)$ production is shown in Figure 3.8. We must point out that x cannot be defined at the LO since there is no photon emission by construction, therefore the shape reported in the figure should be interpreted as the result of an energy scan in which the beam energy is shifted from $\sqrt{s} = 10.580\ \text{GeV}/c^2$ to the new energy $\sqrt{s}'$, corresponding to $x = \frac{\sqrt{s}-\sqrt{s}'}{\sqrt{s}}$. Even at the α^2 order, the radiator is still divergent for $x \to 0$ but, unlike what happens at the $O(\alpha)$ approximation, it remains integrable over it full domain. Therefore it's possible to perform numerical calculations of the total cross sections. In order to estimate the $\Upsilon(4S)$ line-shape distortion, we replace σ_2 with the

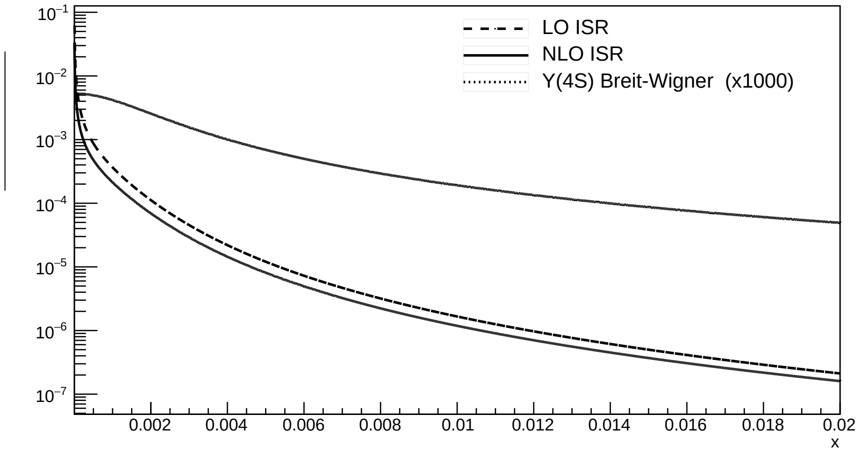

Figure 3.8: Differential cross section of the process $e^+e^- \to \Upsilon(4S)$ at LO, NLO and NNLO approximation in α. The variable x is should be interpreted as the fraction energy of the ISR photon in the case of the NLO and NNLO expression, and as the fractional shift of the incoming e^+e^- pair energy in the CM frame in the case of the LO expression.

modified expression

$$\tilde{\sigma_2} = \begin{cases} \sigma_2, & \text{if } x > \epsilon \\ \frac{1-\int_\epsilon^{+\infty} dx\sigma_2}{\epsilon}, & \text{if } 0 < x < \epsilon \end{cases}$$

which is used in a toy-MC generator which simulates the combined effect of the ISR, the $\Upsilon(nS)$ line-shape, and the beam energy resolution. The result of the simulation is shown in Figure **??**, where we assumed a beam energy resolution of 5 MeV and we use $\epsilon = 10^{-5}$. A detailed discussion on the impact of the radiative corrections to our analysis is presented in the next chapter.

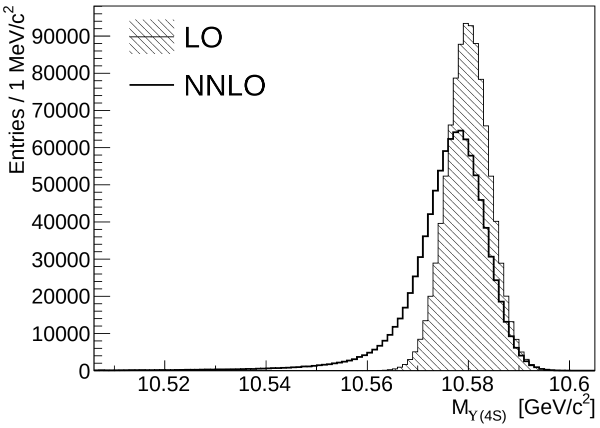

Figure 3.9: $\Upsilon(4S)$ line-shape in e^+e^- collisions with energy in the CM of $\sqrt{s} = 10.580 \pm 0.005$ GeV$/c^2$, assuming either the LO or the NNLO cross section formula. The $\Upsilon(4S)$ is modeled as a Breit-Wigner resonance with $M = 10.580$ GeV$/c^2$ and $\Gamma = 20.5$ MeV$/c^2$, where the beam energy spread is assumed to be Gaussian. 10^6 events are generated for the two cases.

3.1.3 Event shape observables

In e^+e^- collisions at the center of mass energy of few GeV, multi-hadronic final states can be produced either by the non-resonant production of quark-anti-quark pairs via the electromagnetic process $e^+e^- \rightarrow$

$q\bar{q}$, where $q = u, d, s, c$, or by the annihilation of resonant heavy quarks bound states $Q\bar{Q}$ [4]. In the former case the hadrons are produced by the hadronization of the two quarks which are emitted back-to-back in the CM frame, while in the latter case the annihilation is more likely to produce an intermediate gluonic final state with either two or 3 gluons, according to the resonance's quantum numbers. Both $\Upsilon(nS)$ and $h_b(nP)$ annihilates predominantly into 3 gluons, while the $\eta_b(nS)$ can annihilate only in two. Events involving gluon or light quark hadronization can be distinguished based on their topology: an high momentum quark pair is likely to produce two jet-like structures in the detectors, with the final state hadrons being emitted predominantly along the original $q\bar{q}$ pair momentum direction, while hadrons from gluon hadronization do not exhibit a preferred emission direction, giving origin to a rather homogeneous angular distribution of final state particles.
At the $\Upsilon(4S)$ and $\Upsilon(5S)$ energies, the cross section of the $e^+e^- \to q\bar{q}$ reaction is much larger than the cross section for the resonant proceeds, thus the rejection of the continuum based on the event topology is a fundamental part of our study.

The use of event-shape observables [156] to distinguish between quark and gluon hadronization was introduced in the '70, when the search for gluon-induced jets was carried at e^+e^- collider with CM-energy of few tens of GeV as proof of the existence of the gluon itself [157]. Many different observables have been constructed by different authors [158, 159, 160, 161]: sphericity, aplanarity, thrustness, multipole moments and Fox-Wolfram moments [162] are among the most widely used and the ones that will be considered for this study. We will now give a brief review of the main properties of these variables.

The thrust is perhaps the oldest event shape observable. Given an event

---

[4] Since now we will refer to the $e^+e^- \to q\bar{q}$ reaction as *continuum* or *non-resonant*, and to $e^+e^- \to (b\bar{b})$ as *resonant* process.

with N particles (or photons) in the final state, each one with 3-momentum $\vec{p}_i$, and an arbitrary versor $\vec{n}$ we define the quantity $\tilde{T}$ as the normalized sum of the projections of the particle momenta along the direction $\vec{n}$

$$\tilde{T}(\vec{n}) = \frac{\sum_i |\vec{n} \cdot \vec{p}_i|}{\sum_i |\vec{p}_i|}.$$

The direction $\vec{n} = \vec{v}_T$ which maximizes $\tilde{T}$, and the correspondent value $T = \tilde{T}(\vec{v}_T)$ are called thrust axis and thrust of the event:

$$T(\vec{v}_T) = \max_{|v_T|=1} \frac{\sum_i |\vec{v}_T \cdot \vec{p}_i|}{\sum_i |\vec{p}_i|}.$$

We see that the thrust axis is defined such that the projection of the final state particle's momenta along it is maximized, so that, in an ideal di-jet event, it coincides with the di-jet axis. The shape of the event is then determined by the value of T, which is by construction limited between 0 and 1. A jet-like event has $T \to 1$, while lower values of T are connected with spherical events. Using the plane defined by the thrust axis, it is possible to define two additional parameters, here called M_M and M_m, respectively connected to the mayor and minor axis of the event. The major axis $\vec{v}_M$ is constructed with the same approach of the thrust axis, but using the particle momenta projection over the thrust plane. The major axis is thus, by construction, perpendicular to $\vec{v}_T$ and can be seen as an analogous of the thrust axis, but restricted on the transverse plane:

$$M_M(\vec{v}_M) = \max_{|v_M|=1, v_M \cdot v_T = 0} \frac{\sum_i |\vec{v}_M \cdot \vec{p}_i|}{\sum_i |\vec{p}_i|}.$$

The axis perpendicular to both v_M and v_T is called minor axis $\vec{v}_m$, and its correspondent event-shape observable, M_m can be calculate with the same algorithm. The three versors $\vec{v}_T$, $\vec{v}_M$ and $\vec{v}_m$ and the three scalars T, M_M and M_m define an ellipsoid in the momentum space, with an orientation with respect to the beam axis direction $\vec{z}$ given by $\cos\theta_{BA} = \vec{v}_T \cdot \vec{z}$. A perfectly spherical event is thus characterized by $T = M_M = M_m$ and a flat distribution of $\cos\theta_{BA}$. A di-jet like event will have $T > M_M$ and $M_M = M_m$, and the orientation of the thrust axis will be distributed according to the direction of the original $q\bar{q}$ pair, with $\cos\theta_{BA} \propto 1 + \cos^2\theta_{BA}$. Finally, a planar event will exhibit $T > M_M > M_m$. However in real conditions the quark fragmentation tends to broaden the jets, the detector acceptance distances the distributions and, especially at low energies, the limited number of particles per jet introduces large event-by-event fluctuations. Furthermore, the algorithm for the search of the thrust axis is both computationally demanding and does not grant the convergence to the real maximum, thus particular care is needed when using these observables.

An alternative approach to the study of the event shape is based on the construction of a symmetric tensor

$$S^{\alpha\beta} = \frac{\sum_i}{p_i^{\alpha} p_i^{\beta}} \sum_i p_i$$

where α and β are indices for the spatial Cartesian coordinates (x, y, z) and i runs over all the particles and photons in the final state. This tensor can be diagonalized according to the standard rules, obtaining three eigenvalues $\lambda_1 > \lambda_2 < \lambda_3$, constrained by the relation $\lambda_1 + \lambda_2 + \lambda_3 = 1$, and three eigenvectors $\vec{v_1}$, $\vec{v_2}$ and $\vec{v_3}$. The direction of $\vec{v_1}$ corresponds to the direction of maximum expansion of the event, and in ideal conditions coincides with the thrust axis, while $\vec{v_2}$ and $\vec{v_3}$ are the second and third expansion directions, and play a role similar to the major and minor axes. It appears clear, at this point, that there is a connection between λ_1, λ_2, λ_3 and T, M_M and M_m. Indeed the same information carried by the thrust variables is present in the eigenvalues of the sphericity tensor: in particular the value of λ_1, or equivalently the sum $\lambda_2 + \lambda_3$, is sensitive to the sphericity of the event, while λ_3 is sensitive to its planarity. Thus, the sphericity S and the aplanarity A of the event are defined as

$$S = \frac{3}{2}(\lambda_2 + \lambda_3),$$

$$A = \frac{3}{2}(\lambda_3).$$

Despite the calculation of the event sphericity is straightforward and do not require any minimization procedure like the calculation of T, the elements of the sphericity tensor are quadratic functions of the final state particle momenta, and consequently they are, in principle, infrared divergent.

The search for a simple observable which has a separation power comparable with S and T, but whose calculation is simple and infrared safe led to the construction of the harmonic moments M_l and the Fox-Wolfram moments H_l. The harmonic moments are defined with respect to an arbitrary reference axis as:

$$M_l = \frac{\sum_i |p_i| \mathcal{P}_l(\cos\theta_i)}{\sqrt{s}},$$

where θ_i is the angle between the i-th particle's momentum and the reference axis and $\mathcal{P}_l$ is the Legendre polynomial of order l. These quantities are linear function of the momenta, and thus infrared safe, and their calculation do not require any minimization process. However, the presence of a physically motivated reference axis is crucial, otherwise an arbitrary choice can easily reduce the separation power between spherical and jet-like events.

Together with these multiple moments M_l, Fox and Wolfram introduced another observable, which was due to become one of the most popular discriminators between spherical and jet-like events: the harmonic moments H_l, now universally known as Fox-Wolfram moments. This set of observables, unlikely all the previous one, are not based on the search of a main symmetry axis of the event, but are based on the study of the cross-correlations among the particles in the final state:

$$H_l = \frac{\sum_{i,j} |p_i||p_j|\mathcal{P}_l(\cos\theta_{i,j})}{E_{tot}^2},$$

where $\theta_{i,j}$ is the opening angle between the i-th and j-th particle's momentum and E_{tot} is the sum of the energies of all the detected particles. Furthermore the H_l functions are infrared safe.
Usually the H_l moments are not directly used to categorize the event shape, but the ratios

$$R_l = \frac{H_l}{H_0}$$

are instead used in order to reduce the dependence on the mass assumption used in the calculation of the energy of the particles.

3.1.4 Statistical methods

Our study is performed according to the Belle internal prescription for the blind analysis. The selection criteria are optimized using the Monte Carlo (MC) simulation only, and then validated using either control samples or sidebands samples obtained from the Data. The fitting procedure, the statistical methods for the evaluation of significances and upper limits, and the PDFs used for modeling both the signals and the background are also determined according to the MC simulation. After the optimization procedure is completed and validated, it is applied to the data sample and it is not changed anymore. The optimization of the selection criteria is done maximizing the figure of merit $F(c) = \frac{S(c)}{\sqrt{S(c)+B(c)}}$, where $S(c)$ and $B(c)$ are, respectively, the signal and background yield as function of the cut value c. This figure of merit is preferred to the alternative $F'(c) = \frac{S(c)}{\sqrt{B(c)}}$ since its value is less depended from the assumption on the signal yield done in the MC simulation. We however notice that our analysis is characterized by a large combinatorial background, thus we expected $S << B$ and the two figures give approximatively the same result.

In order to easily include the systematic uncertainty in the estimation of the upper limits, we will apply the modified frequentist approach known as CL_s method [163, 164], and more specifically its implementation in the TLimit ROOT class [165]. The CL_s ratio is defined as

$$CL_s = \frac{p_{s+b}}{1 - p_b},$$

where p_{s+b} is the p-value of the fit performed using the *signal + background* hypothesis and p_b is the p-value of the *background-only* hypothesis. The signal yields for which $CL_s < 0.1$ can be excluded at 90% CL. Systematic uncertainties on both the signal and background level can be taken into account via additional Toy-MCs. For the estimation of the statistical significances we use the profile likelihood technique, that is suitable for high-statistic signals and computationally significantly faster than the CLs method.

3.2 Montecarlo simulations settings

In this section we will describe the settings used for the MC simulation of both signal and background processes, with a particular focus on the fine-tuning the photon energy resolution.

The blind analysis approach requires large MC samples of both background and signal processes. As main background Montecarlo, we use the official Belle simulated samples of $\Upsilon(4S) \to B^0\bar{B}^0$ ("mixed" sample), $\Upsilon(4S) \to B^+B^-$ ("charged" sample), $e^+e^- \to u\bar{u}, d\bar{d}, s\bar{s}$ ("uds" sample),

$e^+e^- \to c\bar{c}$ ("charm" sample), $\Upsilon(5S) \to B_s\bar{B}_s$ ("BsBs" sample) and $\Upsilon(5S) \to B\bar{B}$ ("non-BsBs" sample). We will refer to this group of MC as the "generic MC". In addition to these, we generate new samples that accounts for the possible peaking backgrounds and control channels, not included in the generic MC. The transitions $\Upsilon(4S) \to \eta\Upsilon(1S)$, $\Upsilon(5S) \to \eta\Upsilon(1S)$ and $\Upsilon(5S) \to \eta\Upsilon(2S)$ have been already observed reconstructing the $\Upsilon(1S,2S) \to \mu^+\mu^-, e^+e^-$ decays, measuring the branching fractions reported in Table 3.3, and will serve as control channels. The signal processes that we will look for are $\Upsilon(5S) \to \eta h_b(1P)$, $\Upsilon(5S) \to \eta h_b(2P)$, $\Upsilon(5S) \to \eta\Upsilon_{1,2}(1D)$, and $\Upsilon(4S) \to \eta h_b(1P)$. In addition to these, the $h_b(1P) \to \gamma\eta_b(1S)$ can be studied too and is included among the signal samples.
Possible peaking backgrounds can arise from not yet observed η transitions among narrow bottomonium states. In particular we include in our simulation $\Upsilon(5S) \to \pi\pi\Upsilon(1D) \to \pi\pi\eta\Upsilon(1S)$ [5], $\Upsilon(4S) \to \gamma\chi_{b0}(2P) \to \gamma\eta\eta_b(1S)$ and $\Upsilon(4S) \to \gamma\gamma\Upsilon(1D) \to \gamma\gamma\eta\Upsilon(1S)$[6]

The physical processes are simulated using the EvtGen software [166], in conjunction with Pythia6 [167] for the simulation of the fragmentation processes and PHOTOS [168] for the inclusion of the radiative corrections. The detector response is simulated using the Geant3 package [169]. In order to account for the evolving beam and detector conditions along the data taking, different MC sample, each one with different detector settings, are generated for each experiment according to the luminosity recorded.

In order to account for the soft ISR effects we use the VECTORISR model implemented in EvtGen, which allows to simulate the $e^+e^- \to \gamma_{ISR}Y(nS)$ process.

---

[5] A hint of the $\Upsilon(5S) \to \pi^+\pi^-\Upsilon(1D)$ is reported by Belle [141], but the branching fraction has not been measured. The exclusive decay chain $\Upsilon(5S) \to \pi^+\pi^-\Upsilon(1D) \to \pi^+\pi^-\gamma\gamma\Upsilon(1S)$ is also known to occur with branching fraction

[6] Since no $\Upsilon(4S) \to \Upsilon(1D)$ transition has been observed, we assume that the $\Upsilon(1D)$ is produced through the reaction $\Upsilon(4S) \to \gamma\chi_{bJ}(2P) \to \gamma\gamma\Upsilon(1D)$, in analogy with what has been observed in the $\Upsilon(3S)$ decays.

3.2.1 Angular distributions

The angular distribution for each process is determined assuming the dominance of the lower angular momentum. For the point of view of the quantum numbers J^{PC}, the process $\Upsilon(nS) \to \eta h_b(mP)$ can be represented as $1^{--} \to 0^{-+}1^{-+}$, thus both $S-$, $P-$ and $D-$ wave contributions are allowed. However, the P-parity conservation forbids $P-$wave components and we assume the transition to be completely dominated by the $S-$wave term.

The process $\Upsilon(nS) \to \eta\Upsilon(mS)$ corresponds to a $1^{--} \to 0^{-+}1^{--}$ transition, thus again $S-$, $P-$ and $D-$ wave contributions are allowed by the angular momentum conservation. In this case the $P-$parity conservation requires the transition to precess though odd wave amplitudes, and we model is as dominated by the $P-$wave only. The same arguments apply to the transitions $\Upsilon(5S) \to \eta\Upsilon_{1,2}(1D)$, while $\Upsilon(5S) \to \eta\Upsilon_3(1D)$ can proceed only via $D-$wave but violating the P-parity, and is thus assumed not to be present. $h_b(nP) \to \gamma\eta_b(mS)$, corresponding to $1^{-+} \to 1^{--}0^{-+}$ is completely described by an electric dipole term E1, corresponding to a pure $P-$wave transition. With this assumption, the radiative photon from the decay chain $\Upsilon(nS) \to \eta h_b(mP) \to \eta\gamma\eta_b(1S)$ is expected to have an angular distribution, in the CM frame, proportional to $1 + \cos^2(\theta)$. Figure 3.10 shows the angular distribution obtained from the CM truth, together with the expected theoretical distribution.

3.2.2 Tuning of the gluon fragmentation parameters

Our current knowledge of the hadronic annihilation modes of bottomonia is very limited. Few $\Upsilon(1S, 2S)$ 2- and 3-body modes, 100 generic hadronic modes and 48 modes with $\Lambda\bar{\Lambda}$ pairs were investigated, but the sum of the measured branching ratios barely accounts for 2% of the total decay width. No information is available on $h_b(nP)$, $\Upsilon(1D)$ and $\eta_b(nS)$

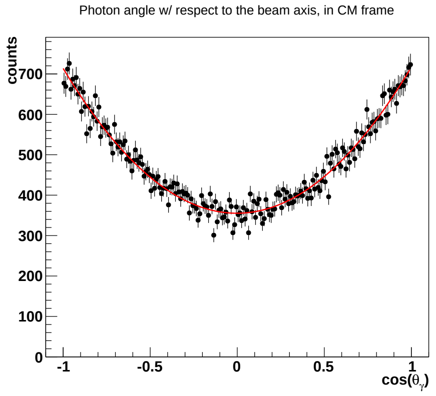

Figure 3.10: Angular distribution of the radiative photon emitted in the decay chain $\Upsilon(4S) \to \eta h_b(1P) \to \eta\gamma\eta_b(1S)$. $\cos(\theta)$ is computed with respect to the beam axis direction in the $\Upsilon(4S)$ reference frame. The red line shows the fit with the function $\mathcal{N}(1+\alpha\cos^2(\theta))$. We find $\alpha = 1.01 \pm 0.02$, in complete agreement with the theoretical expectations.

annihilation. This lack of experimental information is mainly due to the large bottomonium mass, compared to the mass of the hadrons, which allows a large phase space for the annihilation processes. Therefore, the annihilation is likely to produce 10-12 hadrons on average and the full reconstruction of the events is highly insufficient: assuming an 80% geometric acceptance, and 80% efficiency per particle for tracking and PID, an overall 50% efficiency for the background reduction, and a branching ratio of the order of 10^{-5}, on average only 1 event every 10 Millions $e^+e^- \to \Upsilon(1S) \to hadrons$ events with the compete reconstruction of a given annihilation mode is expected.

On the other hand the bottomonium annihilations are well described at the partonic level, as $b\bar{b}$ annihilate into either gluons or quarks. The ratio $\frac{\Upsilon(1S)\to hadrons}{\Upsilon(1S)\to\mu^+\mu^-}$ was indeed already calculated in the very early days of NRQCD, and thanks to the recent experimental measurements the branching ratios of $\Upsilon(1S,2S,3S) \to ggg$, $\Upsilon(1S,2S,3S) \to \gamma gg$ and $\Upsilon(1S,2S,3S) \to q\bar{q}$ are well known. For the other states, we can rely on the Yang-Landau theorem and assume that the hadronization of the spin single states proceeds as $\eta_b \to gg$ and $h_b \to ggg$[7]. The passage from the partonic level to the final state colorless hadron is often describe in terms of an evolving shower, divided in a partonic phase, which takes place early and in a kinematic regime in which α_s allows a perturbative treatment, and a later, partonic phase which takes place when the scale of the system becomes larger, the confining long-distance part of the potential becomes dominant and the quarks are confined into colorless hadrons. So far, no description of this passage from partons to hadrons based rigorously on the QCD Lagrangian is available, thus we have to rely on phenomenological models implemented in Monte Carlo simulations. One of the most popular software packages for describing the hadronization is Pythia6, which implements the so called *string fragmentation* model [170, 171][8].

In order to qualitatively understand this model, let assume to have a $q\bar{q}$ pair emitted back-to-back, as depicted in Figure 3.11. The potential between the two quarks is described as usual by the sum of a Coulombian-like term and a linear term, which grows with the increasing distance

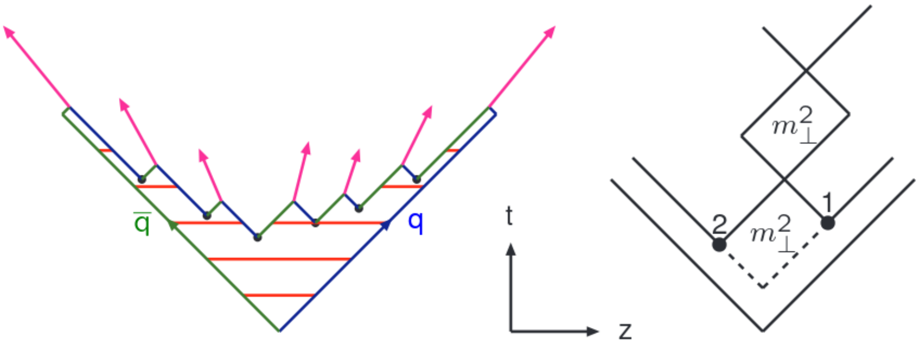

Figure 3.11: Sketch of the string fragmentation picture with two quarks emitted back to back in the CM frame. At each step, a new quark anti-quark pair with transverse mass m_T is produced.

---

[7] Here we treat the gluon as a massless particle with $J^{PC} = 1^{--}$. If virtual gluons with finite mass are involved in the description of the annihilation, as in the case of the $\chi_{b1}(nP)$, the Yang-Landau theorem cannot be applied

[8] For an overview of the fragmentation model, see also [167] and references therein.

between the quarks. This means that the energy stored in the color field among the two quarks increases while the two quarks move away one from the other, eventually to the point at which the creation of an intermediate $q\bar{q}$ pair becomes energetically favored. This situation can be described with the presence of a one-dimensional string among the initial quarks, which is stretched by the motion of $q\bar{q}$. In this picture the creation of a new $q^{'}\bar{q}^{'}$ pair corresponds to the breaking of the original string into two, one connecting q with $\bar{q}^{'}$ and one connecting $q^{'}$ with $\bar{q}$. The process then continues until each $q\bar{q}$ pair as a mass lower than a hadron, at which point only colorless particles are created. An exhaustive description of the aspect to the string fragmentation model can be found in [172]. Without going into details we will try here to point out which are the main parameters that govern the fragmentation.

The probability of creating a $q\bar{q}$ pair with transverse mass m_T during the string breaking is parametrized as:

$$\mathcal{P}(m_T, \kappa) \propto e^{-\frac{\pi m_T^2}{\kappa}} = e^{-\frac{\pi p_T^2}{\kappa}} e^{-\frac{\pi m^2}{\kappa}},$$

where p_t and m are the transverse momentum and the mass of the quark-anti-quark system and $\kappa = 1$ GeV/fm is the string tension. This formula implies a hierarchy in the quark production according to their masses: $u : d : s : c \approx 1 : 1 : 0.3 : 0$, which is strongly dependent on the assumption made for the quark masses. In order to take into account this effect at least for the light quark, the relative probability of creating an $s\bar{s}$ pair is left free and can be tuned on the data.

The model as described so far is able only to produce mesons, but the generation of baryons can implemented by replacing a quark with a diquark system. This description requires a fundamental parameter which governs the probability of having a $(qq)(\bar{qq})$ pair produced instead of a simple $\bar{q}q$ one, and that must be tuned on the data.

In order to completely fragment the original string into hadrons, an iteratively procedure is applied. The simplest is to start from one of the two initial quarks $q\bar{q}$, create an intermediate quark pair $q'\bar{q}'$ and subsequently split the system into a $q\bar{q}'$ meson on one side, and a remaining string connecting q' and $\bar{q}$ which is fragmented again into a meson and a string, until the mass of the residual string is low enough to produce a final meson. In this procedure the transverse momentum of the detached meson is chosen according to the previous formula, while the longitudinal momentum must be chosen in some way though the choice of a proper *fragmentation function* $f(z)$. Since the transverse mass of the meson is already determined and only one degree of freedom is left, the fragmentation functions are usually expressed as function of the adimensional parameter $z = \frac{(E+p_z)_{had}}{(E+p_z)_{string}}$. The choice of the fragmentation function itself is intimately arbitrary, and many possible choices are available in literature. The basic function used by Pythia is the Lund symmetric fragmentation function

$$f(z) \propto z^{-1}(1-z)e^{\alpha}e^{-\beta m_T^2/z},$$

where α and β are parameters to be tuned on the existing data. While β is an universal parameter, two different values of α must be provided, one for the quark and one for the di-quark production.

$f(z)$ is chosen on purpose to be symmetric, so that the fragmentation can be performed starting indifferently by either of the two initial quarks. Nevertheless, if the iteration is carried starting always from one side of the string, the kinematic of the last $q\bar{q}^{'}$ pair is completely constrained by the global energy-momentum conservation, and thus the last hadron cannot be on mass-shell. In order to avoid this problem the hadrons are detached randomly from the two sides of the string at each step, so that the fragmentation proceeds from both the sides towards the center of the string. The process is stopped when the mass of the remaining string falls below a given value, when the remaining part is divided into two hadrons allowing the conservation of energy and momentum using on-shell particles. The threshold at which the hadronization stops is in principle a free parameter, but practically cannot be chosen completely random. The fragmentation is supposed to produce particles with uniform rapidity distribution along all the string, thus if a too high value of the hadronization cutoff is chosen the final two hadrons are likely to be emitted with much larger momentum than the one produced at the early stages. On the other side low cutoff value produce an excessive particle density at mid rapidity. As it is easily understood, the importance of this parameter becomes higher at low energies, when the total energy of the string gets closer to the mass of the final state hadrons. Indeed this parameter, known in Pythia6 as *PARJ(33)*, was found to be the must important in the tuning of the bottomonium annihilations.

The last aspect we which to higligth, is the choice of the light mesons to be produced. In Pythia the constituent quark model is assumed with the standard mixing angles, so that

$$\begin{aligned}
&\eta = \tfrac{1}{2}(u\bar{u} + d\bar{d}) - \tfrac{1}{\sqrt{2}}s\bar{s},\\
&\eta' = \tfrac{1}{2}(u\bar{u} + d\bar{d}) + \tfrac{1}{\sqrt{2}}s\bar{s},\\
&\omega = \tfrac{1}{2}(u\bar{u} + d\bar{d}),\\
&\phi = s\bar{s}.
\end{aligned}$$

However, the $SU(3)$ flavor symmetry breaking implicit in the quark content of η and η' is not encoded in any of the fragmentation steps, thus two *ad-hoc* parameters are implemented to fine tune the production of these two mesons.

This approach to fragmentation has been proven to give results in very good agreement with data at high energies, where α_s is in the perturbative regime, while at the GeV scale a severe fine tuning is needed, and the agreement with the experimental data is much less striking. The default tuning is known to be unable to properly describe the data at B-factories, thus a set of dedicated values has been developed in order to describe the hadron production in B meson annihilation. However, this set of values was found not to properly describe the annihilation of the bottomonium mesons, which takes place at a slightly higher energy scale. Therefore, a further tuning was developed in Belle for the description of $\Upsilon(nS)$ annihilation. This set of parameters are however far from giving a perfect description of the general structure of these processes, and large systematic uncertainties are still present. Table 3.1 presents three different tunings of the gluon fragmentation: the default Pythia6, the tuning adopted by Belle as default, and the modification introduced to better describe the $\Upsilon(nS)$ annihilation.

Table 3.1: Comparison between different Pythia tunings used in Belle.

Parameter	Pythia6 default	Belle Default	Belle quarkonium
PARJ(21)	0.36	0.4	0.4
PARJ(25)	1.0	0.27	0.27
PARJ(26)	0.4	0.12	0.12
PARJ(33)	0.8	0.33	1.0
PARJ(35)	0.8	1.0	1.0
PARJ(41)	0.3	0.32	0.32
PARJ(42)	0.58	0.62	0.62
PARJ(54)	-0.05	-0.05	-0.04
PARJ(55)	-0.005	-0.005	-0.004
PARJ(82)	1.0	1.0	0.1

The misomdelling of the hadronization reflects in a mismodelling of the general event characteristic, such as the charged track multiplicity, the visible energy E_{vis} i.e. the sum of the all the ECL energy clusters, and the event shape observables. This mismodelling impacts the estimation of the trigger efficiency, the hadronic even selection efficiency, and the quality of the event shape simulation. Even with the improved tuning, clear discrepancies are still seen when the MC simulation is compared to the $\Upsilon(1S)$ data, as shonw in Figure 3.12, introducing a few percent-level systematic uncertainty in the measurement of the branching ratios for the processes analyzed in this work.

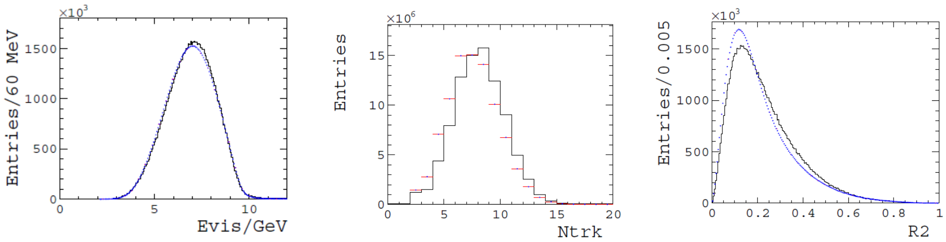

Figure 3.12: Comparison between the MC simulation (dots) and the data (solid histogram) in hadronic events at $\sqrt{s} = 9.460$ GeV. *Left:* Visible energy. *Center:* Charged tracks multiplicity. *Right:* R_2 Fox-Wolfram moment.

This uncertainty is expected to be reduced when the BelleII dataseted will become available. The BelleII experiment will profit from a more precise MC simulation based on Pythia8 with a dedicated set of tunings obtained studying the Belle data. A working group for the production this tuning set has been already set up and is currently working, and is expected to provide its first result by the end of 2017.

3.2.3 Tuning of the photon energy scale

In order to obtain a precise measurement of the $\eta_b(1S)$ mass, a precise modeling of the calorimeter response to photon is required. From previous studies the MC simulation is known to reproduce the photon reconstruction efficiency with a $\pm 2\%$ and the energy resolution within few percent. A bias in the energy reconstruction can also be present, induced by mis-modeling in the material budget in from of the calorimeter. In order to re-calibrate the simulation of the calorimeter response in the MC, we reconstruct few decays of well known particles which involves photons, and we compare the position and the width of the corresponding

peaks as they appear in the Data and in the MC samples. Three calibration channels are selected: $\pi^0 \to \gamma\gamma$, $\eta \to \gamma\gamma$, and $D^{0*} \to D^0\gamma$, each one contributing to the calibration in different energy ranges
The photons are reconstructed with the same criteria applied for the data analysis and described in the next session. The D^0 meson is reconstructed in the two body final state $D^0 \to K^+\pi^-$ combining particle pairs with opposite charge, positively identified as pion or kaon, and coming from the primary interaction vertex.
η and π^0 are reconstructed combining photons with energy equal within 5%. In this way the relation between the photon energy bias an the mass shift is simplified. The invariant mass of a photon pair $\gamma_1\gamma_2$, respectively with energies E_{γ_1} and E_{γ_2}, can be written as:

$$M(\gamma\gamma) = \sqrt{2E_{\gamma_1}E_{\gamma_1}(1-\cos\theta_{\gamma_1\gamma_2})},$$

where $\theta_{\gamma_1\gamma_2}$ is the opening angle of the photon pair. A small δM shift in the $\gamma\gamma$ mass can be therefore related to the photons' energy shifts δE_{γ_1} and δE_{γ_2} by the relation:

$$\delta M = \frac{\sqrt{2E_{\gamma_2}(1-\cos\theta_{\gamma_1\gamma_2})}}{2\sqrt{E_{\gamma_1}}}\delta E_{\gamma_1} + \frac{\sqrt{2E_{\gamma_1}(1-\cos\theta_{\gamma_1\gamma_2})}}{2\sqrt{E_{\gamma_2}}}\delta E_{\gamma_2},$$

where we assumed the error on the opening angle to be negligible. Without further assumption, the deconvolution of the photon energy resolution from this relation, although is possible, requires high statistic in order to consistently populate any bin of $(E_{\gamma_1}, E_{\gamma_2})$. In order to simplify the problem we require $E_{\gamma_1} \approx E_{\gamma_2} = E_\gamma$, so that

$$\delta M = 2\sqrt{(1-\cos\theta_{\gamma_1\gamma_2})}\delta E_\gamma$$

and consequently, defining $\Delta M = M_{MC} - M_{data}$ as the difference between the $\gamma\gamma$ mass measured in the MC and in the Data samples,

$$\frac{\delta E_\gamma}{E_\gamma} = \frac{\Delta M}{M_{MC}}.$$

For the D^{0*} we apply a similar procedure. In order to neglect the contribution due to the mis-modeling of the D^0 peak parameters, we define $\tilde{M}(D^0\gamma) = M(D^0\gamma) - M(D^0) + m_{D^0}$, so that the tracking-related uncertainties are almost completely eliminated. The energy of the photon emitted in the D^{0*} decay can be expressed as

$$E_\gamma = \frac{\tilde{M}^2(D^0\gamma) - M^2(D^0)}{2(E_{D^0} - p_{D^0}\cos\theta_{D^0,\gamma})},$$

therefore, following the same conventions adopted before for the definition of ΔE_γ and $\Delta\tilde{M}(D^0\gamma)$,

$$\frac{\Delta E_\gamma}{E_\gamma} = 2M_{MC}(D^0\gamma)\frac{\Delta\tilde{M}(D^0\gamma)}{M^2_{MC}(D^0\gamma) - M^2_{MC}(D^0)}.$$

From the measurement of the widths and centroid of the calibration processes, and using the formulas presented above, we are finally able to measure two correction factors $\mathcal{F}_{en}$ and $\mathcal{F}_{res}$ to apply, respectively, to the photon energy scale and the photon energy resolution. To measure the energy shifts, we fit the control sample peaks in the MC and in the data as function of the photon energy in the laboratory frame, in 100 MeV wide intervals. Figure 3.13 shows the behavior of the invariant mass of the control channel as function of the photon energy, in the data sample. The $D^{0*} \to D^0\gamma$, $\pi^0 \to \gamma\gamma$ and $\eta \to \gamma\gamma$ peaks are clearly visible.

The fit of the MC sample is performed, in each energy interval, with a PDF obtained by the sum of a double sided, asymmetric Crystal Ball (CB) function, characterized by two power-law tails merged with and asym-

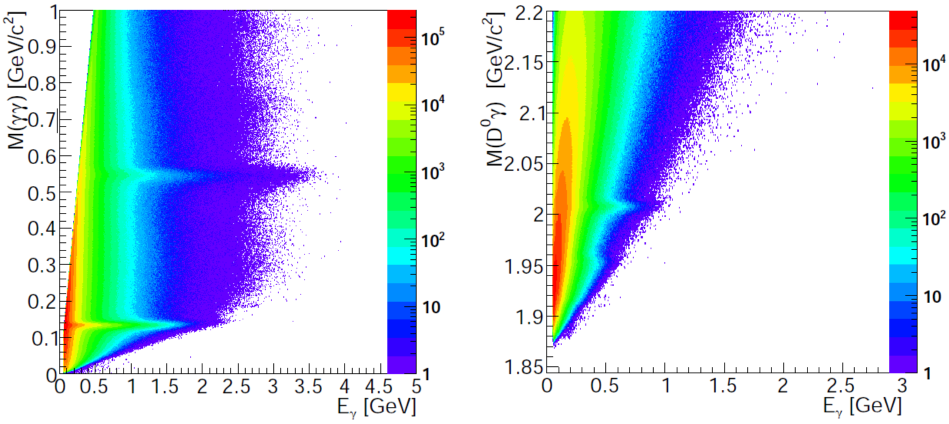

Figure 3.13: *Left:* $M(\gamma\gamma)$ as function of E_γ, in the data sample.
Right: $M(D^0\gamma)$ as function of E_γ .

metric Gaussian core with resolutions σ_L and σ_R, and polynomial PDF that describes the background. The parametrization of the peak PDF is:

$$f_{sig}(x) = N \cdot \begin{cases} B_L^{-n_L} e^{-\frac{\alpha_L^2}{2}} & \text{if } t_L < -\alpha_L \\ e^{-\frac{t_L^2}{2}} & \text{if } -\alpha_L < t_L < 0 \\ e^{-\frac{t_R^2}{2}} & \text{if } 0 < t_R < \alpha_R \\ B_R^{-n_R} e^{-\frac{\alpha_R^2}{2}} & \text{if } t_R > \alpha_R \end{cases}$$

where $t_{L,R} = \frac{(\mu - x)^2}{\sigma_{L,R}}$ is the usual Gaussian function exponent and the factors $B_{L,R} = 1 - \frac{t_{L,R}\alpha_{L,R} - \alpha_{L,R}^2}{n_{L,R}}$ are introduced in order to assure the continuity and the smoothness of f_{sig} in $t_{L,R} = \pm\alpha_{L,R}$. The free parameters of the fit are the four tail-shape factors $\alpha_{L,R}$ and $n_{L,R}$, the width of the core asymmetric Gaussian $\sigma_{L,R}$, the peak position μ and the normalization N. The fit is then repeated on the data sample, convolving the signal PDF, whose parameters are now fixed, with a Gaussian smearing function $S(M) = \frac{e^{-(M-\Delta M)^2}}{\sigma^2}$. ΔM here represents the difference between the peak position in the data and in the MC sample, while σ is an additional resolution term. The background PDF parameters are left floating in order to account for the small differences in the background shapes among the two samples. The result of the fits in each energy interval are shown in Figures **??**-**??**. We observe that not all the sample contribute or can be used in all the kinematic regions. The D^{0*} values are used only between $E_\gamma = 100$ MeV and $E_\gamma = 500$ MeV, since in the other regions the statistical error on width and mass are not competitive with the other channels. In the case of $\pi^0 \to \gamma\gamma$, the spectrum is well populated up to $E_\gamma \approx$ GeV, but above $E_\gamma = 0.6$ GeV the possibility for the two ECL cluster originated by the two photons to overlap becomes not-negligible. To estimate this threshold, we first explicit the opening angle of a photon pair as function of their energy E invariant mass M:

$$\cos\theta = 1 - \frac{M^2}{4E^2}.$$

Since the inner radius of the ECL is $r = 1.34$ m, the distance between the two clusters if the photons are emitted at mid-rapidity is:

$$d \approx \frac{rM}{\sqrt{2}E}.$$

We consider the overlapping effects to be not negligible if the distance among the cluster centers falls below $d_{crit} = 20$ cm, since for smaller distance the $3x3$ clusters containing the showers start to overlap. The corresponding critical energies are $E^{\pi^0}_{\gamma,crit} = 0.64$ GeV for π^0's and $E^{\pi^0}_{\gamma,crit} = 2.6$ GeV for η's. This calculation is approximate since it considers the closest distance between the ECL and the interaction point and do not account for the increasing shower size with increasing photon energy, but clearly indicate that the calibration obtained with π^0 can be used between $E_\gamma = 0$ GeV and $E_\gamma = 0.6$ GeV. The η mode, finally, is used for $E_\gamma > 0.2$ GeV since for lower energies the signal peak is statistically not enough significant The results obtained with the different control channels are shown in

Figure 3.14. We calculate, for each sample, the correction factors $\mathcal{F}_{en}$ and $\mathcal{F}_{res}$ as

$$\mathcal{F}_{res} = \frac{\sigma^{data}}{\sigma^{MC}}$$

and

$$\mathcal{F}_{en} = 1 + \Delta M / M^{MC}.$$

In order to account for the presence of asymmetric peaks and the additional smearing term in the fit of the data sample, we define σ^{data} and σ^{MC} as $\sigma^{data,MC} = \frac{\sigma_L^{data,MC}+\sigma_R^{data,MC}}{2}$, where $\sigma_{L,R}^{data} = \sqrt{{\sigma_{L,R}^{MC}}^2 + \sigma^2}$. In order to estimate the final energy correction, the average of the results obtained in each bin from the different control channels is calculated. The additional energy smearing determined by the value of $\mathcal{F}_{res}$ is thus applied photon-by-photon on the MC sample used for the estimation of the reconstruction efficiency and the resolutions. Given an MC photon with original 3-momentum $\vec{E}_0$ and reconstructed momentum components $\vec{E}_r$,

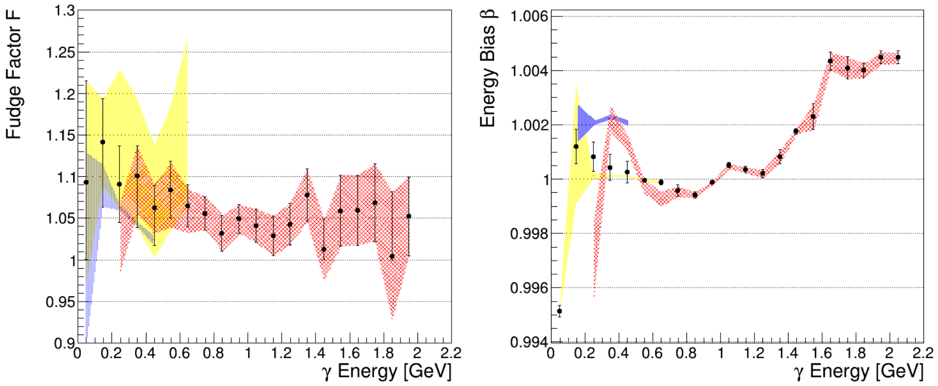

Figure 3.14: Fudge factors $\mathcal{F}_{res}$ (*left*) and $\mathcal{F}_{en}$ (*right*) from different calibration samples: $D^{0*} \to D^0\gamma$ (blue), $\eta \to \gamma\gamma$ (red) and $\pi^0 \to \gamma\gamma$ (yellow). Each band represents the $\pm 1\sigma$ region around the central value, accounting for the systematic uncertainty induced by the choice of the background PDF. The black points represent the average value used for smearing the MC samples.

we calculate the smeared reconstructed momentum as

$$\vec{E}_s = (\vec{E}_0 + (\vec{E}_r - \vec{E}_0) \cdot \mathcal{F}_{res}) \cdot \mathcal{F}_{en}.$$

The original resolution $\Delta\vec{E} = \vec{E}_r - \vec{E}_0$ is increased by a factor $\mathcal{F}_{res}$, while the global energy of the photon is scaled by a factor $\mathcal{F}_{en}$.

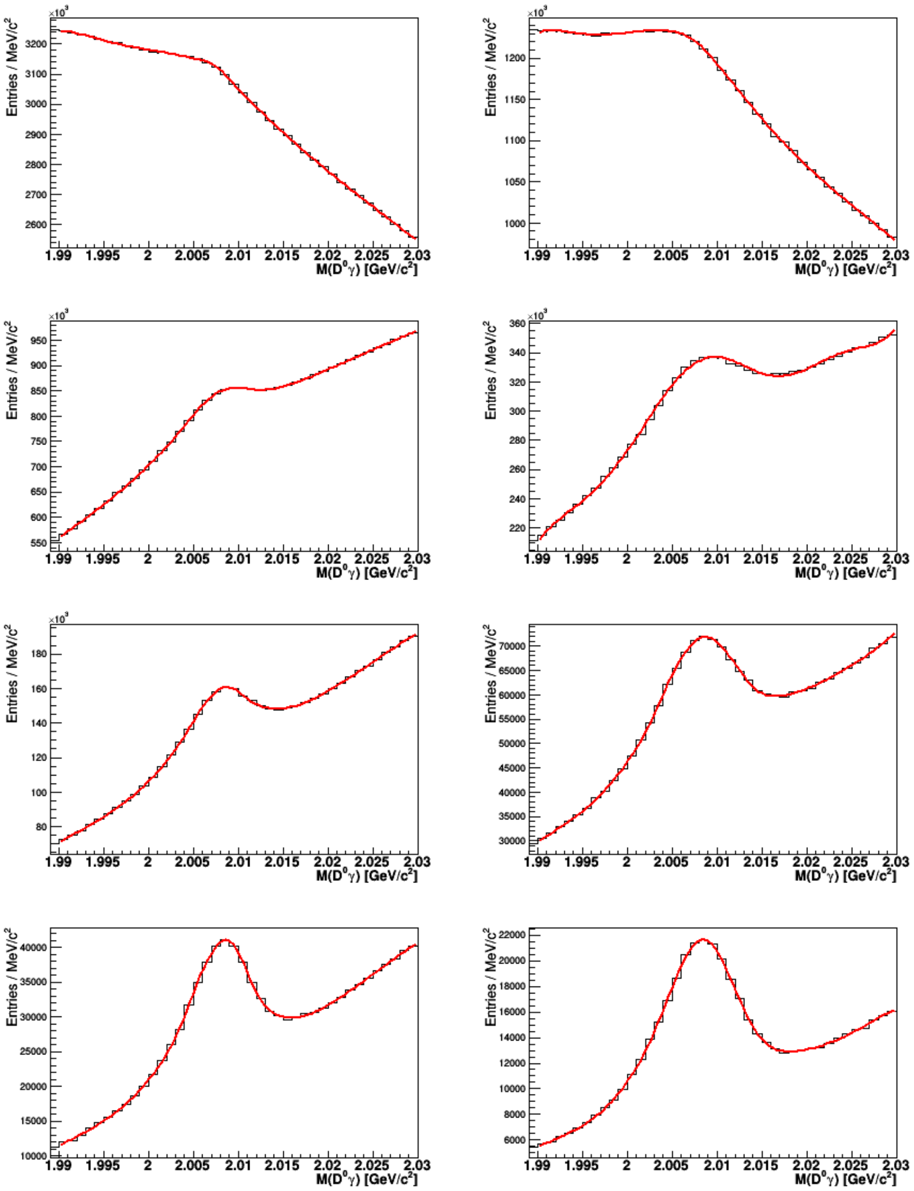

Figure 3.15: Fit of $M(D^0\gamma)$ in the D^{0*} regions from ($100 < E_\gamma < 200$) MeV (upper row) to ($400 < E_\gamma < 500$) MeV (bottom row). The left plot shows the MC sample and the right plot shows the Data sample.

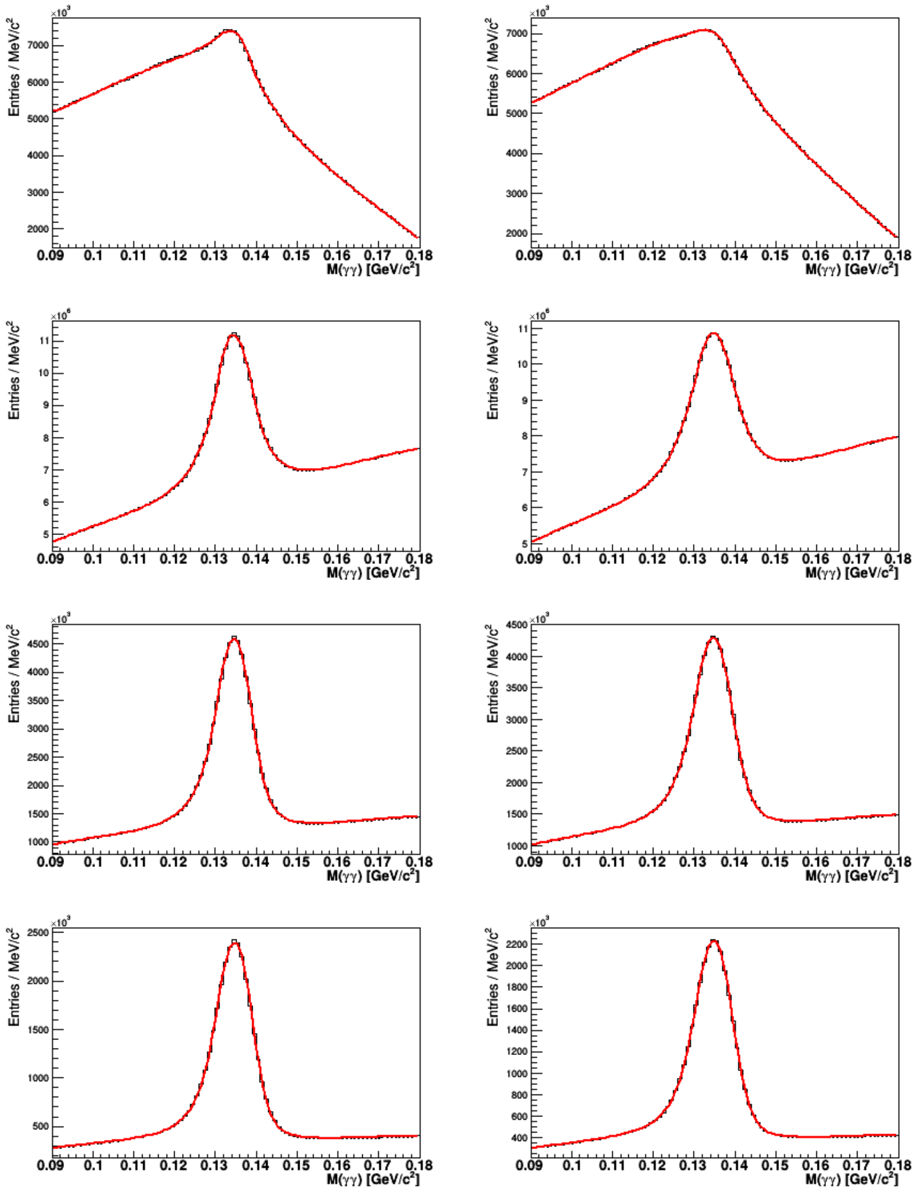

Figure 3.16: Fit of $M(\gamma\gamma)$ in the π^0 region from $(0 < E_\gamma < 100)$ MeV (upper row) to $(300 < E_\gamma < 400)$ MeV (bottom row). The left plot shows the MC sample and the right plot shows the Data sample.

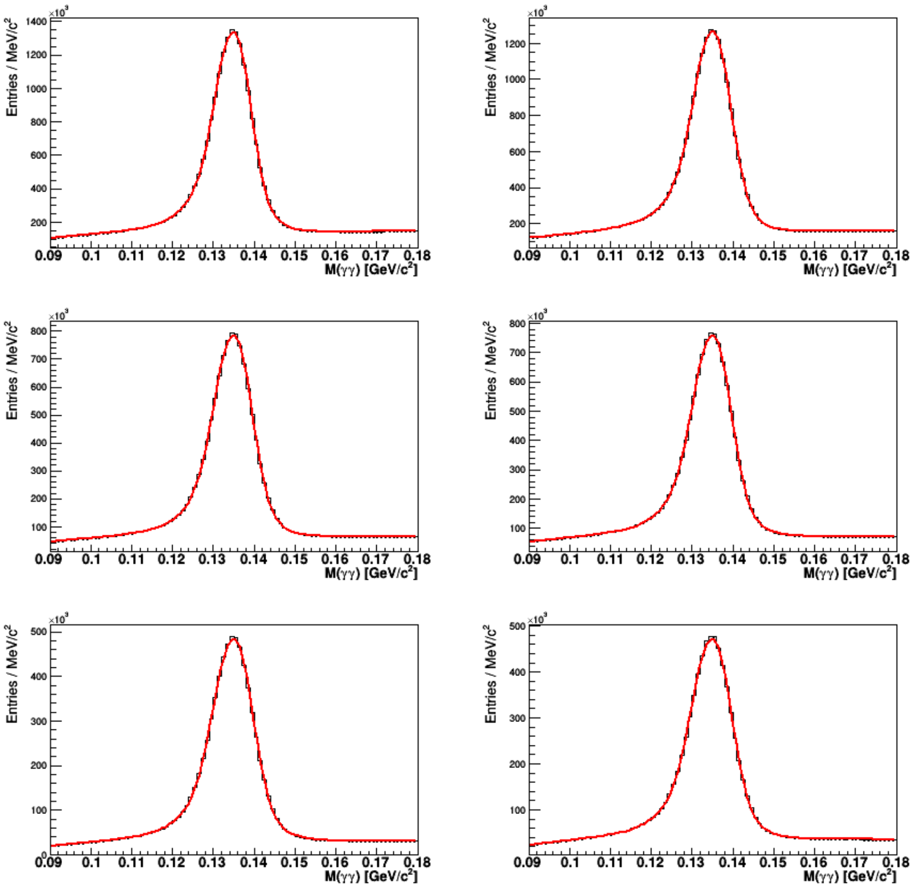

Figure 3.17: Fit of $M(\gamma\gamma)$ in the π^0 region from $(400 < E_\gamma < 500)$ MeV (upper row) to $(600 < E_\gamma < 700)$ MeV (bottom row). The left plot shows the MC sample and the right plot shows the Data sample.

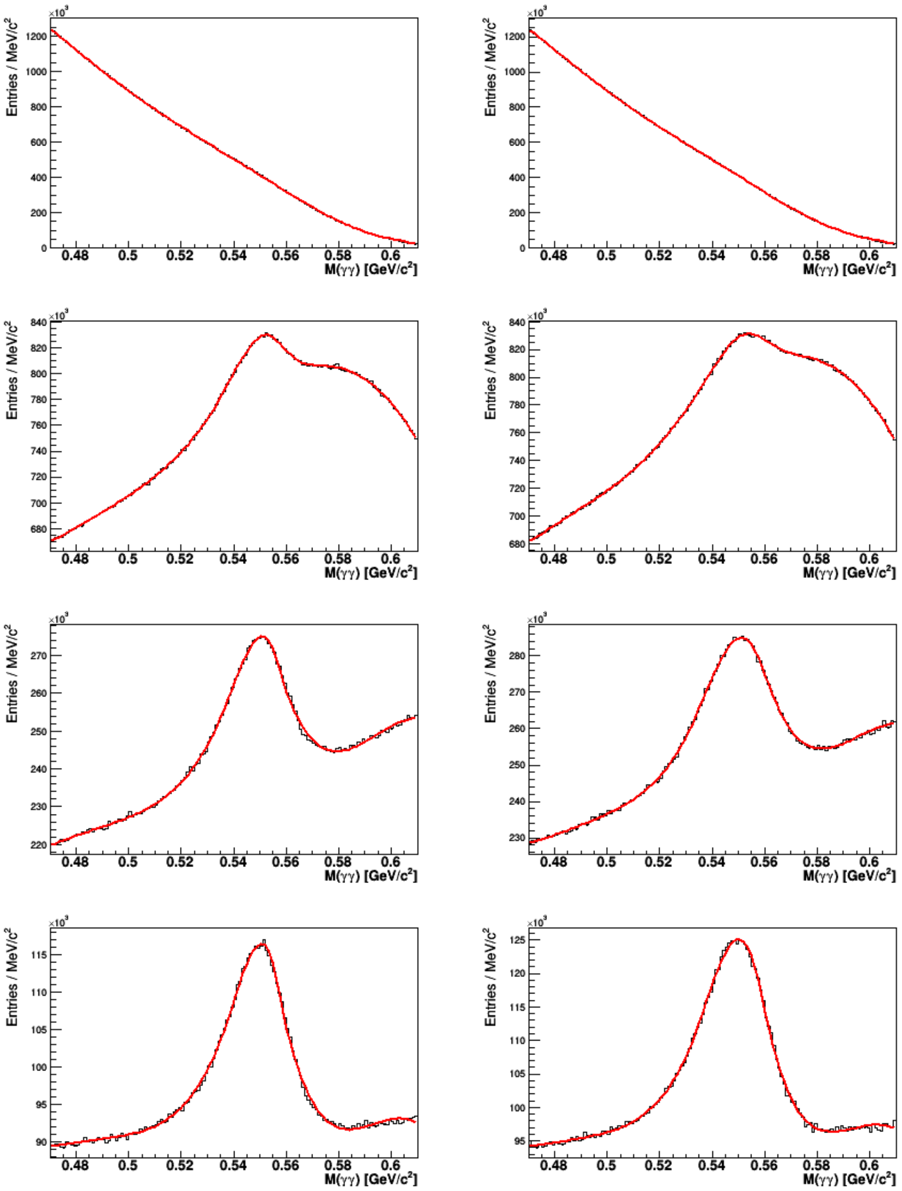

Figure 3.18: Fit of $M(\gamma\gamma)$ in the η region from $(200 < E_\gamma < 300)$ MeV (upper row) to $(500 < E_\gamma < 600)$ MeV (bottom row). The left plot shows the MC sample and the right plot shows the Data sample.

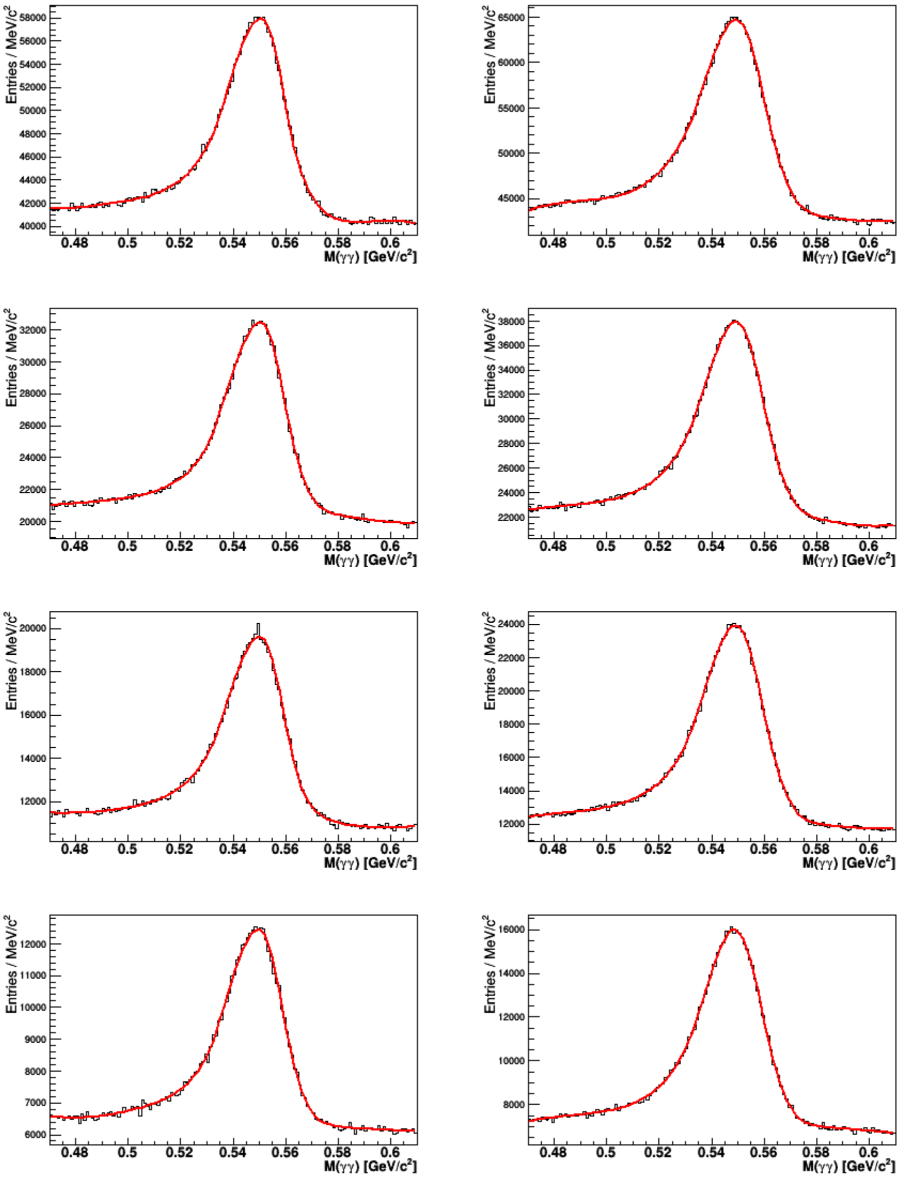

Figure 3.19: Fit of $M(\gamma\gamma)$ in the η region from $(600 < E_\gamma < 700)$ MeV (upper row) to $(900 < E_\gamma < 1000)$ MeV (bottom row). The left plot shows the MC sample and the right plot shows the Data sample.

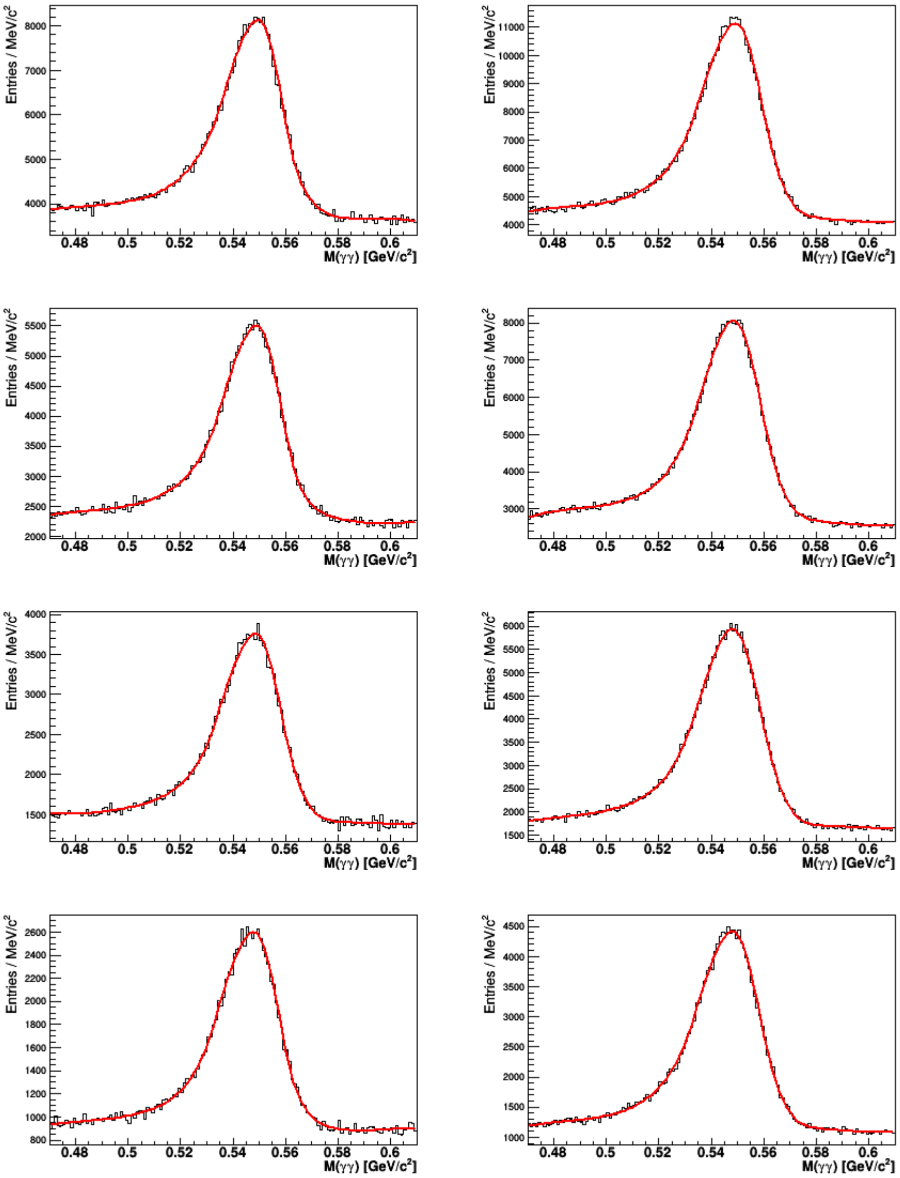

Figure 3.20: Fit of $M(\gamma\gamma)$ in the η region from $(1000 < E_\gamma < 1100)$ MeV (upper row) to $(1300 < E_\gamma < 1400)$ MeV (bottom row). The left plot shows the MC sample and the right plot shows the Data sample.

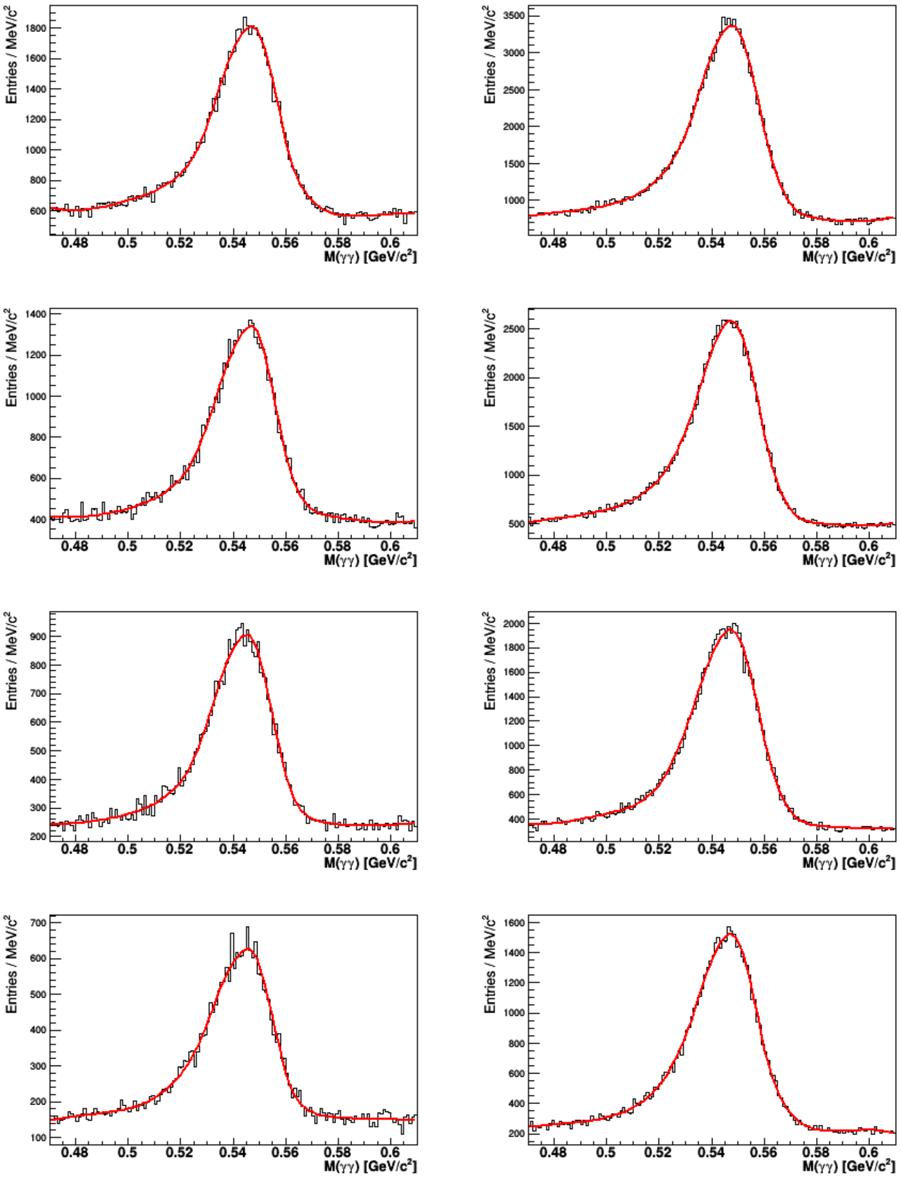

Figure 3.21: Fit of $M(\gamma\gamma)$ in the η region from $(1400 < E_\gamma < 1500)$ MeV (upper row) to $(1700 < E_\gamma < 1800)$ MeV (bottom row). The left plot shows the MC sample and the right plot shows the Data sample.

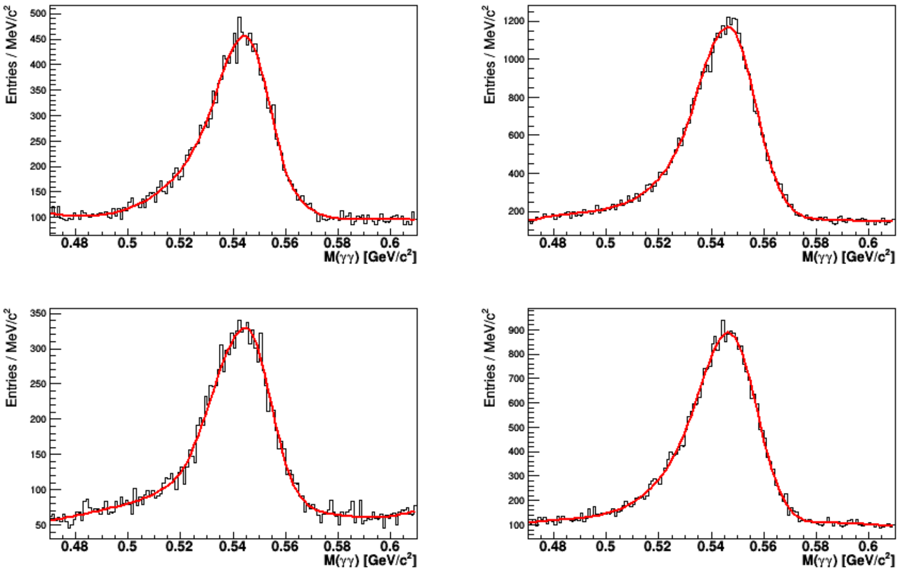

Figure 3.22: Fit of $M(\gamma\gamma)$ in the η region from ($1800 < E_\gamma < 1900$) MeV (upper row) to ($1900 < E_\gamma < 2000$) MeV (bottom row). The left plot shows the MC sample and the right plot shows the Data sample.

3.2.4 Montecarlo samples

Table 3.2 summarizes the EvtGen decay models used for the genration of the signal processes. *PHSP* describes a phase-space flat distribution. *PARTWAVE* allows to include the correct angular distributions on top of the phas-space one, and takes 6 agruments: the even ones are the relative wight of the possible angular waves in increasing order (S,L,P,D,F...), while the odd ones are complexes phases that allows to include CP-violation effects. *HELAMP* also allows to model the angular distribution, but takes as agrument the helicity amplitudes instead of the partial vawe ones.

Table 3.2: Size and characteristics of the signal MC samples.

Channel	Decay model
$\Upsilon(5S) \to \eta h_b(1P)$	PARTWAVE 1. 0. 0. 0. 0. 0.
$\Upsilon(5S) \to \eta h_b(2P)$	PARTWAVE 1. 0. 0. 0. 0. 0.
$\Upsilon(5S) \to \eta\Upsilon(1S)$	HELAMP 1 0 0 0 0 -1
$\Upsilon(5S) \to \eta\Upsilon(2S)$	HELAMP 1 0 0 0 0 -1
$\Upsilon(5S) \to \eta\Upsilon(1^3D_{1,2})$	PARTWAVE 0. 0. 1. 0. 0. 0.
$\Upsilon(5S) \to \pi^+\pi^-\Upsilon(1D) \to \pi^+\pi^-\eta\Upsilon(1S)$	PHSP
$\Upsilon(4S) \to \eta h_b(1P)$	PARTWAVE 1. 0. 0. 0. 0. 0.
$\Upsilon(4S) \to \eta\Upsilon(1S)$	HELAMP 1 0 0 0 0 -1
$\Upsilon(4S) \to \gamma\chi_{b0}(2P) \to \gamma\eta\Upsilon(1S)$	PHSP
$\Upsilon(4S) \to \gamma\gamma\Upsilon(1D) \to \gamma\gamma\eta\Upsilon(1S)$	PHSP
$h_b(nP) \to \gamma\eta_b(mS)$	HELAMP 1 0 1 0

The radiative transitions among $\chi_{b0,1,2}(nP)$ and $\Upsilon_{1,2,3}(mD)$ exhibit a complex pattern, as shown in Figure 3.23. Given the unknown proportions between the different possible decay chains, and the impossibility to distinguish the $\Upsilon(1D)$ fine splitting due to the insufficient detector resolution, we simply assume a phase-space flat distribution for all these radiative transitions.

A complete stream of generic MC (*uds, charm, BsBs, non-BsBs, mixed, charged*) is used for the background estimation and the optimization of the selection criteria. In generating the MC samples and in the analysis of the

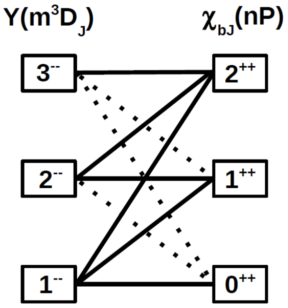

Figure 3.23: Schematic view of the radiative transitions among $\chi_{b0,1,2}(nP)$ and $\Upsilon_{1,2,3}(1D)$. Transitions for which S-wave amplitude is allowed are reported in solid black, while the dashed transitions can occur only via $D-$wave amplitude and are expected to by largely suppressed.

results we assume the branching ratios reported in Table 3.3. The $\Upsilon(2S)$ decays are simulated including the hadronic and radiative transitions to lower bottomonium states. The annihilation into gluons of each state is simulated according to their quantum numbers: $\Upsilon(nS) \to ggg$, $h_b \to ggg$,

Table 3.3: Branching ratios for the transitions included in the MC samples. The transitions $\Upsilon(2S) \to \Upsilon(1S)$ are described according to the latest PDG values and are not reported in this table.

Channel	Assumed Branching ratio $\mathcal{B}_{MC}$	Decay Model
$\eta \to \gamma\gamma$	$(3.941 \pm 0.020) \times 10^{-1}$	PDG2012
$\eta \to \pi^+\pi^-\pi^0$	$(2.292 \pm 0.028) \times 10^{-1}$	PDG2012
$\Upsilon(5S) \to \eta\Upsilon(1S)$	$(7.3 \pm 1.6) \times 10^{-4}$	Belle preliminary [129]
$\Upsilon(5S) \to \eta\Upsilon(2S)$	$(38.1 \pm 4.2) \times 10^{-4}$	Belle preliminary [129]
$\Upsilon(4S) \to \eta\Upsilon(1S)$	$(1.96 \pm 0.28) \times 10^{-4}$	PDG2012
$h_b(1P) \to \gamma\eta_b(1S)$	$0.49^{+0.08}_{-0.07}$	PDG2012
$h_b(2P) \to \gamma\eta_b(1S)$	0.22 ± 0.05	PDG2012
$h_b(2P) \to \gamma\eta_b(2S)$	0.48 ± 0.13	PDG2012
$h_b(1P) \to ggg$	50.8%	$1 - \mathcal{B}[h_b(1P) \to \gamma\eta_b(1S)]$
$h_b(2P) \to ggg$	30.2%	$1 - \mathcal{B}[h_b(2P) \to \gamma\eta_b(1,2S)]$
$\eta_b(1S) \to gg$	100%	
$\eta_b(2S) \to gg$	100%	
$\Upsilon(1S) \to ggg$	81.7%	PDG2012
$\Upsilon(1S) \to \gamma gg$	2.2%	PDG2012
$\Upsilon(2S) \to ggg$	58.8%	PDG2012
$\Upsilon(2S) \to \gamma gg$	8.8%	PDG2012

$\eta_b \to gg$.

3.3 Selection criteria

3.3.1 Hadronic event skim

The Belle datas are divided in different subsamples, called *skims*, each one corresponding to a set of loose selection criteria intened to discriminate between events with different nature: hadronic events, $e^+e^- \to \tau^+\tau^-$, $e^+e^- \to e^+e^- + X$ etcetera... In this analysis we will use the hadronic skim, called *HadronBJ*. To pass this selection the events are requested to have at least three charged tracks pointing towards the primary interaction vertex, a visible energy greater than $0.2\sqrt{s}$, a total energy deposition in the electromagnetic calorimeter (ECL) between $0.1\sqrt{s}$ and $0.8\sqrt{s}$, and a total momentum balanced along the z axis. The skim efficiency is expected to be $> 99\%$ for events with bottomonium states annihilating into gluons or B mason pair decays.

3.3.2 γ reconstruction

The primary goal of the selection criteria is to provide a high-purity sample of photons to reduce the combinatorial background in the η mass region. In order to avoid the introduction of non-smooth structures in the η recoil spectrum, we optimize the selection criteria using all the η in the generic MC samples rather than focusing on the signal η, which are produced in a rather narrow momentum window. Before any selection criteria is applied, the ECL cluster energy spectra in generic $\Upsilon(4S)$ annihilation is peaked at very low energies, where it's dominated by the backgrounds as shown in Figure 3.24. Energy released by hadrons interacting with the ECL crystals is also a sizable source of background that must be reduced.

A set of standard, loose photon quality requirements is already pro-

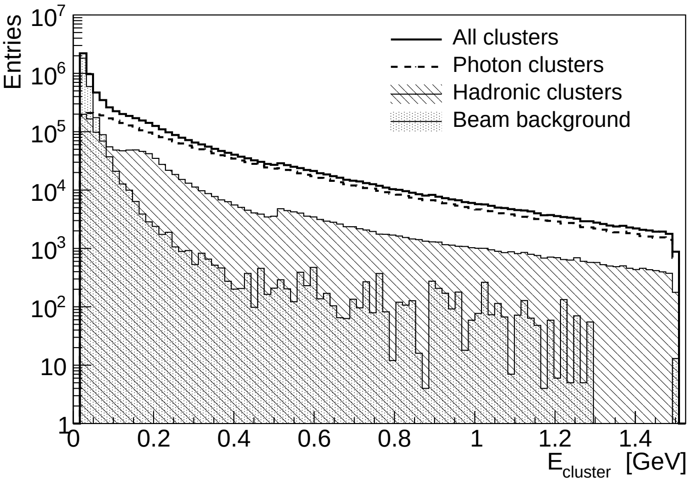

Figure 3.24: Spectrum of the ECL clusters before any selection, from a generic $\Upsilon(4S)$ MC sample

vided by the ECL sub-group, and is shared by different Belle analyses. The main purpose of this selection is to reject the clusters originated by the interaction of hadrons in the calorimeter volume. In orders to eliminate the energy deposits due to protons, pions, electrons or other charged hadrons reconstructed by the tracking system, we require a calorimeter cluster not to match the extrapolated trajectory of any charged track. Then we require the shower radius to be smaller than 5.8 cm and that at least 90% of the cluster energy is released in a 3x3 crystal cluster. These requirements suppress the background due to anti-neutron interaction within the calorimeter volume. Figure 3.25 show the distribution of these two observables for clusters originated by photons and cluster ascribable to hadronic interactions.

The second source of clusters not associated to the hadronic event is represented by the soft photons emitted by the interaction within the beams (the *beam background*) and by the electronic noise. These two sources are not distinguishable in the MC simulations, and must thus be treated

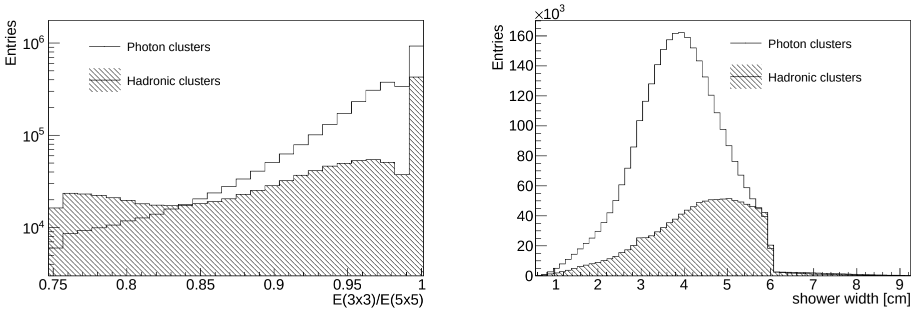

Figure 3.25: *Left:* Ratio between the energy deposited in a 3x3 crystal array and the energy deposited in a 9x9 array, for clusters originated by different sources. *Right:* Shower radius for clusters originated by different sources.

simultaneously. Fake clusters ascribable to readout issues are likely to be constituted by one single crystal, thus we require a good shower to be reconstructed in at least 2 adjacent ECL channels. The distribution of the number of hits associated to each cluster (Figure 3.26) is clearly dominated by the beam backgrounds in the region $N_{hits} < 5$, therefore it could be reasonable to implement a much tighter cut. However, we notice that

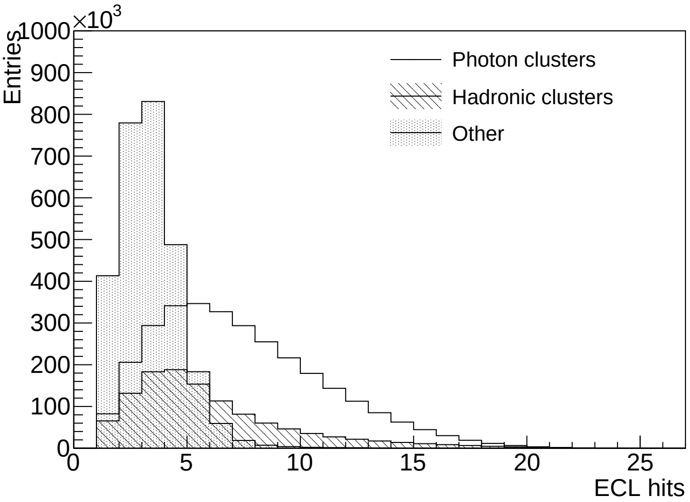

Figure 3.26: Number of ECL hits associated to each cluster in the MC simulation, for different sources.

for real photons associated to an η decay there is a proportionality between the energy and the number of hits in the cluster, while it is absent for the background clusters, which are all characterized by a rather low energy regardless from the cluster size, as shown in Figure 3.27. Therefore we prefer to reject low energy clusters rather than implement further selection on the cluster properties. The standard Belle selection, used in many other analyses, requires to reject clusters with energy below 50 MeV. However, we notice that the soft photons emitted by the beam activity are produce an angular distribution strongly peaked in the forward and backward direction as shown in Figure 3.28. As expected by the presence of

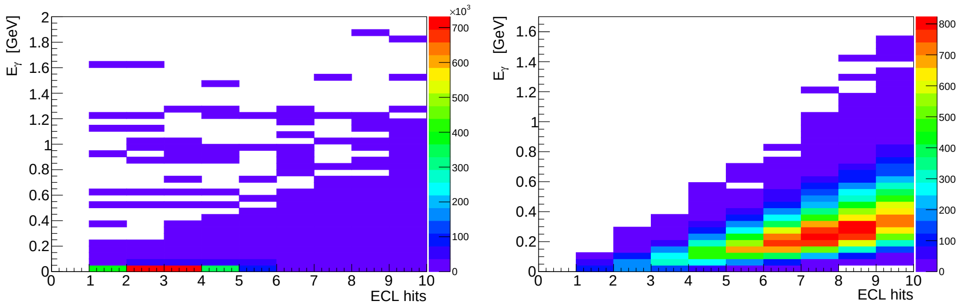

Figure 3.27: *Left*: distribution of the cluster energy as function of the number of ECL hits involved, when the cluster is originated by beam background, electronic noise or reconstruction artifacts. *Right*: same distribution of clusters originated by photons resulting from an η decay.

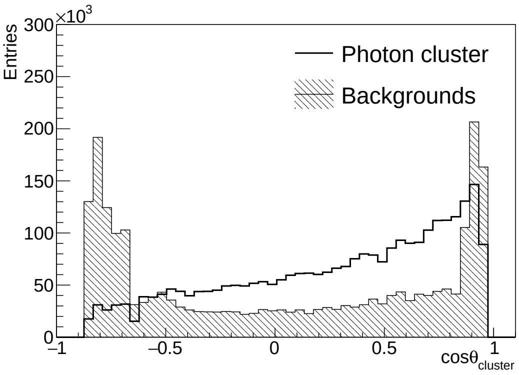

Figure 3.28: Polar angle distribution of the ECL clusters, in the MC simulation.

asymmetric beams, also the energy distribution of the clusters shows a dependence on the polar angle, as shown in Figure 3.29. Therefore, instead

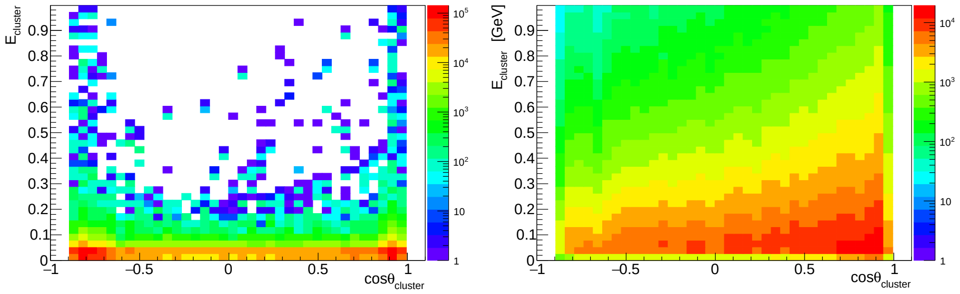

Figure 3.29: *Left*: distribution of the cluster energy as function of the polar angle in the laboratory frame, when the cluster is originated by beam background, electronic noise or reconstruction artifacts. *Right*: same distribution of clusters originated by real photons.

of using the standard Belle selection we choose different energy thresholds in four different ECL section: the two end-caps, the forward half of the barrel, and the backward half of the barrel. Figure 3.30 shows the cluster energy spectra in the four different regions. The energy thresholds are summarized in Table 3.4

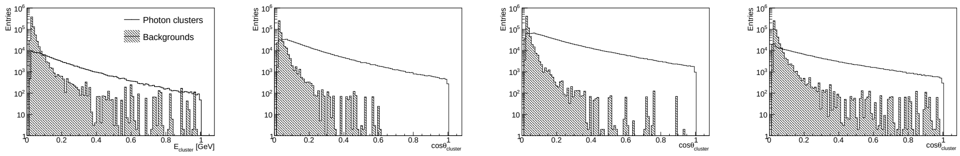

Figure 3.30: Cluster energy distribution in different regions: backward endcap (*left*), backward barrel (*middle, left*), forward barrel (*middle, right*) and forward endcap (*right*).

Table 3.4: Energy threshold in the laboratory frame applied in the selection of the photon candidates.

Angular region (Lab. frame)	Energy threshold [MeV]	Note
$\cos\theta_{lab} < -0.65$	75	ECL Backward Endcap
$-0.65 < \cos\theta_{lab} < 0$	50	ECL Backward Barrel
$0 < \cos\theta_{lab} < 0.85$	60	ECL Forward Barrel
$\cos\theta_{lab} > 0.85$	95	ECL Forward Endcap

The different components of the cluster energy spectrum after all the selection criteria are applied is shown in Figure 3.31 The spectrum of the $\gamma\gamma$ invariant mass results particularly depleted in the low mass region, where the contribution due to the backgrounds is dominant (Figure 3.32). Even if the π^0 and η peaks are clearly visible, further selection criteria will be implemented and described in the next section.

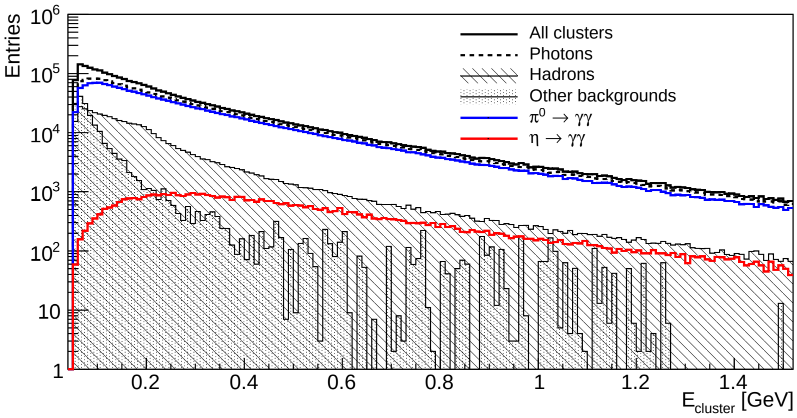

Figure 3.31: Components of the ECL energy spectrum after all the selection criteria are applied.

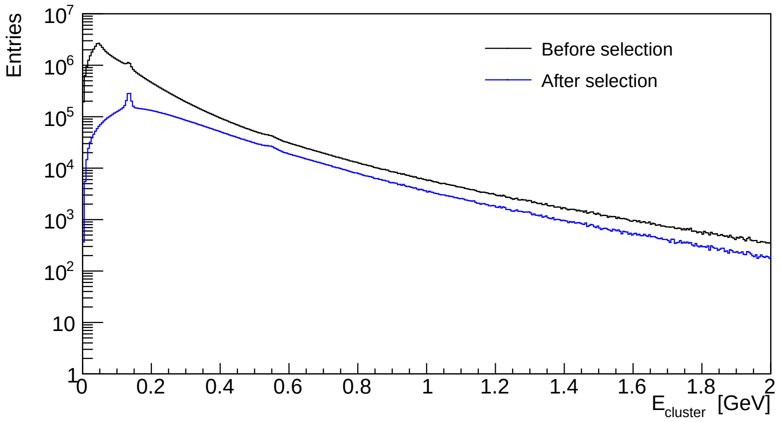

Figure 3.32: Invariant mass distribution of the photon candidates pairs before and after the selection criteria.

3.3.3 $\pi^0 \to \gamma\gamma$ and $\eta \to \gamma\gamma$ selection

In order to further study the selection criteria per η and π^0, we define two *signal windows*: The candidates η are required to have mass within 26 MeV/c^2 of the nominal η mass m_η [**?**], while the candidates in the regions 39 MeV/c^2 $< |M(\gamma\gamma) - m_\eta| <$ 52 MeV/c^2 are used as control samples. For the π^0 candidates we require a mass within 17 MeV/c^2 from the nominal π^0 mass. In both cases the mass window correspond to a $\pm 2\sigma$ region around the central peak. When we will refer to η or π^0 in the following, this mass condition well be understood. The effect of the photon selection on the spectra of reconstructed $\eta \to \gamma\gamma$ and $\pi^0 \to \gamma\gamma$ is shown in Figure 3.33 The selection efficiency on real $\pi^0 \to \gamma\gamma$ and $\eta \to \gamma$ and on the combinatorial background in the same mass regions is shown in Figure 3.34. While in the π^0 case the background reduction is already at a satisfactory level and no further requirement will be applied, the photon quality selection has little impact on the background under the η peak. The main reason for that must be searched in the kinematic of the η decay. The clusters originating from η decays have larger energy than the ones from π^0

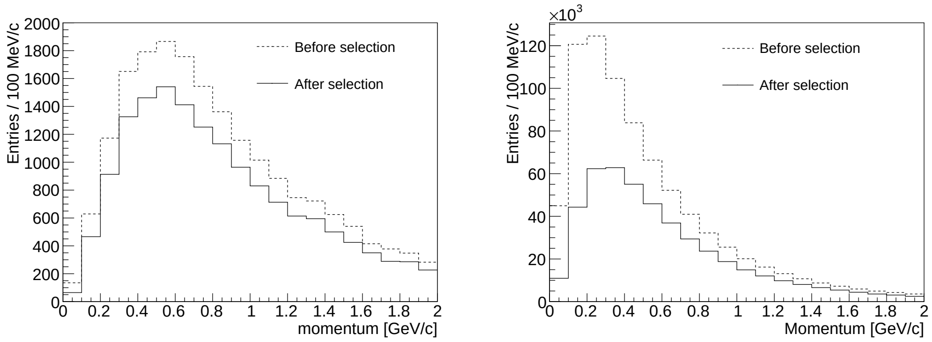

Figure 3.33: *Left*: Spectrum of the reconstructed $\eta \to \gamma\gamma$ before and after the photon selection. *Right*: same distributions for $\pi^0 \to \gamma\gamma$.

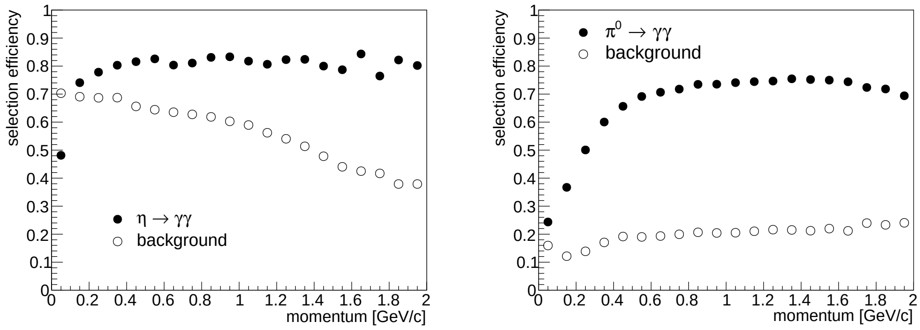

Figure 3.34: *Left*: Spectrum of the reconstructed $\eta \to \gamma\gamma$ before and after the photon selection. *Right*: same distributions for $\pi^0 \to \gamma\gamma$.

decays, therefore are naturally located in an energy range where the backgrounds due to artifacts and hadronic interactions are lower. Furthermore, clusters with energy lower than 80 MeV do not contribute to the combinatorial background in the η mass region, therefore the energy threshold cut has no impact at all. The scalar nature of the η allows, however, to reduce the combinatorial background studying the angular distribution of the photons from the annihilation. We define the helicity angle as the angle between the direction along which the photons are emitted in the η rest frame and the direction of the η momentum in the laboratory frame. This distribution is flat for η, while it exhibits a peak at $\cos\theta_{hel} \approx 1$ for the combinatorial background. The peak is an effect of the boost between the $\gamma\gamma$ center of mass and the lab frame. While for the η case the $\gamma\gamma$ momentum is determined before the annihilation, for the combinatorial background the $\gamma\gamma$ momentum direction is determined by the direction of the highest energy photon. This is clearly visible in figure 3.35, where the helicity angle distribution for η and combinatorial photons is shown. According to the optimization, we require $\cos\theta_{hel} < 0.94$. This criterion is

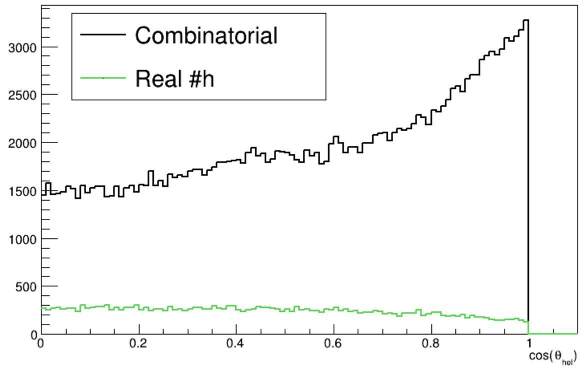

Figure 3.35: Distribution of $\cos\theta_{hel}$ for real η and combinatorial $\gamma\gamma$ pairs in the η mass window.

usually applied also to $\pi^0 \to \gamma\gamma$. However in our case we notice that such cut would simply mimic the effects of the photon energy threshold, since the helicity angle and the energy of the lower energy photon, at a fixed $\gamma\gamma$ mass and momentum, is uniquely determined as shown in figure 3.36. Therefore, no helicity-based selection is applied to $\pi^0 \to \gamma\gamma$. We notice that the position of the cutoff of the helicity angle distribution depends on the momentum of the $\gamma\gamma$ pair as shown in Figure 3.37. Therefore a momentum depended selection is expected to be more efficient rather than the approach we follow. We test this idea optimizing the asymmetry cut in five bins of momentum , but we immediately observe that such approach produces either discontinuities or sharp structures in the η recoil

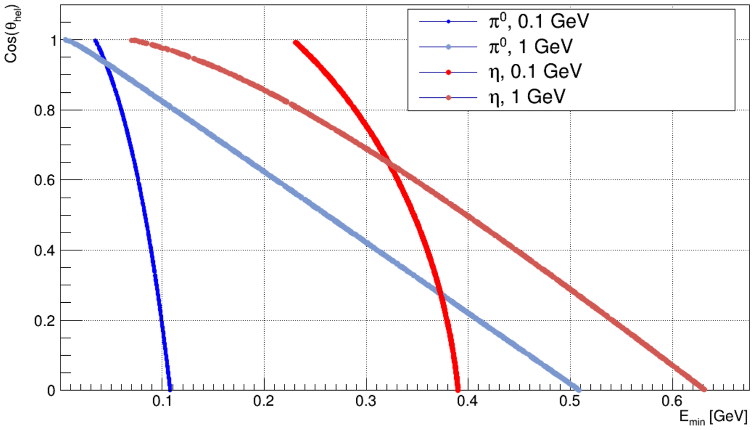

Figure 3.36: Energy of the less energetic photons emitted in an η or π^0 decay as function of $\cos\theta_{hel}$, for different values of the $\gamma\gamma$ pair momentum.

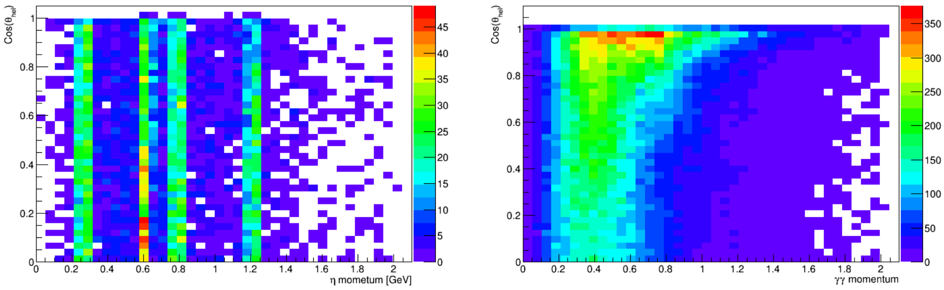

Figure 3.37: *Left*: Spectrum of the reconstructed $\eta \to \gamma\gamma$ before and after the photon selection. *Right*: same distributions for $\pi^0 \to \gamma\gamma$.

mass distribution, making the final fit much more complex. Furthermore, an additional systematic uncertainty is introduced by the binning used for the optimization, and overall the increase in the signal significance is not competitive with the instabilities introduced in the final fit. Therefore, we chose to use a single threshold regardless for the $\gamma\gamma$ momentum.

Despite this further cut increases the signal/background ratio, its impact on the background reduction is still marginal. In order to significantly reduce the combinatorial background, we analyze the origin of the photons that contribute to the $\gamma\gamma$ invariant mass spectrum in the region between 0.5 and 0.6 GeV, shown in Figure 3.38. Roughly one third of the η candidates is actually the result of the combinations of two photons coming from the annihilation of two different π^0's, and overall more than one half of the background is due the result of the combination of a photon originated by a π^0 and another cluster. A significant reduction of the background yield can be thus archived if an efficient π^0 veto is implemented. For our analysis we use a rather simple algorithm based on the completely reconstructed π^0. First we reconstruct the π^0 candidates from the $\gamma\gamma$ pairs with invariant mass within 17 MeV from the nominal π^0 mass. Then we assign to each of them a value $\mathcal{D}$ which is an estimator of the probability, for that candidate, to be a real π^0 rather than combinatorial background. Finally we iteratively remove the photons associated to a π^0 from the η reconstruction stream, starting from the π^0 which has higher probability of being a real π^0. If, during the procedure, a π^0 is found to be made with an photon that has been already vetoed, the other photon is not vetoed. The

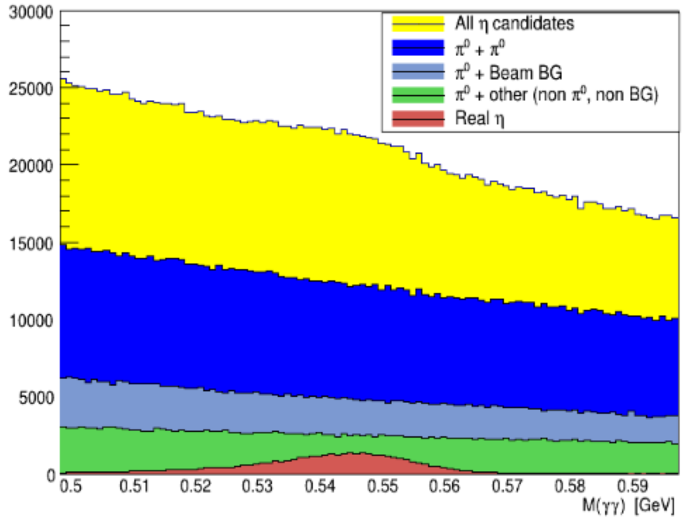

Figure 3.38: Different contributions to the $\gamma\gamma$ invariant mass in the η mass region.

core of the method is clearly the construction of the estimator $\mathcal{D}$. For out analysis we used a quite simple approach based on one single observable which turned out to be the most powerful and widely used one: the difference between the $\gamma\gamma$ mass and the nominal π^0 mass, $\mathcal{D} = |M(\gamma\gamma) - m_{\pi^0}|$. Therefore we arrange the π^0 candidates in increasing distance from the nominal π^0 mass and, starting from the closest one, we exclude the corespondent photons.

This simple approach has already a major impact on the quality of the η reconstruction as shown in Figure 3.39 where the $\gamma\gamma$ invariant mass distribution in the η mass region obtained in the $\Upsilon(5S)$ data sample is shown, with and without the π^0 veto. Thanks to the π^0 veto the signal-over-background ratio (S/B ratio) in the region within $\pm 2\sigma$ from the η peak is increased by a factor 2.5, as shown in Figure 3.40 We investigated

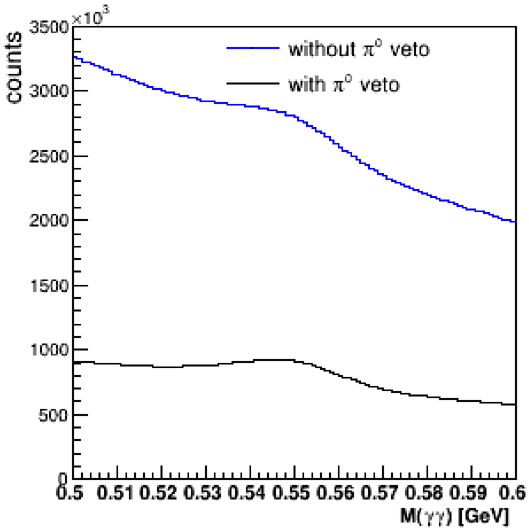

Figure 3.39: $M(\gamma\gamma)$ distribution in the full $\Upsilon(5S)$ dataset. The distribution without the π^0 veto is compare to the distribution obtained applying the π^0 veto.

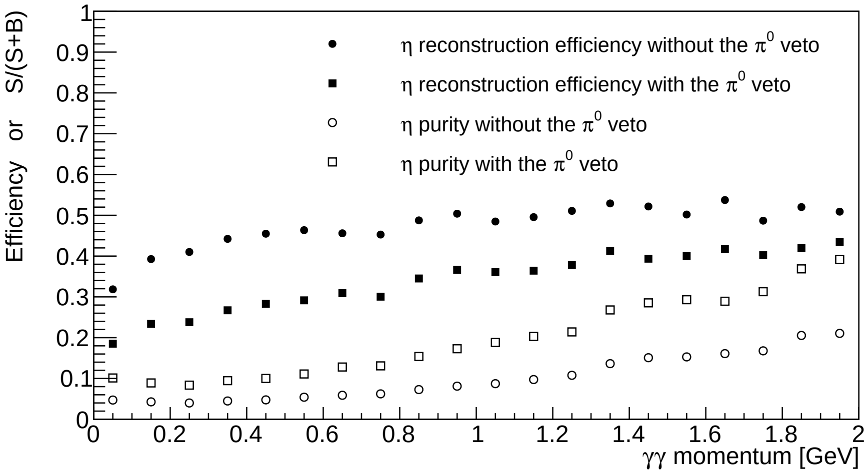

Figure 3.40: Efficiency and purity of the $\eta \rightarrow \gamma\gamma$ samples selected with and without the π^0 veto.

3.3.4 $\eta \rightarrow \pi^+\pi^-\pi^0$ selection

Previous experiences with the reconstruction of $\eta \rightarrow \pi^+\pi^-\pi^0$ already showed that the significance of the results obtained in this channel are causally much lower than the one obtained in the $\gamma\gamma$ mode. If, from one side, the recoil mass resolution in the 3π mode is smaller and thus the recoil peaks are narrower, on the other hand the reconstruction efficiency is usually a reduced by a factor four, and the branching ratio almost by a factor of two. Furthermore, the combinatorial background is larger by almost a factor of two, leading to an overall reduction of a factor ten of the significance with respect to the $\gamma\gamma$ mode. These considerations are, obviously valid for inclusive analyses. In exclusive modes with few tracks in the final state, as it happens when the Y meson are reconstructed in two lepton modes, the $\eta \rightarrow \pi^+\pi^-\pi^0$ can lead to a significant increase of the trigger efficiency. Nevertheless, a tentative analysis of the $\eta \rightarrow \pi^+\pi^-\pi^0$ channel has been made in order to provide a cross check of the results obtained in the $\gamma\gamma$ mode.

The π^0 candidates are reconstructed as previously described without any further selection. For the $\pi^+\pi^-$ pair we apply the standard Belle selection procedure for charged tracks. First, we expect both the pion to come from the primary interaction vertex, thus we reject all the tracks whose helix are not pointing to it. To discriminate among thanks compatible from the primary vertex and other tracks, either produced by the decay of long living particles or artifacts of the tracking algorithm, we calculate the *impact parameters* in the transverse plane and along the beam axis. These quantities, respectively named Δr and Δz, are the projections either on the transfer plane or on the beam axis of the distance of minimum approach between the track helix and the interaction point. The distribution of Δr and Δz for pions coming from the η decay and for all the charged tracks in the even are shown in Figure 3.41. Following the standard Belle prescriptions, we require $|\Delta r| < 1.5$ cm and $|\Delta r| < 0.5$ cm.

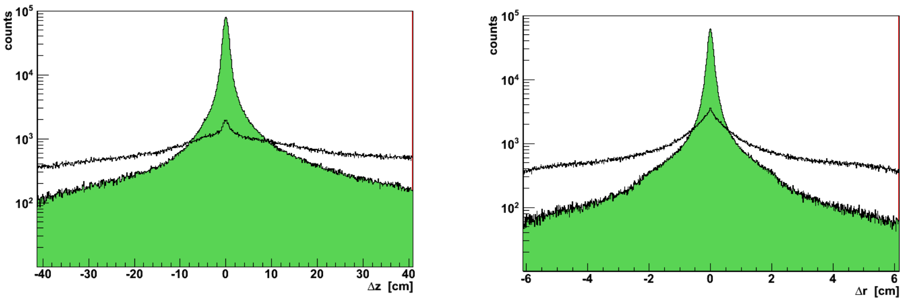

Figure 3.41: *Left*: Distribution of Δz for pions produced in η decay (green) and for other tracks in the event (white). *Right*: Distribution of Δr for pions produced in η decay (green) and for other tracks in the event (white).

In order to be selected for the η reconstruction, both the charged tracks have to be positively identified as pions. To reject kaons and protons, the standard Belle prescription is to require the likelihood ratios $\frac{\mathcal{L}_K}{\mathcal{L}_\pi} < 0.6$ (Figure 3.42) and $\frac{\mathcal{L}_p}{\mathcal{L}_\pi} < 0.6$ (Figure 3.43). In addition to that, we found a significant contamination due to electrons, therefore we add as requirement the electron probability to be less than 0.1 (Figure 3.44) [9].

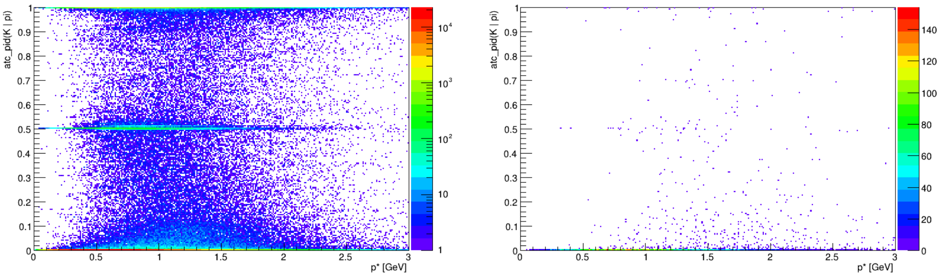

Figure 3.42: *Left*: $\frac{\mathcal{L}_K}{\mathcal{L}_\pi}$ as a function of the track momentum in CM frame for the combinatorial background in the η mass window. *Right*: $\frac{\mathcal{L}_K}{\mathcal{L}_\pi}$ as a function of the track momentum in CM frame for pions resulting from η decay.

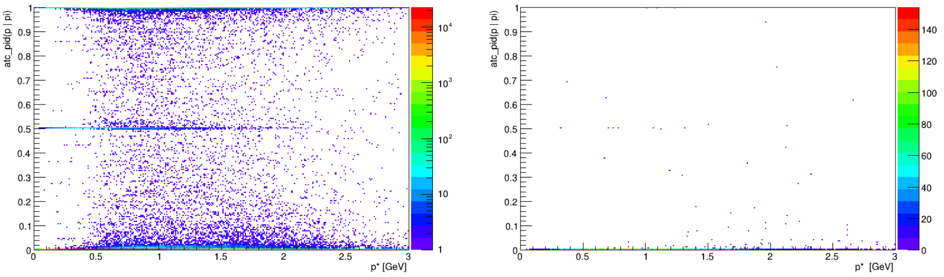

Figure 3.43: *Left*: $\frac{\mathcal{L}_p}{\mathcal{L}_\pi}$ as a function of the track momentum in CM frame for the combinatorial background in the η mass window. *Right*: $\frac{\mathcal{L}_p}{\mathcal{L}_\pi}$ as a function of the track momentum in CM frame for pions resulting from η decay.

After the removal of displaced tracks and the selection of the pions, a residual background is constituted by track pairs created by photon conversion in the detector material, which are mis-identified as pions. As shown in Figure 3.45 these events are characterized by two tracks with small opening angle. Therefore we require the cosine opening angle in the CM frame between the to tracks to be less than 0.98.

The quality of previous Belle analyses based on inclusive di-pion re-

---

[9] Please refer to Chapter 1 for the general discussion on the particle identification in Belle and the definition of PID likelihoods and electron probability.

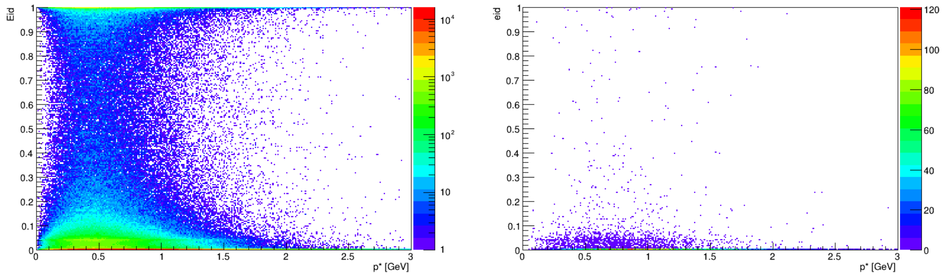

Figure 3.44: *Left*: electron ID probability as a function of the track momentum in CM frame for the combinatorial background in the η mass window. *Right*: electron ID probability as a function of the track momentum in CM frame for pions resulting from η decay.

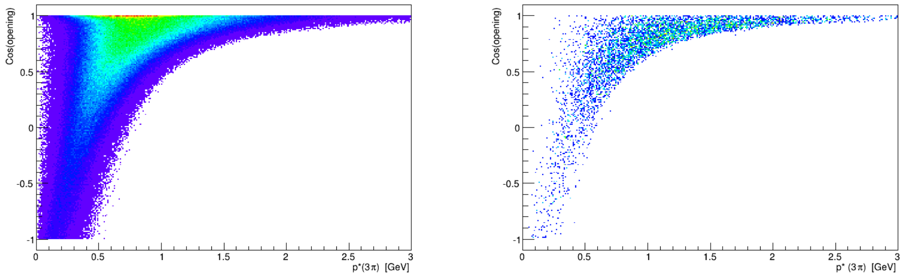

Figure 3.45: *Left*: Opening angle between of the $\pi^+\pi^-$ pair candidate for combinatorial background in the η mass window. *Right*: Opening angle between of the $\pi^+\pi^-$ pairs resulting from η decay.

construction was significantly improved by the introduction of a veto on the $K_s \to \pi^+\pi^-$ events, that represent both a source of combinatorial background and are known to produce non-smooth structures in the $\pi^+\pi^-$ recoil spectrum. Another source of combinatorial background can be due to the pions resulting from hyperon annihilations or transitions, since hyperons are known to be largely produced in bottomonium annihilations. For these reasons we studied the composition of the combinatorial background in the η mass window, shown in Figure 3.46.

Contrary to what was observed in the $\eta \to \gamma\gamma$ case, where a dominant source of background was identified, in this case there is no such process,

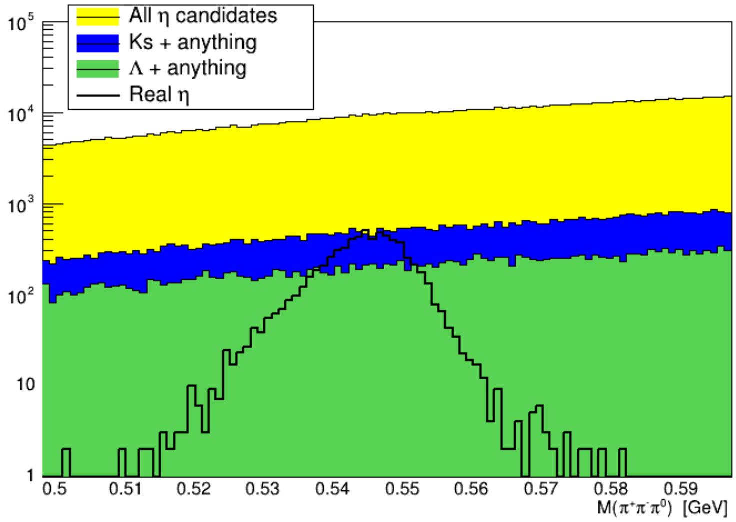

Figure 3.46: Different contributions to the $\pi^+\pi^-\pi^0$ invariant mass in the η mass region.

and the difference contributions are almost equally contributing. The bulk of the combinatorial background is due to light meson decay, such as $\rho \to \pi^+\pi^-$, which are very difficult to be efficiently vetoed due to their large natural width. Therefore, no K_s or other veto can be applied, and the irreducible, combinatorial background level in the η region remains very high. Indeed, S/B ratio of the $\eta \to \pi^+\pi^-\pi^0$ is found to be significantly lower than in the case of the $\eta \to \gamma\gamma$. The expected statistical significance of the $h_b(1,2P)$ signals in the $\eta \to \pi^+\pi^-\pi^0$ mode are less than 1 σ, thus this mode is excluded from the analysis and the η are reconstructed in the two photons mode only.

3.3.5 Continuum suppression

Foor the B meson analysis a sophisticate and successful approach to the continuum rejection has been developed, combining 17 event-shape observable in one single discriminant obtained with the Fisher technique.

This discriminant is intimately connected with the nature of an $\Upsilon(4S) \to B\bar{B}$ event which is overall spherical but can be further divided into two spherical part, each one corresponding to the annihilation of the B mesons (respectively signal and tag). Therefore many different fox-wolfram moments can be constructed either using all the tracks in the event, or only the ones associated to the decay of one of the two B. The current algorithm requires 16 FW-like moments, which combines charged tracks, neutral clusters and missing momentum from both signal and tag B:

$M_n^{st,c}$, with $n = 0...4$ (all signal tracks + tag charged tracks)
$M_n^{st,n}$, with $n = 0, 2, 4$ (all signal tracks + tag neutral tracks)
$M_n^{st,m}$, with $n = 0, 2, 4$ (all signal tracks + tag missing momentum)
M_n^{tt}, with $n = 0...4$ (all tag tracks) ,

and the value of r the transverse missing energy E_T. Further reduction is obtained creating a likelihood ratio which takes into account the presence of displaced vertexes, the value of the Fisher discriminant, the angular distribution of the thrust axis and the angular distribution of the B meson. The angular distribution of the B meson emission direction with respect to the beam axis, which is expected to be proportional to $1 + \cos^2\theta$ for real B and flat for combinatorial backgrounds. The performances of this Likelihood discriminant are shown in Figure 3.47 Despite the success of this algorithm, it cannon be used for bottomonium analyses where a spherical sub-event is not present. The standard procedure used by the Belle quarkonium group for rejecting the continuum contribution is based only on the 2nd order Fox-Wolfram moment $R2$. This approach has been proved to be efficient, robust and precise, with a quite small systematic uncertainty. We therefore reject the continuum $e^+e^- \to q\bar{q}$ background requiring the ratio between the 2nd- and 0th- order Fox Wolfram Moment to be less than 0.30. The optimal value has been chosen as the one that

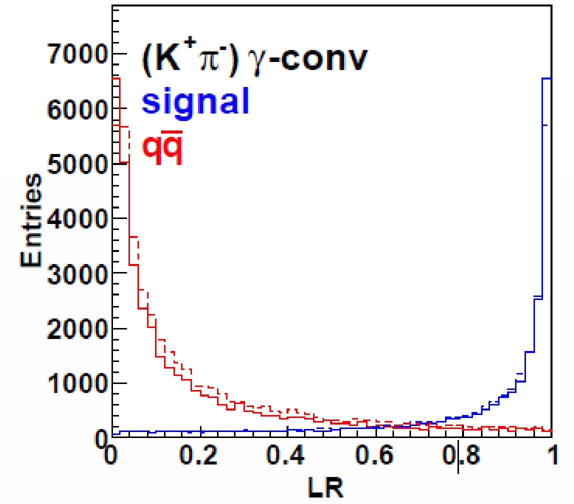

Figure 3.47: Distribution of the event shape likelihood ratio for continuum events and $\Upsilon(4S) \to B\bar{B}, B \to K + \pi^-$ events.

maximizes the significance of the $\Upsilon(5S) \to \eta h_b(nP)$ peaks in the MC simulation. A cross check is preformed on the data studying the significance of the $\Upsilon(5S) \to \pi^+\pi^-\Upsilon(2S)$ peak: the optimal value of $R2 < 0.30$ is in agreement with what is expected.

Nevertheless we noticed that the problem of the continuum rejeciton in bottomonium anlyses was generaly overlooked in the past, while more sofisticate thecnique inspired by the Belle's one can significanlty improove the quality of the analyses performend at the $\Upsilon(4S)$ and $\Upsilon(5S)$ energy. In the Appendix B we present the results of some early investigations in this direction, and the prospect for future developments.

3.3.6 Efficiency and resolution

After the selection the reconstructed $\eta \to \gamma\gamma$ candidates in the region of mass between 0.48 GeV and 0.62 GeV, we further reduce the window in which the good η candidates are searched for. The signal region is within 13 MeV from the nominal η mass ($\pm 2\sigma$ region), while a sideband sample is constructed with the candidates with invariant mass outside a $\pm 3\sigma$ region, but within the $[0.48, 0.62]$ GeV interval. A kinematic fit with mass constrain is applied to all the η candidates in order to improve the recoil mass resolution.

The reconstruction efficiency and the MC-based resolution of the recoil mass peak are summarized in table B.1.

Table 3.5: Reconstruction efficiency and MM(η) resolution in MC. The peak position corresponds to the fitted recoil mass in MC events.

Channel	Efficiency [%]	Position [GeV]	Resolution [MeV]
$\Upsilon(5S) \to \eta h_b(1P)$	20.70%	9.899	10.3
$\Upsilon(5S) \to \eta h_b(2P)$	16.34%	10.26	6.52
$\Upsilon(5S) \to \eta \Upsilon(1S)$	17.63%	9.560	15.5
$\Upsilon(5S) \to \eta \Upsilon(2S)$	15.74%	10.022	8.77
$\Upsilon(5S) \to \eta \Upsilon(1D)$	16.74%	10.16	7.22
$\Upsilon(1D) \to \eta \Upsilon(1S)$ in $\Upsilon(5S)$ data	17.32%	10.165	13.4
$\Upsilon(4S) \to \eta h_b(1P)$	16.96%	9.899	7.10
$\Upsilon(4S) \to \eta \Upsilon(1S)$	17.20%	9.460	12.1
$\chi_{b0}(2P) \to \eta \eta_b(1S)$ in $\Upsilon(4S)$ data	19.35%	9.747	14.8
$\Upsilon(1D) \to \eta \Upsilon(1S)$ in $\Upsilon(4S)$ data	14.57%	9.877	10.6

The inclusive η recoil mass distribution obtained from the generic MC sample is shown in Figure 3.48.

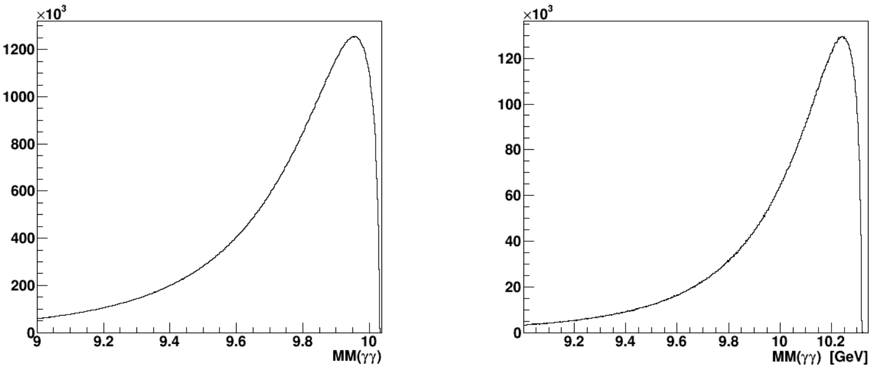

Figure 3.48: η recoil in MC background events, for $\Upsilon(4S)$ (left) and $\Upsilon(5S)$ generic MC.

In the next chapter we will discuss the fitting procedure adopted for the signal extraction, and we will present the results of the analysis of the data samples.

Chapter 4

Fit of the η recoil mass on the data samples

4.1 Fitting procedure

4.1.1 Signal PDF

When the radiative corrections are neglected, the signal peaks that appear on top of the combinatorial background are described by Gaussian PDFs, whose width is determined by the detector resolution. The ISR however introduces a radiative tail towards lower recoil masses, which can be phenomenologically described by a power law. Here we describe the method used for the determination of the tail parameters, focusing on the case of $\Upsilon(4S) \to \eta h_b(1P)$. The same argument and the same conclusion can be applied to any of the signal channels, both at $\Upsilon(4S)$ and $\Upsilon(5S)$ energy.

According to the MC simulations, the detector resolution on the η missing mass is 7.1 MeV/c^2. However the $\Upsilon(4S)$ has a non-negligible physical width $\Gamma_{\Upsilon(4S)} = 20.5$ MeV, therefore the emission of a soft ISR photon with energy of few MeV can lower the effective CM energy of the e^+e^- collision, that however results in the production of an $\Upsilon(4S)$. In order to model this effect we first convolve the detector resolution with the distribution of the ISR emission probability as function of the γ_{ISR} energy. The resulting distribution is weighted with a Breit-Wigner peak that describes the $\Upsilon(4S)$ line shape. The final distribution is well described by a Crystal Ball PDF that phenomenologically describes the radiative tail. Figure 4.1 shows the evolution of the PDF under the effects of the ISR and the finite $\Upsilon(4S)$ width.

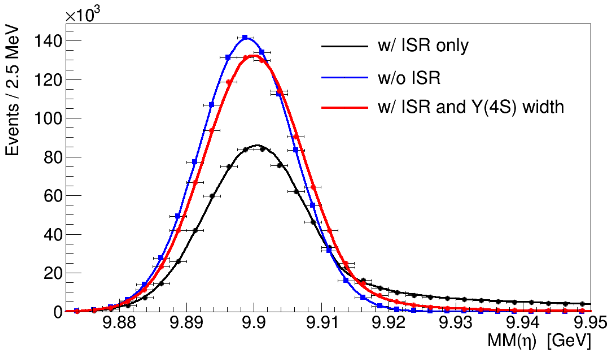

Figure 4.1: Signal PDF accounting the detector resolution only (blue dots), after the convolution of the detector resolution with the ISR PDF (black dots) and after the inclusion of IRS and $\Gamma_{\Upsilon(4S)}$ (red dots). The different curves show the result of the crystal-ball fits.

4.1.2 Background PDF

While the construction of the signal PDF using the MC simulation is rather straightforward, since it depends only on the detector resolution, which is well known thanks to the photon energy re-calibration, and on the ISR radiator which is also a rather well-known quantity, the description of the background shape is more challenging. We tested two different strategies for solving this problem: a completely phenomenological approach, modeling the background as a polynomial function, and a more physical approach. In principle the background PDF $B(M_{miss})$

should be constructible from two separate functions, both with physical meaning: $\epsilon(M_{miss})$ describing the reconstruction efficiency and $P(M_{miss})$ describing the initial η spectrum. The final PDF would be $B(M_{miss}) = \epsilon(M_{miss}) \cdot P(M_{miss})$. We attempted to follow this approach with different choices of $P(M_{miss})$, testing either a Boltzmann , a modified Tsallis or an Argus distribution, and parameterizing $\epsilon(M_{miss})$ with a Chebyshev polynomial. All our attempts to archieve a good description of the data by this mean failed, either because of a wrong assumption for the emission spectra or for an inadequate modeling of the η reconstruction efficiency. Indeed the $P(M_{miss})$ we tested are known to properly describe the data in high energy collisions, where a thermodynamical description of the fireball evolution is justified. In our case this assumption is questionable, both because of the low final state multiplicity and for the presence of many different emission processes (a residual contribution from the continuum, the bottomonium annihilation and the B meson decay) which are hardly describable by the very same PDF. The proper modeling of the reconstruction efficiency is a non-trivial problem. While the angular distribution for the signal η is known and modeled by the MC simulation, for generic η the discrepancies between data and MC would require ϵ to be at least function of the missing mass and the polar angle of the η candidate. This requirement introduces large systematic uncertainty in the ϵ parametrization and would require a dedicated study, which is beyond the scope of this work.

On the other hand the parametrization of $B(M_{miss})$ as a high order Chebyshev polynomial was already proven to be a simple and successful strategy by previous Belle analyses, therefore we decided to apply this strategy. Even with this approach the complete fit of the whole spectrum from 9.0 GeV$/c^2$ up to the kinematic limit is hardly converging, mainly because of the sharp kinematic cutoff at high masses. Therefore, in order to ensure the convergence of the fit, we divide the recoil mass distribution in several regions, each one to be fitted separately.

4.1.3 Fit conditions

In the $\Upsilon(4S)$ sample the fit is performed in two separated regions: the first one, which includes the $\Upsilon(1S)$ peak, spans from 9.3 GeV/c^2 to 9.7 GeV/c^2; the second one, which includes the $h_b(1P)$ region, spans from 9.7 GeV/c^2 to 10 GeV/c^2. The signals are modeled, as mentioned above, with two Crystal-Ball shaped peaks, one describing the $\Upsilon(1S)$ and one describing the $h_b(1P)$, whose parameters are fixed according to the MC simulation except for the mass of the $h_b(1P)$ and the yields, $N_{\Upsilon(1S)}$ and $N_{h_b(1P)}$, that are left floating. The background is described in both the regions with a Chebyshev Polynomial PDF. In the low M_{miss} range the order of the polynomial is 6, while the high M_{miss} one requires an 11th order PDF. In order to determine the polynomial order and the fit range for high mass region, we explore different possibilities. We consider three different intervals, $(9.6, 10)$, $(9.7, 10)$, and $(9.8, 10)$. For each interval we test the fit with a polynomial order ranging from 5 to 13. We observe a good fit result using a polynomial order between 9 and 12 in the first and second interval, and between 7 and 9 in the third one. The best fit is obtained with a 11^{th} order polynomial in the range $(9.7, 10)$, which is thus chosen as nominal one. We will use the other configurations in order to estimate the systematic uncertainty related to the background fit.

In the low M_{miss} range the fit is overall more stable, and we get a good fit quality with a 6^{th} order polynomial in the $(9.3, 9.7)$ range. Other possible combinations will be used for the estimation of the systematic uncertainties.

In the $\Upsilon(5S)$ the fit is divided into two regions, the first one from $M_{miss} = 9.30$ GeV to $M_{miss} = 9.70$ GeV and the second one from $M_{miss} = 9.70$ GeV to $M_{miss} = 10.30$ GeV, and we use the same PDF used for the

$\Upsilon(4S)$ case.

Even if the PDF shape is determined on the MC samples, in the data fit the background parameters must be left floating, since the MC do not give a perfect description of its shape, as can be seen in Figure 4.2 and 4.3.

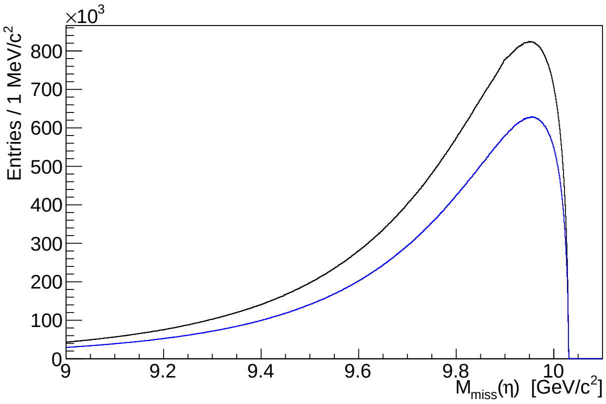

Figure 4.2: $\eta \to \gamma\gamma$ recoil mass spectrum in $\Upsilon(4S)$ data and in the generic MC.

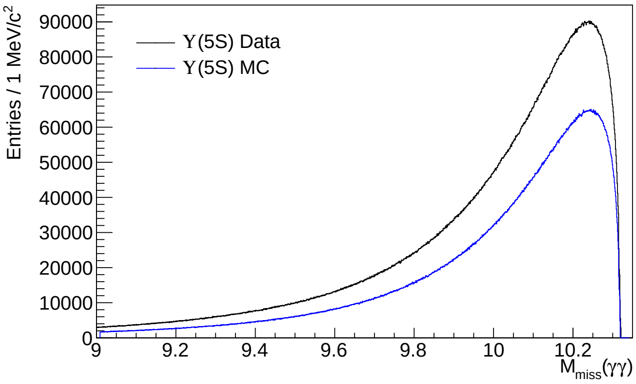

Figure 4.3: $\eta \to \gamma\gamma$ recoil mass spectrum in $\Upsilon(5S)$ data and in the generic MC.

The fit is performed on binned samples with a bin width 0.1 MeV/c^2. Thinner binnings are shown not to improve the results, and different binning values are used to evaluate the systematic uncertainties. The residual distributions, used to present the results, are chosen to have a 1 MeV/c^2 bin width to improve the readability.

4.2 Fit of the $\Upsilon(4S)$ sample

4.2.1 Fit of the $\eta \to \gamma\gamma$ sideband and MC samples

To check the fitting procedure and exclude the presence of non-η peaking contributions in the $M_{miss}(\eta)$ distribution we first apply the fitting procedure to the pure background MC and to the recoil mass distribution obtained from the η mass sidebands in the data sample. The results are shown in Figure 4.4 and 4.5

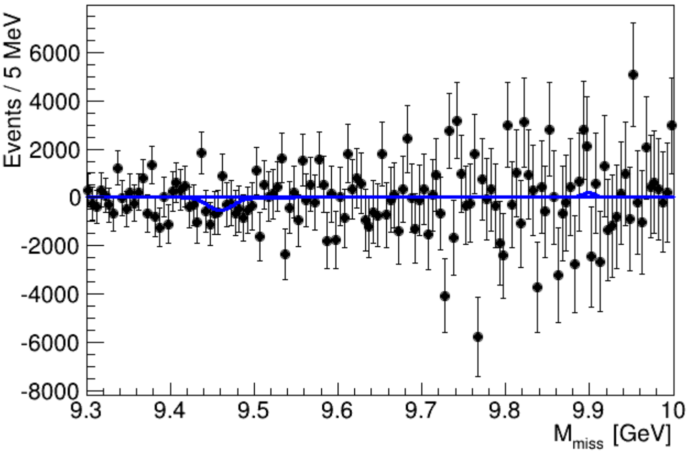

Figure 4.4: $\gamma\gamma$ recoil mass in $\Upsilon(4S)$ the data sample for $\gamma\gamma$ pairs belonging to the η mass sideband region, after the subtraction of the background component.

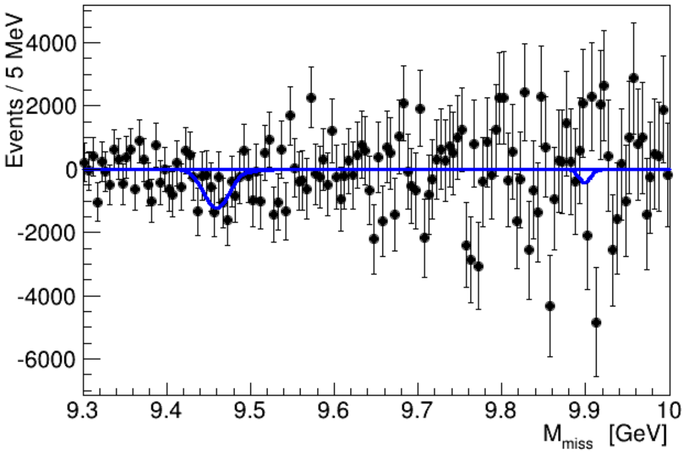

Figure 4.5: $\gamma\gamma$ recoil mass in background MC sample for $\gamma\gamma$ pairs belonging to the η mass region, after the subtraction of the background component.

No peaking structure is found in either of the fits.

Before fitting the data we perform the fit on an MC sample with $N^{MC}_{h_b(1P)} = 96150$ and $M^{MC}_{h_b(1P)} = 9899.0$ MeV/c^2. The result of the fit, shown in Figure 4.6 is $N^{fit}_{h_b(1P)} = 102562 \pm 4870$ and $M^{fit}_{h_b(1P)} = 9898.8 \pm 0.3$ MeV/c^2, in complete agreement whit the original values. For this test we infer no significant bias is introduced by the fitting procedure.

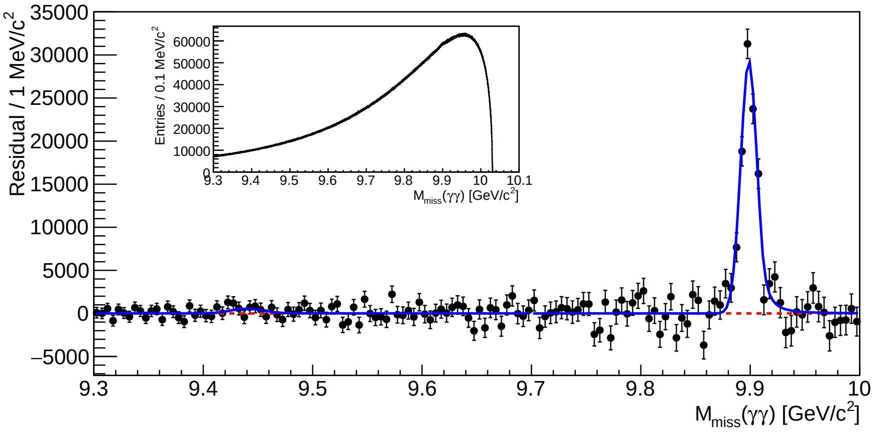

Figure 4.6: $\gamma\gamma$ recoil mass in the η mass region from the MC simulation, after the subtraction of the background component. The inset shows the distribution before the background subtraction.

4.2.2 Fit of the $\eta \to \gamma\gamma$ signal sample

The result of the fit on the data sample is shown in figure 4.7. The confidence levels of the fit are 1% in the lower region and 19% in the upper one. We observe a peak in correspondence of the $\Upsilon(4S) \to \eta h_b(1P)$ with a statistical significance of 11 σ and we measure $N_{h_b(1P)} = 112469 \pm 5537$. From the position of the $h_b(1P)$ peak position we determine $M_{h_b(1P)} = 9899.27 \pm 0.40$ MeV/c^2, where the error is statistical. In the $\Upsilon(1S)$ region we measure $N_{\Upsilon(1S)} = 4230$ with a statistical significance of 1.9σ. The correspondent 90% CL upper limit on the $\Upsilon(1S)$ yield is $N^{UL}_{\Upsilon(1S)} = 13900$, including the effect of the systematic uncertainties.

4.2.3 $\eta \to \pi^+\pi^-\pi^0$ fit

We study the $\eta \to \pi^+\pi^-\pi^0$ mode as a validation of the measurement. The fitting procedure is identical to the one used for the $\eta \to \gamma\gamma$ sample, and the signal PDF parameters are set according to the MC simulation. We measure $\mathcal{B}[\Upsilon(4S) \to \eta h_b(1P)]_{\eta\to\pi^+\pi^-\pi^0} = (2.3 \pm 0.6(\text{stat.})) \times 10^{-3}$ with a

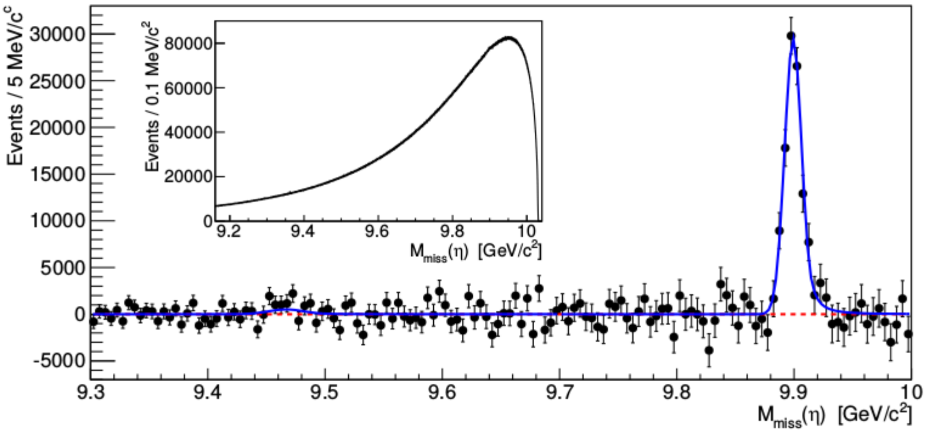

Figure 4.7: $\gamma\gamma$ recoil mass in the η Mass region, after the subtraction of the background component. The inset shows the distribution before the background subtraction.

reconstruction efficiency of 4.5% and a significance of 3.5σ, which is in agreement with the $\gamma\gamma$ mode. The result of the fit is shown in Figure 4.8.

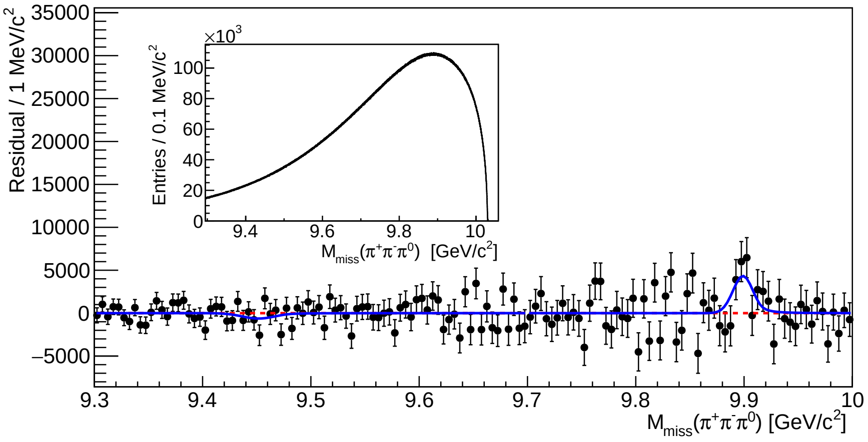

Figure 4.8: $\pi^+\pi^-\pi^0$ recoil mass in the η Mass region, after the subtraction of the background component. The inset shows the distribution before the background subtraction.

4.2.4 Systematic errors

The different contributions to the systematic uncertainties are summarized in table 4.1.

Table 4.1: Systematic uncertainties in the determination of the number of $h_b(1P)$ and $\Upsilon(1S)$, in units of %, and on $M_{h_b(1P)}$ in units of MeV/c^2.

Source	$N_{h_b(1P)}$	$N_{\Upsilon(1S)}$	$M_{h_b(1P)}$
Background order and range	±2.4	±7.1	±0.1
Bin width	±2.5	±2.4	±0.1
ISR modeling	±2.8	±2.6	±0.7
γ energy calibration	±1.2	±1.4	±0.3
Peaking backgrounds	±0.5	-	±0.4
Reconstruction efficiency	±6.6	±8.2	-
$N_{\Upsilon(4S)}$	±1.4	±1.4	-
Beam energy calibration	±0.0	±0.0	±0.4
$\mathcal{B}[\eta \to \gamma\gamma]$	±0.5	±0.5	-
Total	±8.2	±11.6	±1.0

Fitting procedure The main contribution to the systematic uncertainty comes from fit-related effects. First we study the fluctuation of signal yield as function of the fit range and the polynomial order. For each range-order combination we require the confidence level of the fit to be compatible with the one obtained in with the nominal configurations. All the measured values of $N_{\Upsilon(1S)}$, $N_{h_b(1P)}$ and $M_{h_b(1P)}$ are compatible within the statistical errors, with the average fluctuations $\sigma(N_{h_b(1P)}) = \pm 2.4\%$, $\sigma(N_{\Upsilon(1S)}) = \pm 7.1\%$ and $\sigma(M_{h_b(1P)}) = 0.1$ MeV.

We study the uncertainty related to the bin width repeating the fitting procedure with bin width ranging from 0.1 MeV to 1 MeV. We observe the fluctuations $\sigma(N_{h_b(1P)}) = \pm 2.5\%$, $\sigma(N_{\Upsilon(1S)}) = \pm 2.4\%$ and $\sigma(M_{h_b(1P)}) = 0.1$ MeV.

ISR modeling. The uncertainty introduced by the ISR modeling is entirely related to the uncertainty on the $\Upsilon(4S)$ width, $\Gamma_{\Upsilon(4S)} = 20.5 \pm 2.5$

MeV. We re-calculate the signal CB parameters varying the $\Upsilon(4S)$ width within $\pm 1\sigma$, obtaining a $\pm 2.8\%$ fluctuation in the $h_b(1P)$ yield, a $\pm 2.6\%$ fluctuation in the $\Upsilon(1S)$ upper limit and a ± 0.7 MeV fluctuation of the $M_{h_b(1P)}$ value.

As cross check we tested alternative tools for the ISR modeling, using a mixed sample of direct $\Upsilon(4S)$ decays and $\Upsilon(4S)$ ISR events generated using the VECTORISR model provided by the EvtGen MC generator. The VECTORISR model has been developed for the simulation of the production of low mass states in ISR processes, therefore it's expected to describe the soft ISR emission only within a few percent approximation. We noticed that the emission of ISR photons with energy less than 5 MeV, lower than the intrinsic energy spread of the e^- beam which is already included in the MC simulation, does not significantly affect the $M_{miss}(\eta)$ resolution. Therefore we can avoid to use VECTORISR to model very soft photons limiting its usage to events with $E(\gamma)_{ISR} > 5$ MeV, and obtain the final distribution by mixing two MC samples, one with ISR and one without ISR. From the theoretical distribution we calculate the probability of emitting a photon with energy greater than 5 MeV, $P(E(\gamma)_{ISR} > 5\text{MeV}) = 7.23\%$, and we re-weight the samples accordingly. Fitting of the data sample with the PDFs obtained with the two different methods we estimate a difference of only $\pm 3.5\%$ in the signal yield, which suggests that our analytical approach is correctly describing the signal PDF.

γ **energy calibration.** We assume a $\pm 0.2\%$ error on the absolute photon energy scale $\mathcal{F}_{en}$ since we observe a systematic 0.2% shift between the measurement obtained with $\pi^0 \to \gamma\gamma$ and the one obtained with the $D^{*0} \to D^0\gamma$. To evaluate how this uncertainty propagates to the final results, we calculate the reconstruction efficiency and the signal fit parameters varying $\mathcal{F}_{en}$ by ± 0.002, and we compare the results of the fit on the data under the different assumptions. We observe no significant fluctuation at the level of 0.01 MeV on $M_{h_b(1P)}$. The corresponding uncertainty on the signal yield is 0.2%.

The value of the fudge factor $\mathcal{F}_{res}$ influences both the reconstruction efficiency, because of the presence of the minimum photon energy requirements, the η mass window and the π^0 veto, and the fitting procedure, through the value of the signal peak resolution. In order to estimate these effects we repeat the analysis assuming three different smearing scenarios: the first one, using the central value of the smearing, the second one obtained lowering $\mathcal{F}_{res}$ by 1σ, an the third one obtained increasing $\mathcal{F}_{res}$ by 1σ. Comparing the branching fraction and the mass measurements obtained in the three scenarios, we estimate the corresponding uncertainties due to the photon energy calibration. Including the contribution due to the uncertainty on β we obtain: $\sigma(N_{h_b(1P)}) = \pm 1.2\%$, $\sigma(N_{\Upsilon(1S)}) = \pm 1.4\%$, and $\sigma(M_{h_b(1P)}) = 0.1$ MeV.

Peaking backgrounds. The $\Upsilon(4S) \to \eta h_b(1P)$ transition may suffer from a peaking background from the transition $\Upsilon(1D) \to \eta \Upsilon(1S)$, where the $\Upsilon(1D)$ is produced via the radiative cascade $\Upsilon(4S) \to \gamma \chi_{b0}(2P) \to \gamma\gamma\Upsilon(1D)$. Even if the η recoil peak for this transition is Doppler-shifted, we found that a Gaussian PDF properly describes it. Including this component into the fit we observe no significant signal of $\Upsilon(1D) \to \eta\Upsilon(1S)$, with a fitted yield compatible with 0 and an upper limit $N^{UL}_{\Upsilon(1D)} = 4210$, including the systematic uncertainties. The χ^2/NDF shows that no significant change in the fit performances can be archieved including this component. The 0.5% difference between the two fitted $\Upsilon(4S) \to \eta h_b(1P)$ yields will be included in the systematic uncertainties.

Reconstruction efficiency. Different sources contributes to the uncertainty on reconstruction efficiency. Using the 121.4 fb^{-1} collected at the $\Upsilon(5S)$ energy, we reconstruct the $\Upsilon(5S) \to \pi^+\pi^-\Upsilon(2S)$ transitions and we compare the R_2 shape obtained from the data with the simulated one, as shown in figure 4.9, we determine a ±3% uncertainty related to the continuum rejection.

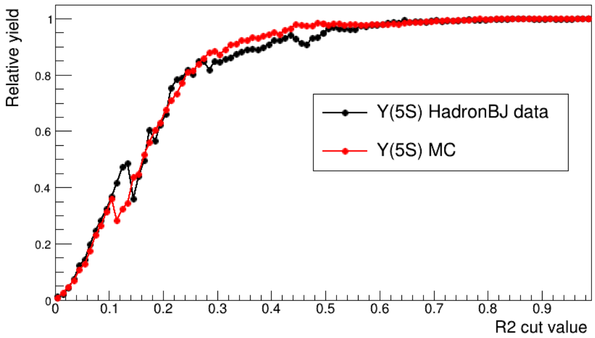

Figure 4.9: Comparison between the fitted yield of $\Upsilon(5S) \to \pi^+\pi^-\Upsilon(2S)$ events in the data and in the MC simulation, as a function of the R_2 requirement.

$h_b(1P)$ decays are expected to produce ggg and gg final states with almost the same probability, while the $\Upsilon(2S)$ sample used for the estimation of the systematic uncertainty is expected to contain 10% of gg events, while the remaining 90% is composed predominantly of ggg (80%). However, we observe that the gg and ggg produce very similar R_2 distributions in the MC simulation (figure 4.10), so the usage of $\Upsilon(5S) \to \pi^+\pi^-\Upsilon(2S)$ as control sample is not expected to introduce large errors.

The $\Upsilon(1S)$ decay table used for this analysis includes the leptonic modes $\Upsilon(1S) \to \mu^+\mu^-, e^+e^-$, that account for a total 5% of the branching ratio. We expect those events not to pass the HadronBJ selection, with a correspondent reduction of the reconstruction efficiency. We check the HadronBJ selection efficiency and we found $\epsilon_{HBJ} = 90\%$, while $\epsilon_{HBJ} = 95\%$ was expected assuming all the non-leptonic final states to pass the hadronic selection. We ascribe this effect to the $\Upsilon(1S)$ decays with less than four charged tracks in the final state. Since we have no validation

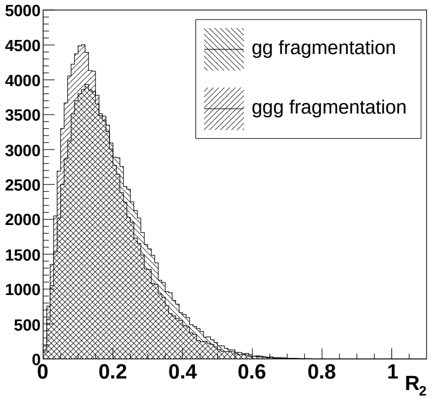

Figure 4.10: Comparison between the R_2 distribution in ggg and gg fragmentation.

available for MC simulation of the $\Upsilon(1S) \to ggg$ fragmentation into few hadrons, we assume the 5% difference between the expected and observed values of ϵ_{HBJ} as systematic uncertainty. The same argument applies to the $h_b(1P)$ decay: in this case a find a discrepancy of $\pm 1\%$.

The π^0 veto efficiency is studied in MC and Data sample comparing the number of $\eta \to \gamma\gamma$ candidates as function of the $\gamma\gamma$ momentum, with and without the veto. In Figure 4.11 we present the ratio $\frac{N(\eta)_{Veto}}{N(\eta)_{NoVeto}}$. No significant discrepancy between MC and Data is found, thus we don't add a systematic uncertainty related to this procedure.

The uncertainty on the photon reconstruction efficiency is estimated using the previous Belle study on $D \to K^{\pm}\pi^{\mp}\pi^0$ events to be $\pm 2.8\%$ per photon, corresponding to $\pm 5.6\%$ per η. The number of $\Upsilon(4S)$ events is known with a relative uncertainty of $\pm 1.4\%$. Finally, an uncertainty on the branching fractions of the η decay modes is included according to the PDG values.

Beam energy calibration The beam energy spread is included in the MC simulation and is therefore already accounted for by the MC resolution.

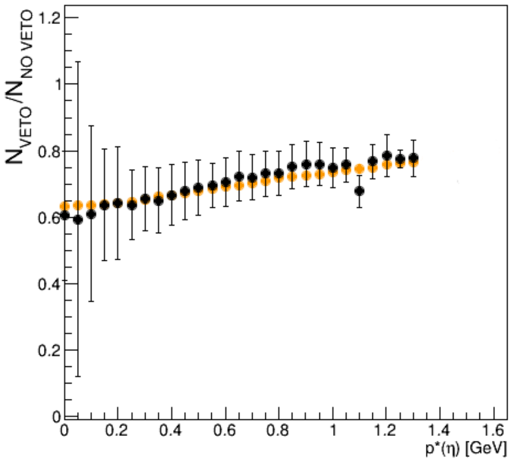

Figure 4.11: Ratio between the number of $\eta \to \gamma\gamma$ fitted with and without applying the π^0 veto, as a function of th momentum of the $\gamma\gamma$ pair. The distribution observed in the data sample (black dots) is found to be in agreement with the MC expectation (Orange, dotted distribution).

Its central value in Belle is calibrated using fully reconstructed B meson decays. In order to do that the *beam constrained mass* M_{bc} is first calculated as

$$M_{bc} = \sqrt{E_n^2 - p_B^2},$$

where E_n is the nominal beam energy in the CM frame and p_B is the B meson momentum. The corrected beam energy E_c is then calculated as

$$E_c = E_n - \frac{m_B}{E_n}(M_{bc} - m_B),$$

where m_B is the nominal B meson mass. Therefore the uncertainty on the B meson mass propagates to the corrected beam energy value, and this effect is not included in the standard MC simulation.

To evaluate it we perform a Toy-MC simulation, measuring the reconstructed $h_b(1P)$ mass as function of the B mass value assumed for the calculation of E_c. The result of the simulation of 10000 values of m_B, Gaussian distributed around the nominal value with a resolution equal to the m_B error reported by the PDG is shown in Figure 4.12

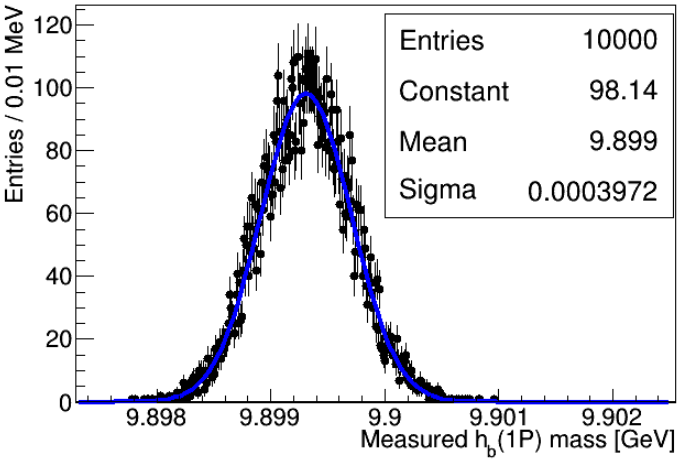

Figure 4.12: Fluctuation of the measured $h_b(1P)$ mass if the mass of the B meson used for the beam energy calibration is Gaussian floated within ± 0.17 MeV/c^2 from the nominal value of 5.2793 MeV/c^2.

The corresponding fluctuation of ± 0.4 MeV/c^2 on the measurement of the $h_b(1P)$ mass is assumed as systematic uncertainty related to the beam energy calibration.

η parameters The branching ratio $\mathcal{B}[\eta \to \gamma\gamma]$ is known with a $\pm 0.5\%$ accuracy according to the Particle Data Group. The η mass value used in the kinematic fit may affect the $h_b(1P)$ mass measurement. We repeat the kinematic fit varying the η mass within ± 0.02 MeV the central value (corresponding to a $\pm 1\sigma$ interval), without observing any significant shift in the $h_b(1P)$ peak position.

Luminosity We assume that the number of $\Upsilon(4S)$ is $N_{\Upsilon(4S)} = (771.581 \pm 10.566) \times 10^6$ thus we assign a 1.7% of uncertainty to the branching fractions measured at the $\Upsilon(4S)$.

4.2.5 Results

We observe for the first time the transition $\Upsilon(4S) \to \eta h_b(1P)$ with statistical significance of 11σ, and we measure a branching ratio

$$\mathcal{B}[\Upsilon(4S) \to \eta h_b(1P)] = (2.18 \pm 0.11 \pm 0.18) \times 10^{-3}.$$

The $\Upsilon(4S) \to \gamma\chi_{bJ}(2P) \to \gamma\gamma\Upsilon(1D) \to \gamma\gamma\eta\Upsilon(1S)$ process is not observed. We estimate an upper limit for the branching ratio

$$\mathcal{B}[\Upsilon(4S) \to \gamma\chi_{bJ}(2P) \to \gamma\gamma\Upsilon(1D) \to \gamma\gamma\eta\Upsilon(1S)] < 0.8 \times 10^{-4},$$

We do not report any new evidence for the transition $\Upsilon(4S) \to \eta\Upsilon(1S)$, and we determine the 90% CL upper limit

$$\mathcal{B}[\Upsilon(4S) \to \eta\Upsilon(1S)] < 2.7 \times 10^{-4},$$

which is compatible with the previous observation of this transition, that reported $\mathcal{B}[\Upsilon(4S) \to \eta\Upsilon(1S)] = 1.96 \pm 0.06 \pm 0.06 \times 10^{-4}$.

Finally, we report a new measurement of the $h_b(1P)$ mass:

$$M_{h_b(1P)} = 9899.3 \pm 0.4 \pm 0.9 \text{ MeV/c}^2.$$

4.3 Fit of the $\Upsilon(5S)$ sample

The fit of the $\Upsilon(5S)$ data sample is performed with the very same strategy and conditions used for the fit of the $\Upsilon(4S)$ one.

4.3.1 Fit on the Data sample

The results of the fit are shown in Figure 4.13.

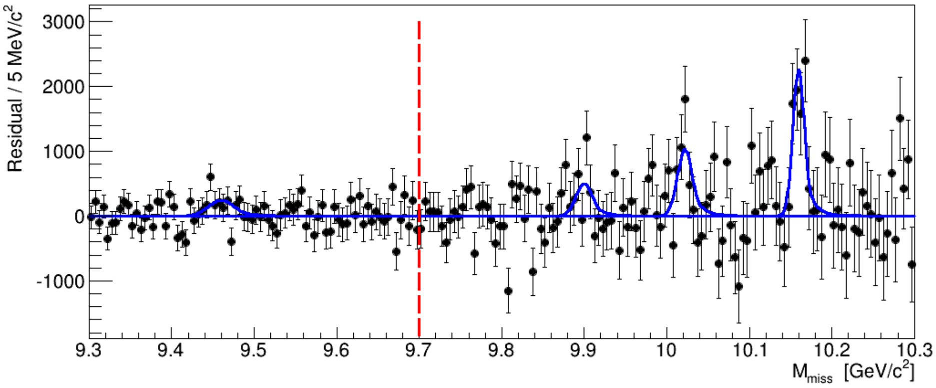

Figure 4.13: Residual from the background fit in $\Upsilon(5S)$ Dataset.

The only signals with significance higher than 3σ are $\Upsilon(5S) \to \eta\Upsilon(1D)$ and $\Upsilon(5S) \to \eta\Upsilon(2S)$; we cannot claim evidences of the transitions $\Upsilon(5S) \to \eta h_b(1,2P)$ or $\Upsilon(5S) \to \eta\Upsilon(1S)$. The fitted yields and the correspondent upper limits are reported in Table 4.2

Table 4.2: Significances, yields and correspondent upper limits for the signal processes in $\Upsilon(5S)$ decays.

Channel	Significance	N_{meas}	N_{UL}
$\Upsilon(5S) \to \eta\Upsilon(1S)$	1.8σ	2970 ± 1657	7459
$\Upsilon(5S) \to \eta h_b(1P)$	2.4σ	2742 ± 1489	9222
$\Upsilon(5S) \to \eta\Upsilon(2S)$	3.3σ	5016 ± 1635	
$\Upsilon(5S) \to \eta\Upsilon(1D)$	5.3σ	8563 ± 1718	
$\Upsilon(5S) \to \eta h_b(2P)$	$<1\sigma$	26 ± 363	8017

4.3.2 Systematic errors

We assume that the number of $\Upsilon(5S)$ is $N_{\Upsilon(5S)} = (41.28 \pm 2.15) \times 10^6$, thus we assign a 4.9% of uncertainty to the branching fractions measured at the $\Upsilon(5S)$. The number of $\Upsilon(5S)$ is calculated as $N_{\Upsilon(5S)} = \mathcal{L} \cdot \sigma(e^+e^- \to b\bar{b})$, where $\mathcal{L} = 121.4$ fb-1 is the collected luminosity and $\sigma(e^+e^- \to b\bar{b}) = 0.34$ nb is the cross section of the $\Upsilon(5S)$ production. For the uncertainty we assume $\sigma_{crosssection} = 4.7\%$ and $\sigma_{luminosity} = 1.4\%$.

A peaking background from $\Upsilon(5S) \to \pi^+\pi^-\Upsilon(1D) \to \eta\Upsilon(1S)$ can affect the measurement of $\mathcal{B}[\Upsilon(5S) \to \eta\Upsilon(1D)]$. Combining a recent unpublished measurement by Belle of the branching ratio $\mathcal{B}[\Upsilon(5S) \to \pi^+\pi^-\Upsilon(1D) \to \gamma\gamma\Upsilon(1S)]$[1] and the upper limit $\frac{\Upsilon(1D)\to\eta\Upsilon(1S)}{\Upsilon(1D)\to\gamma\gamma\Upsilon(1S)} < 0.25$ reported by the PDG, and taking into account the reconstruction efficiency and the $\eta \to \gamma\gamma$ branching ratio we estimate that this contribution should be negligible. According to the MC simulation this background can be modeled in our data sample with a Gaussian PDF. Despite this contamination is expected to be small, we repeat the fit including an additional peak. The difference in the yield of $\Upsilon(5S) \to \eta\Upsilon(1D)$ events in the two conditions is 0.3%.

As we did for the $\Upsilon(4S) \to \eta h_b(1P)$, we repeat the fit leaving the widths of the signal peaks floating, observing a 6.0% discrepancy in the fitted yields. The same procedure is applied to the peak positions by leaving the $\Upsilon(2S)$ and $\Upsilon(1D)$ masses floating. We observe a discrepancy of 1.7%.

The fit has been repeated using different orders of the Chebyshev polynomial. The corresponding systematic errors are 1% for $\Upsilon(5S) \to \eta\Upsilon(1D), \eta\Upsilon(2S)$, while in the case of $\Upsilon(5S) \to \eta h_b(1,2P)$ and $\Upsilon(5S) \to \eta\Upsilon(1S)$ is of the order of 10%. In the latter case, since no significant signal

---

[1] We cannot explicitly report here the result, which has not been released yet.

is observed, we derive the systematic uncertainty from the fluctuations of the upper limit.

The uncertainties related to the fit procedure are estimated changing both the fit range and the bin width, with the constraint of having a χ^2/NDF comparable to the one obtained in the best conditions. The summary of the systematic errors per each channel are reported in Table 4.3.

Table 4.3: Systematic uncertainties in the study of the $\Upsilon(5S) \to \eta b\bar{b}$ transitions.

Source	$\eta\Upsilon(1S)$	$\eta\Upsilon(2S)$	$\eta\Upsilon(1D)$	$\eta h_b(1P)$	$\eta h_b(2P)$
$N_{\Upsilon(5S)}$	±4.9%	±4.9%	±4.9%	±4.9%	±4.9%
γ reconstruction	±4.0%	±4.0%	±4.0%	±4.0%	±4.0%
Fit range	±4.0%	±6.0%	±3.5%	±9.0%	±10%
Bin width	±7.1%	±1.0%	±3.5%	±15%	±20%
Polynomial order	±9.0%	±7.3%	±1.1%	±10%	±9.0%
Signal resolution	±7.0%	±12%	±1.0%		
Floating masses	±5.0%	±7.2%	±1.7%		
Peaking backgrounds			±0.3%		
Total	±16.2%	±18.1%	±8.3%	±21.0%	±25.0%

4.3.3 Measurement of the $\Upsilon(1D)$ centroid

The fine splitting in the $\Upsilon(1D)$ system is too small to be measured with the recoil mass technique. We can, however, measure the average mass of the system ("centroid" in the following). We obtain the value of $M_{\Upsilon(1D)} = 10161.4 \pm 1.8 \pm 1.0$ MeV/c^2, where the first error is statistical and the second one is systematic. The different sources of systematic uncertainty are reported in Table 4.4. The η meson energy resolution is estimated from the studies conducted on the photon energy scale.

4.3.4 Results

We report the observation of the transition $\Upsilon(5S) \to \eta\Upsilon(1D)$ with statistical significance of 5.3σ, and an evidence of the transition $\Upsilon(5S) \to$

Table 4.4: Systematic uncertainties on the measurement of the $\Upsilon(1D)$ centroid.

Source	Error [MeV]
Fit range	±0.2
Bin width	±0.5
Polynomial order	±0.2
Signal resolution	±0.5
γ energy resolution	±0.7
Total	±1.0

$\eta\Upsilon(2S)$ with statistical significance of 3.3σ. We measure the branching ratios

$$\mathcal{B}[\Upsilon(5S) \to \eta\Upsilon(1D)] = (3.14 \pm 0.63 \pm 0.26) \times 10^{-3}$$

and

$$\mathcal{B}[\Upsilon(5S) \to \eta\Upsilon(2S)] = (1.96 \pm 0.64 \pm 0.35) \times 10^{-3}.$$

Our measurement of $\mathcal{B}[\Upsilon(5S) \to \eta\Upsilon(2S)]$ is about 1.8σ below the result obtained with the exclusive reconstruction of the $\Upsilon(2S)$, $\mathcal{B}[\Upsilon(5S) \to \eta\Upsilon(2S)]_{\Upsilon(2S)\to\pi^+\pi^-\mu^+\mu^-} = (3.8 \pm 0.4 \pm 0.5) \times 10^{-3}$ [129].

In the search for transitions to the $h_b(1,2P)$ no signal has been observed. Upper limits at 90% confidence level are calculated for the branching ratios:

$$\mathcal{B}[\Upsilon(5S) \to \eta h_b(1P)] < 3.4 \times 10^{-3},$$

$$\mathcal{B}[\Upsilon(5S) \to \eta h_b(2P)] < 4.0 \times 10^{-3},$$

and

$\mathcal{B}[\Upsilon(5S) \to \eta\Upsilon(1S)] < 3.1 \times 10^{-3}$,

where the systematic uncertainty is taken into account by lowering the efficiency of a factor $(1 - \sigma_{syst})$.

We also report a new measurement of the average mass of the $\Upsilon(1D)$ triplet,

$M[\Upsilon(1S)] = 10161.4 \pm 1.8 \pm 1.0\ \mathrm{MeV/c^2}$.

Chapter 5

Fit of the $h_b(1P) \to \gamma\eta_b(1S)$ process

5.1 Fitting procedure

The $\Upsilon(4S) \to \eta h_b(1P) \to \eta\gamma\eta_b(1S)$ process is studied using the recoil mass of the η candidate and the observable $\Delta M_{miss} = M_{miss}(\eta\gamma) - M_{miss}(\eta)$, where $M_{miss}(\eta\gamma)$ is the recoil mass of the $\eta\gamma$ pairs, that is expected to peak at the $\eta_b(1S)$ mass value (Figure 5.1). The yield of $h_b(1P)$ is fitted in slices of ΔM_{miss}, and the obtained distribution is then fitted. This procedure is the same used for the first measurement, at Belle, of the $\eta_b(1, 2S)$ parameters [142]. The range in which the $M_{miss}(\eta)$ fit is performed is different from the one used in the previous section in order to assure the proper convergence of the fit in each slice of $\Delta M_{miss}(\eta)$. We select the range [9.8, 9.95] GeV and a 7th order Chebyshev Polynomial for the nominal fit, while alternative ranges and polynomial orders will be used for the estimation of the systematic uncertainties. In order to improve the quality of the fit, we first fit each slice in the sideband sample, where no signal is present, and we use the resulting polynomial coefficients to fix the initial conditions of the fit in the signal sample.

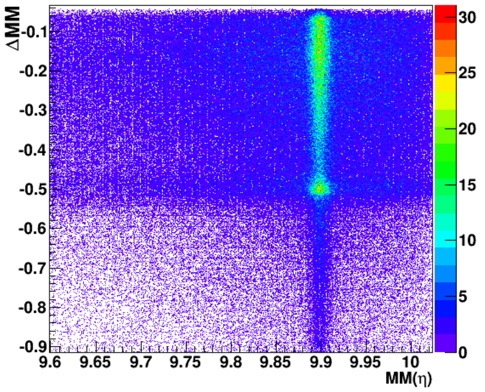

Figure 5.1: ΔM_{miss} versus $M_{miss}(\eta)$ in signal MC events. No MC truth is required.

The signal peak is modeled with the convolution of a resolution function and a Breit-Wigner resonance. The resolution function is modeled as a double Crystal Ball PDF, with a core resolution of 11 MeV, shown in Figure 5.2. The background due to the combination of accidental pho-

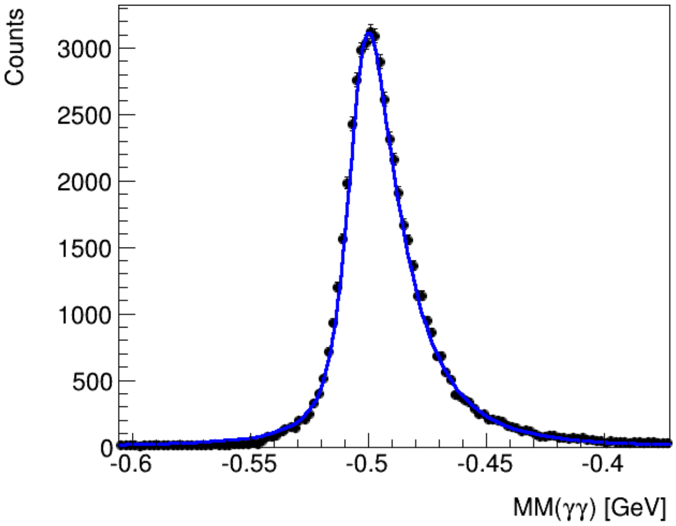

Figure 5.2: Resolution PDF used to model the $\Upsilon(5S) \to \eta h_b(1P) \to \eta\gamma\eta_b(1S)$ signal peak.

tons and a signal η is modeled with an exponential PDF. In the fit of the data sample we fix all the signal parameters except the peak position and the Breit-Wigner width. Given the binned nature of the fit, the possible presence of negative values and the non-poissonian errors, we perform a minimum χ^2 fit.

The fitting procedure is first tested on an MC sample with large signal statistics. The results of the fit, shown in Figure 5.3, are in complete agreement with the MC values.

...

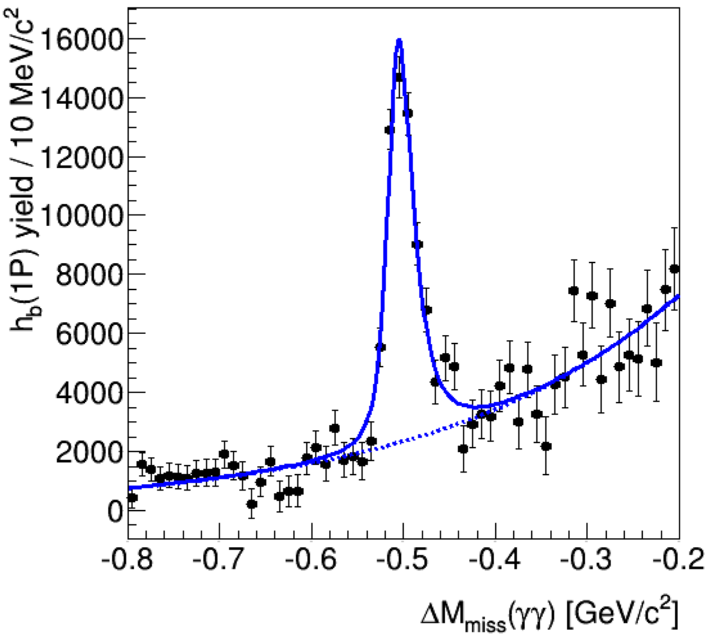

Figure 5.3: $\Upsilon(5S) \rightarrow \eta h_b(1P) \rightarrow \eta\gamma\eta_b(1S)$ signal fit in the MC sample. The background is described with an exponential function.

The branching ratio of the transition $h_b(1P) \rightarrow \gamma\eta_b(1S)$ can be expressed as

$$\mathcal{B}[h_b(1P) \rightarrow \gamma\eta_b(1S)] = \frac{N_{\eta_b(1S)}\epsilon_{\eta h_b(1P)}}{N_{h_b(1P)}\epsilon_{\eta\gamma\eta_b(1S)}},$$

where $\frac{\epsilon_{\eta h_b(1P)}}{\epsilon_{\eta\gamma\eta_b(1S)}} = 1.887 \pm 0.053$ is the ratio of the reconstruction efficiencies for $\Upsilon(4S) \to \eta h_b(1P)$ and $\Upsilon(4S) \to \eta h_b(1P) \to \eta\gamma\eta_b(1S)$.

5.2 Fit of the data sample

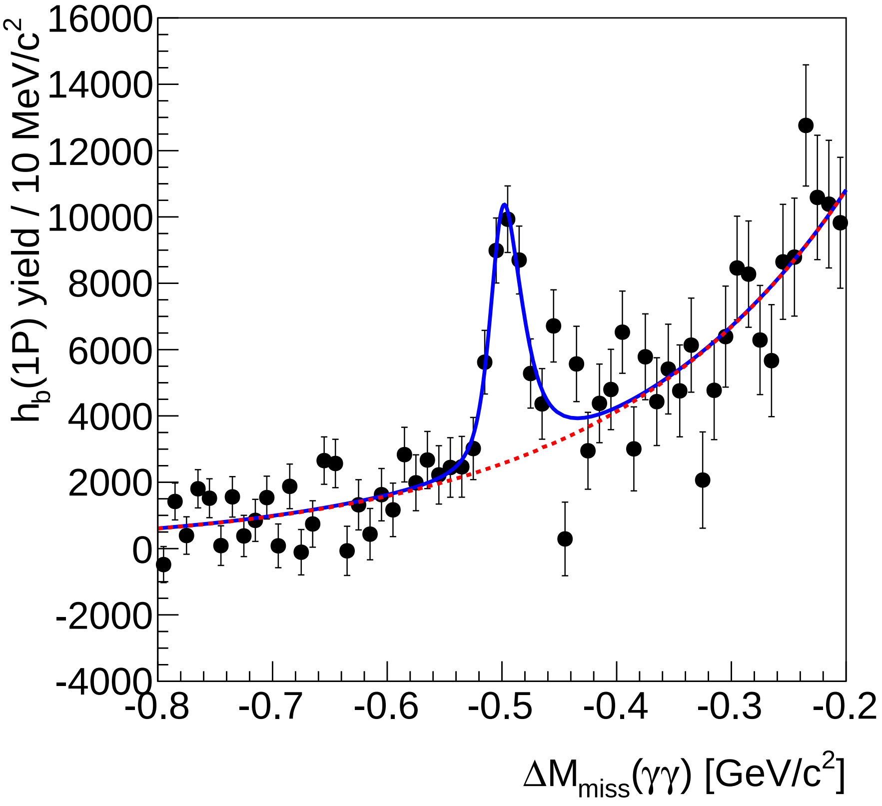

Figure 5.4: $\Upsilon(5S) \to \eta h_b(1P) \to \eta\gamma\eta_b(1S)$ signal fit in the Data sample. The background is described with an exponential function.

We estimate the number of signal events $N_{\eta_b} = 33116 \pm 4741$ and a peak position of:

$\Delta M_{miss} = M_{\eta_b(1S)} - M_{h_b(1P)} = -498.64 \pm 1.74$ (stat) MeV.

The η_b width $\Gamma(\eta_b)$ is left floating in the fit, obtaining the value:

$$\Gamma(\eta_b) = 7.8^{+6.4}_{-5.3} \text{ (stat.) MeV.}$$

. We measure

$$\mathcal{B}[h_b(1P) \to \gamma\eta_b(1S)] = (55.6 \pm 8.0)\%,$$

which is fully compatible with the PDG value $\mathcal{B}^{PDG}[h_b(1P) \to \gamma\eta_b(1S)] = (49 \pm 8)\%$

5.2.1 Systematic errors

The systematic uncertainties related to the η reconstruction and the luminosity do not affect the measurement of $\mathcal{B}[h_b(1P) \to \gamma\eta_b(1S)]$, since it is obtained with a ratio of two branching fractions. The $\gamma\eta_b$ yield is affected by systematic uncertainties from both the ΔM_{miss} fit and the $M_{miss}(\eta)$ fit, but in the determination of the branching fraction some of them simplifies. The contributions due to the different sources are summarized in Table 5.1.

Table 5.1: Systematic uncertainties in the determination of the $\eta_b(1S)$ mass and width, in units of MeV/c^2 and on $\mathcal{B} = \mathcal{B}[h_b(1P) \to \gamma\eta_b(1S)$, in units of %.

Source	ΔM_{miss}	$\Gamma_{\eta_b(1S)}$	$\mathcal{B}$
$M_{\text{miss}}(\eta)$ fit range	±0.8	±3.0	±2.8
$M_{\text{miss}}(\eta)$ bin width	±0.0	±0.1	±0.0
$M_{\text{miss}}(\eta)$ polynomial order	±0.1	±1.9	±1.6
$M_{h_b(1P)}$	±0.0	±0.8	±1.1
ΔM_{miss} fit range	±0.0	±0.7	±2.2
ΔM_{miss} bin width	±0.8	±2.8	±5.2
γ energy calibration	±0.5	±0.3	±1.2
Reconstruction efficiency ratio	-	-	±2.8
Total	±1.2	±4.7	±7.2

Reconstruction efficiency. The uncertainty on the reconstruction efficiency is entirely due to the single photon reconstruction uncertainty, since all the other sources, like the HadronBJ-related one discussed in the previous section, simplify.

γ **energy calibration.** We estimate the impact on the photon calibration uncertainty as we did for the measurements related to the $h_b(1P)$, comparing the results of the analysis obtained under tree different smearing scenarios. For the estimation of the ΔM_{miss}, we include also the contribution due to the uncertainty on β, which is found to be dominant over the uncertainty related to $\mathcal{F}$. For the other measurements, we found no significant effect correlated to the value of β.

$M_{\text{miss}}(\eta)$ **fit.** Four uncertainties are related to the $M_{\text{miss}}(\eta)$ fit: the choice of the bin width, the bin Range, the background PDF order and the value of $M_{h_b(1P)}$, which is fixed during the fit to the value obtained by the fit of the full $M_{miss}(\eta)$ distribution presented in the previous section. In order to assure the uniform quality of the fit, we require the p-value of the ΔM_{miss} fit to be greater than 20%, otherwise the fit configuration will not be included in the estimation of the uncertainties.

The M_{miss} bin width is varied within 0.1 and 0.5 MeV. For each value we repeat the fit procedure, and we report as systematic uncertainty the average fluctuation of the measured quantities. We find that the uncertainties related to the $M_{miss}(\eta)$ binning are almost negligible: we observe $\sigma(\Delta M_{\text{miss}}) = 0.02$ MeV, which can be considered as negligible, $\sigma(\mathcal{B}) = 0.3\%$ and $\sigma(\Gamma_{\eta_b(1S)}) = 0.1$ MeV.

In order to study the effect of the $M_{miss}(\eta)$ range, the lower edge of the fit range is varied from 9.7 to 9.85 GeV in 0.05 GeV steps, while the upper edge is fixed. Extending the upper edge to 10 GeV requires a dramatic change on the background PDF, which is required to have order grater than 11, thus we do not consider this option. We observe the fluctuations $\sigma(\Delta M_{\text{miss}}) = 0.8$ MeV, $\sigma(\Gamma_{\eta_b(1S)}) = 3.0$ MeV and $\sigma(\mathcal{B}) = 2.8\%$.

We test different options for the description of the background, changing the order of the Chebyshev PDF from 5 to 9. We observe the fluctuation on the measured quantities $\sigma(\Delta M_{\text{miss}}) = 0.1$ MeV, $\sigma(\Gamma_{\eta_b(1S)}) = 1.9$ MeV and $\sigma(\mathcal{B}) = 1.6\%$.

The fit of the $M_{\text{miss}}(\eta)$ distributions is performed fixing the position of the $h_b(1P)$ peak to the best fit value of 9899.3 MeV. In the following , we will refer to this parameter as $M^{fit}_{h_b(1P)}$. We repeat the fit with different assumptions for $M^{fit}_{h_b(1P)}$, changing its values within a $\pm 2\sigma$ window around the nominal value with 0.2 MeV steps. We observe a negligible fluctuation of the ΔM_{miss} value of 0.03 MeV, while for the other measured quantities we report $\sigma(\Gamma_{\eta_b(1S)}) = 0.8$ MeV and $\sigma(\mathcal{B}) = 1.1\%$.

ΔM_{miss} fit. We estimate the impact of different ranges in the ΔM_{miss} fit changing the interval lower edge from -0.9 to -0.7 GeV and the upper one within -0.3 GeV and -0.2 GeV. We observe the fluctuations in the measured quantities $\sigma(\Delta M_{\text{miss}}) = 0.1$ MeV, $\sigma(\Gamma_{\eta_b(1S)}) = 1.9$ MeV and $\sigma(\mathcal{B}) = 1.6\%$.

Similarly, we repeat the with with a different bin width: 2, 5, 10 (nominal) and 12 MeV. We observe the fluctuations in the measure quantities $\sigma(\Delta M_{\text{miss}}) = 0.8$ MeV, $\sigma(\Gamma_{\eta_b(1S)}) = 2.8$ MeV and $\sigma(\mathcal{B}) = 5.2\%$.

5.2.2 Results

We observe the transition $\Upsilon(4S) \to \eta h_b(1P) \to \eta\gamma\eta_b(1S)$ with statistical significance of 13σ. We measure the branching fraction

$\mathcal{B}[h_b(1P)\gamma\eta_b(1S)] = (55.6 \pm 8.0 \pm 4.0)\%$,

The mass of the $\eta_b(1S)$ can be calculated by measuring the mass difference

$M_{\eta_b(1S)} - M_{h_b(1P)} = (-498.6 \pm 1.7 \pm 1.2)$ MeV.

We calculate the $\eta_b(1S)$ mass as $M_{\eta_b(1S)} = \Delta M_{miss} + M_{h_b(1P)}$, where $M_{h_b(1P)}$ is the value obtained from the fit of the inclusive $h_b(1P)$ peak:

$M_{\eta_b(1S)} = (9400.7 \pm 1.7 \pm 1.6)$ MeV

Finally we estimate the width of the $\eta_b(1S)$ resonance

$\Gamma_{\eta_b(1S)} = (8^{+6}_{-5} \pm 5)$ MeV.

Chapter 6

Conclusions

This final chapter is devoted to the summary of the results presented in this work and the discussion of their consequences. The most important results are connected with the first observation of the hadronic transition $\Upsilon(4S) \to \eta h_b(1P)$. This process is found to be the strongest known transition from the $\Upsilon(4S)$ meson to lower bottomonium states and offers a completely new pathway to the $\eta_b(1S)$, allowing for the first time to confirm the measurements of the $\eta_b(1S)$ properties previously done by the Belle collaboration exploiting the $\pi\pi$ transitions from the $\Upsilon(5S)$.

At the $\Upsilon(5S)$ energy, we observe for the first time the transition to the $\Upsilon(1D)$ through the emission of an η meson, and we complete the pattern of the searches for η transition. With the available data sample we do not observe transitions to the spin singlet states, but at least we are able to put upper limits that can be compared with the measurements done in the $\pi\pi$ channels.

6.1 Hadronic transitions

A summary of the results of the measurement of hadronic and radiative transitions presented in this work is shown in Table 6.1. We report the first observation of a single meson transition from spin-triplet to spin-singlet bottomonium states, $\Upsilon(4S) \to \eta h_b(1P)$. The search for similar processes resulted in the 90% C.L. upper limits $\mathcal{B}[\Upsilon(4S) \to \eta\Upsilon(1S)] < 2.7 \times 10^{-4}$, in agreement with the measurement by BaBar[128], and $\mathcal{B}[\Upsilon(4S) \to \gamma\gamma\Upsilon(1^3D_{1,2})] \times \mathcal{B}[\Upsilon(1^3D_{1,2}) \to \eta\Upsilon(1S)] < 0.8 \times 10^{-4}$.

Table 6.1: Summary of the results of the searches for η transitions from $\Upsilon(4S)$ and $\Upsilon(5S)$.

Observable	Value	Previous measurement
$\mathcal{B}[\Upsilon(4S) \to \eta h_b(1P)]$	$(2.18 \pm 0.11 \pm 0.18) \times 10^{-3}$	
$\mathcal{B}[\Upsilon(4S) \to \eta\Upsilon(1S)]$	2.7×10^{-4}	$(1.96 \pm 0.28) \times 10^{-4}$
$\mathcal{B}[\Upsilon(5S) \to \eta h_b(2P)]$	$< 4.0 \times 10^{-3}$	
$\mathcal{B}[\Upsilon(5S) \to \eta h_b(1P)]$	$< 3.4 \times 10^{-3}$	
$\mathcal{B}[\Upsilon(5S) \to \eta\Upsilon(2S)]$	$(1.96 \pm 0.64 \pm 0.35) \times 10^{-3}$	$(3.8 \pm 0.4 \pm 0.5) \times 10^{-3}$
$\mathcal{B}[\Upsilon(5S) \to \eta\Upsilon(1S)]$	$< 3.1 \times 10^{-3}$	$(0.73 \pm 0.16 \pm 0.08) \times 10^{-3}$
$\mathcal{B}[\Upsilon(5S) \to \eta\Upsilon(1D)]$	$(3.14 \pm 0.63 \pm 0.26) \times 10^{-3}$	
$\mathcal{B}[h_b(1P) \to \gamma\eta_b(1S)]$	$(56 \pm 8 \pm 4)\%$	$49^{+8}_{-7}\%$

Table 6.2 reports the updated comparison between the theory and the experimental measurement of the η transitions in the bottomonium sector. Our result on $\Upsilon(4S) \to \eta h_b(1P)$ is in remarkable agreement with the theoretical expectation, confirming the validity of the most recent models of

Table 6.2: Theoretical prediction on the partial widths of the η transitions among bottomonium states, from different authors. For the $\Upsilon(5S) \to \Upsilon(2S)$ transition we report both the two the experimental results available. We report here only the theoretical prediction by the authors who considered also the transitions from $\Upsilon(4S)$ and $\Upsilon(5S)$. All the values are in units of keV/c^2

Process	[133]	[135]	[121]	[136]	Exp
$\Upsilon(2S) \to \Upsilon(1S)$ $[\times 10^{-3}]$	60 ± 40				9.3 ± 1.5
$\Upsilon(3S) \to \Upsilon(1S)$ $[\times 10^{-3}]$	3600 ± 2200		20		< 3
$\Upsilon(4S) \to \Upsilon(1S)$	2.3 ± 1.4		6.05		4.0 ± 0.8
$\Upsilon(5S) \to \Upsilon(1S)$	8.8 ± 5.2	$20 - 150$			40 ± 23
$\Upsilon(5S) \to \Upsilon(2S)$		$10 - 100$			209 ± 111, 108 ± 78
$\Upsilon(4S) \to h_b(1P)$			37.9	≈ 20	44.7 ± 7
$\Upsilon(5S) \to h_b(1P)$					< 187
$\Upsilon(5S) \to h_b(2P)$					< 220
$\Upsilon(5S) \to \Upsilon(1D)$					172 ± 96

the light degrees of freedom contributions to these processes. However we must also remark that no author has foreseen the $\Upsilon(5S) \to \eta\Upsilon(1D)$ transition. In this case, the comparison with the $\pi\pi$ transitions is surprising. In the latter, the transition to the $\Upsilon(1D)$ is much weaker than the ones to the $h_b(1P, 2P)$. The measurement of $\Upsilon(5S) \to \pi^+\pi^-\Upsilon(1D)$ has not been explicitly quoted by the previous Belle studies, that only reported the presence of a peak with a yield of 22000 ± 7800 events and 2.4σ of statistical significance. Assuming that the reconstruction efficiency for the $\pi\pi\Upsilon(1D)$ final state is the same as for the nearby transitions, we can approximatively calculate the ratios [1]

$$\frac{\Upsilon(5S) \to \pi^+\pi^-\Upsilon(1D)}{\Upsilon(5S) \to \pi^-\pi^+h_b(1P)} \approx 0.5$$

$$\frac{\Upsilon(5S) \to \pi^+\pi^-\Upsilon(1D)}{\Upsilon(5S) \to \pi^-\pi^+h_b(2P)} \approx 0.3$$

$$\frac{\Upsilon(5S) \to \pi^+\pi^-\Upsilon(1D)}{\Upsilon(5S) \to \pi^-\pi^+\Upsilon(2S)} \approx 0.2$$

In the η transitions sector the situation seems to be opposite. The η transition to the $\Upsilon(1D)$ is larger than or at least of the same order of any other η transition we searched for:

$$\frac{\Upsilon(5S) \to \eta\Upsilon(1D)}{\Upsilon(5S) \to \eta h_b(1P)} > 0.92,$$

$$\frac{\Upsilon(5S) \to \eta\Upsilon(1D)}{\Upsilon(5S) \to \eta h_b(2P)} > 0.78,$$

$$\frac{\Upsilon(5S) \to \eta\Upsilon(1D)}{\Upsilon(5S) \to \eta\Upsilon(2S)} = 1.6 \pm 0.7,$$

This result is even more surprising if we consider that the η transition is selecting only two out of three states of the $\Upsilon(1D)$ spin triplet.

---

[1] These ratios must be taken very carefully. A reasonable assumption for the uncertainty on each is probably ±50%.

None of our results is directly sensitive to the HQSS violation effects, since all the transitions from Υ to h_b are spin-flipping. Furthermore also the calculation of ratios is not possible and only upper or lower limits on $\mathcal{R}_{\eta,\pi\pi}^{nS\to mP}$ can be reported, since we are not able to measure the η transitions from the $\Upsilon(5S)$ to the $h_b(1P,2P)$, for which the $\pi\pi$ counterparts are known, while we measure the transition from the $\Upsilon(4S)$, for which the $\pi\pi$ process has not been studied in details. Belle reported only the upper limit on the ratio of cross sections $\frac{\sigma[e^+e^-\to\pi\pi h_b(1P)]_{\Upsilon(4S)}}{\sigma[e^+e^-\to\pi\pi h_b(1P)]_{\Upsilon(5S)}} < 0.27$. from the computation of the number of $B\bar{B}$ pairs collected by Belle we can calculate $\sigma[e^+e^- \to \Upsilon(4S)] = 1.097$ nb, while the cross section of the $\Upsilon(5S)$ production is $\sigma[e^+e^- \to \Upsilon(5S)] = 0.34$ nb. With these assumption we can evaluate a rough upper limit $\mathcal{B}[\Upsilon(4S) \to \pi^+\pi^- h_b(1S)] < 0.4 \times 10^{-3}$ and us this estimation to calculate the ratio:

$$\mathcal{R}_{\eta,\pi\pi}^{4S\to 1P} > 5.4.$$

For the $\Upsilon(5S)$ we are able to calculate the upper limits

$$\mathcal{R}_{\eta,\pi\pi}^{5S\to 1P} < 0.94$$

and

$$\mathcal{R}_{\eta,\pi\pi}^{5S\to 2P} < 0.62.$$

Unfortunately no theoretical predictions on these ratios are currently available for comparison. The general picture however already shows that the $\Upsilon(4S)$ has a quite unique behavior: it's the only state for which $\mathcal{R}_{\eta,\pi\pi}^{4S\to x} > 1$ in every process studied so far. In the $\Upsilon(5S)$ the data suggest, as general behavior, $\mathcal{R}_{\eta,\pi\pi}^{5S\to x} \approx 1$, while in the narrow bottomonia the HQSS is still a good symmetry with $\mathcal{R}_{\eta,\pi\pi}^{2S,3S\to 1S} << 1$.

6.2 Hyperfine splittings

Table 6.3 summarizes the masses, total widths and hyperfine splittings measured in this work or calculated upon our results.

Table 6.3: Summary of the measurements of different resonance parameters, compared with the values available before our analysis. For the η_b mass and the corresponding hyperfine splitting, we compare our result with the previous one obtained using the E1 transition from $h_b(1P)$

Observable	Value	Previous measurement
$M_{\Upsilon(1D)}$	$(10161 \pm 1.8 \pm 1.0)$ MeV/c^2	10163.7 ± 1.4 MeV/c^2
$M_{h_b(1P)}$	$(9899.3 \pm 0.4 \pm 1.0)$ MeV/c^2	(9899.3 ± 1.0) MeV/c^2
$M_{\eta_b(1S)} - M_{h_b(1P)}$	$(-498.6 \pm 1.7 \pm 1.2)$ MeV/c^2	
$M_{\eta_b(1S)}$	$(9400.7 \pm 1.7 \pm 1.6)$ MeV/c^2	$(9402.4 \pm 1.5 \pm 1.8)$ MeV/c^2
$\Gamma_{\eta_b(1S)}$	$(8^{+6}_{-5} \pm 5)$ MeV/c^2	$(11^{+6}_{-4}$ MeV/c^2
$\Delta M_{\mathrm{HF}}(1S)$	$(+59.6 \pm 1.7 \pm 1.6)$ MeV/c^2	$57.9 \pm 1.5 \pm 1.8$
$\Delta M_{\mathrm{HF}}(1P)$	$(+0.6 \pm 0.4 \pm 1.0)$ MeV/c^2	$(+0.8 \pm 1.1)$ MeV/c^2

In order to calculate $\Delta M_{\mathrm{HF}}(1S)$ we subtract our measurement of $M_{\eta_b(1S)}$ from the world average $\Upsilon(1S)$ mass value $m_{\Upsilon(1S)} = (9460.30 \pm 0.26)$ MeV/c^2. Similarly we calculate $\Delta M_{\mathrm{HF}}(1P)$ subtracting our measurement of the $h_b(1P)$ mass from the world average value of the $\chi_{bJ}(1P)$ centroid, $m^{cog}_{\chi_{bJ}(1P)} = 9899.87 \pm 0.42$. We find $\Delta M_{\mathrm{HF}}(1P) = (+0.6 \pm 0.4 \pm 1.0)$ MeV/c^2, compatible with zero, indicating the absence of significant long-range spin-spin interactions in the QCD potential.

In order to improve our result, we can calculate the average $\eta_b(1S)$ mass accounting for the correlations among our measurement and the previous one obtained by Belle We calculate $M^{avg}_{h_b(1P)}$ as the weighted average of all the available results, including BaBar's one. We assume that no correlation is present among the different measurements, since they are performed at different energies and with different modes: two photons in our case, two charged tracks in the case of the $\Upsilon(5S)$ analysis. The possible sources of correlated uncertainties, like the R_2 selection or the luminosity estimation, do not affect the measurement of $M_{h_b(1P)}$. Table 6.4 shows the measurements and the weights used for this calculation. We observe that the BaBar results has very small impact on the $M^{avg}_{h_b(1P)}$ value, since its error is much larger than the Belle's ones.

Table 6.4: Summary of the measurements contributing to $M^{avg}_{h_b(1P)}$. The weights used in the calculation of the averages are calculated as $w = \sigma_{tot}(M_{h_b(1P)})^{-2}$.

Source	$M_{h_b(1P)}$ [MeV]	$\sigma_{tot}(M_{h_b(1P)})$ [MeV]	weight [MeV^{-2}]
BaBar	9902	4.47	0.05
Belle 5S	9899.1	1.08	0.86
Belle 4S	9899.27	0.98	1.03
Average (including BaBar)	9899.3	0.7	
Average (excluding BaBar)	9899.2	0.7	

We obtain the average value $M^{avg}_{h_b(1P)} = 9899.3 \pm 0.7$ MeV$/c^2$. In order to estimate the average mass of the $\eta_b(1S)$ state we exclude all the measurement obtained using the M1 radiative transitions from $\Upsilon(nS)$ states. These measurements show a systematic disagreement with the one obtained using the E1 transition from the $h_b(1P)$, still subject of theoretical debate. The only measurement that remains is the one obtained by Belle using the transitions $\Upsilon(5S) \to \pi^+\pi^- h_b(1P, 2P) \to \gamma\pi^+\pi^-\eta_b(1S)$. This measurement was obtained using the $M_{h_b(1P)} = (9899.1 \pm 1.08)$ MeV, thus a fist step towards the Belle's average, we re-evaluate $M^{5S}_{\eta_b(1S)}$ assuming the new world average value obtaining:

$$M^{5S,avg}_{\eta_b(1S)} = (9402.6 \pm 1.5 \pm 1.7)\mathrm{MeV}/c^2$$

Similarly we recalculate the $\eta_b(1S)$ mass obtained in our analysis, obtaining

$$M^{4S,avg}_{\eta_b(1S)} = (9400.6 \pm 1.7 \pm 1.4)\mathrm{MeV}/c^2$$

By this means, we have two estimation of $M_{\eta_b(1S)}$, both obtained under the same assumptions for the $h_b(1P)$ mass. However, since $M^{5S,avg}_{\eta_b(1S)}$ relies also on the measurement of the $h_b(2P)$ mass, the correlation coefficient among $M^{5S,\mathrm{avg}}_{\eta_b(1S)}$ and $M^{avg}_{h_b(1P)}$ is 0.805, while it is 1 in the case of $M^{4S,\mathrm{avg}}_{\eta_b(1S)}$. We thus take into account this correlation in the averaging procedure and we obtain the Belle average

$$M^{\mathrm{Belleavg}}_{\eta_b(1S)} = (9401.6 \pm 1.1 \pm 1.2)\mathrm{MeV}/c^2,$$

which is the most precise measurement of the bottomonium ground state mass available.

Our measurement of $\Delta M_{\mathrm{HF}}(1S)$ is in agreement with the value obtained with the $\Upsilon(5S) \to \pi^+\pi^- h_b(1P) \to \pi^+\pi^-\gamma\eta_b(1S)$ process [142], while a discrepancy with the M1-based measurements [153, 154, 152] is present. From the theoretical point of view our result is in agreement with the predictions of many potential models and lattice calculations [**?**], including the most recent ones [**?**], as summarized in Figure 6.1. Our measurement confirms a pattern similar to the one observed in charmonium, suggesting that also in bottomonium the line-shape of the $\eta_b(1S)$ in M1 transition is distorted by a form factor not accounted by the experimental analyses.

Finally, our measurement of $\mathcal{B}[h_b(1P) \to \gamma\eta_b(1S)]$ agrees with the theoretical predictions [**?**, 143].

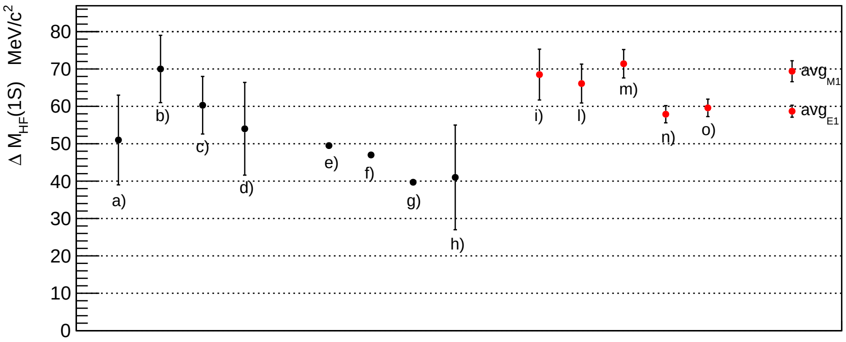

Figure 6.1: Summary of the experimental measurements of the $1S$ hyperfine splitting in bottomonium (red dots), compared with a selection of the most recent theoretical predictions (black dots).
The theoretical prediction are: a) Aarts et al. (2014) [144], b) Dowdall et al. (2012) [145], c) Meinel (2012) [146], d) Burch et al. (2010) [147], e) Wei-Zhao et al. (2013) [148], f) Gupta et al. (1994) [149], g) Radford and Repko (2007) [150], h) Kniehl et al. (2004) [151].
The experimental measurements are: i) CLEO collaboration (M1 transition $\Upsilon(3S) \rightarrow \gamma\eta_b(1S)$) [152], l) BaBar Collaboration (M1 transition $\Upsilon(3S) \rightarrow \gamma\eta_b(1S)$) [153], m) BaBar Collaboration (M1 transition $\Upsilon(2S) \rightarrow \gamma\eta_b(1S)$) [154], n) Belle Collaboration (E1 transitions $h_b(1P, 2P) \rightarrow \gamma\eta_b(1S)$) [142].
The last point are the average of the $M1$ and $E1$ measurements. For the $E1$ value we use the Belle internal average.

Appendices

Appendix A

Improved π^0 and η selection

Despite the success of this very simple vetoing algorithm we wish to highlight that other possible definition of $\mathcal{D}$ were tested and, despite they turn out not to improve significantly the quality of the veto, can still be used for future analysis which require an high purity π^0 samples or for the implementation of more complex veto algorithms. In particular we focus your attention on the angular distribution and the momentum spectrum of real an fake π^0 candidates. First, we notice that the real π^0 and the combinatorial background have a quite different momentum spectrum, and significant differences are observed also in the angular distribution at $\cos\theta_{\gamma\gamma} \approx 1$ (Figure A.1).

Based on this considerations, we tested an alternative definition of $\mathcal{D}$ as

$$\mathcal{D} = \mathcal{P}_{\pi^0}(p, M),$$

where $\mathcal{P}$ is the probability, evaluated thanks to the montecarlo simulation, for a $\gamma\gamma$ pair of momentum p and mass m to be a real π^0 rather than a combinatorial pair. We do not include the angular distribution information in the construction of the $\mathcal{D}$ function since its discriminating power is found to be too low. To estimate the probability distribution $\mathcal{P}_{\pi^0}(p, M)$, we

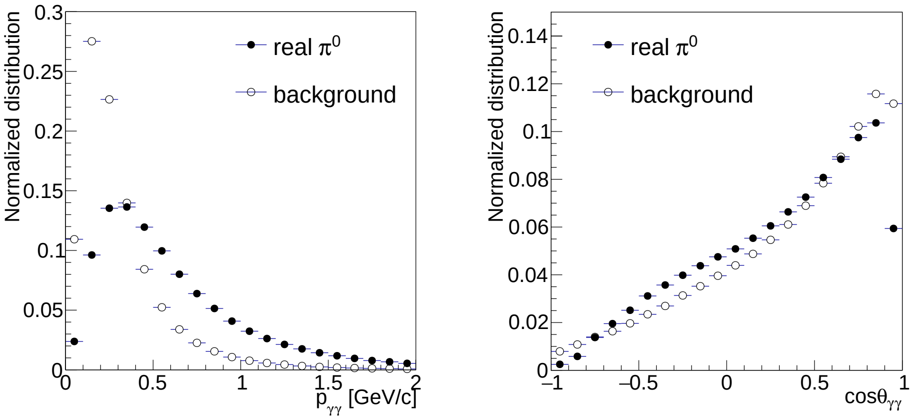

Figure A.1: *Left*: Momentum spectrum of real and fake π^0 in the π^0 mass window. *Right*: Angular distribution of real and fake π^0 in the π^0 mass window.

take the ratio between the real π^0 and the total number of $\gamma\gamma$ candidates in 140 mass bins between 0.10 and 0.17 Gev$/c^2$ and 300 momentum bins between 0 and 3 GeV$/c$. We find that the maximum signal/background ratio is obtained requiring $\mathcal{P}_{\pi^0} > 0.27$, as shown in Figure A.2. Therefore,

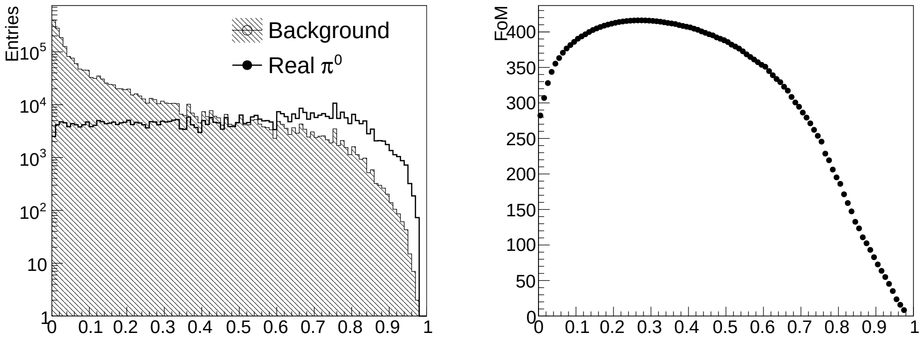

Figure A.2: *Left*: Distribution of $\mathcal{P}_{\pi^0}$ for real π^0 and combinatorial background. *Right*: Figure of merit of the optimization of the $\mathcal{P}_{\pi^0}$ cut.

we tried to implement a π^0 veto based on $\mathcal{P}_{\pi^0}$ selecting as π^0 candidates the $\gamma\gamma$ pair with $\mathcal{P}_{\pi^0} > 0.27$ and subsequently ordering them according to the decreasing values of $\mathcal{P}_{\pi^0}$. The comparison among between the two different definitions of $\mathcal{D}$ are shown in Figure A.3

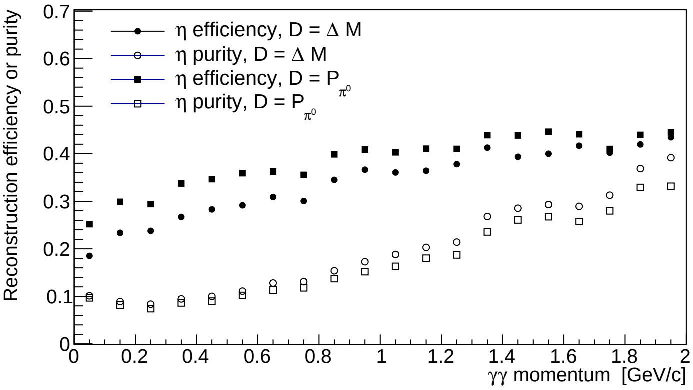

Figure A.3: Comparison between the η reconstruction efficiency and the η purity obtained using different definitions of the π^0 veto function $\mathcal{D}$.

Even if $\mathcal{D} = \mathcal{P}_{\pi^0}$ allows a slightly higher reconstruction efficiency in the low momentum region, the signal purity is slightly decreased. Furthermore, we notice that the choice of $\mathcal{D} = \mathcal{P}_{\pi^0}$ is likely to introduce much larger systematic uncertainties. Large fluctuations of the veto performances are observed if the binning used for the construction of $\mathcal{P}$ is changed. Furthermore the value of the probability strongly depends on the MC simulation of the π^0 spectrum and yield, which is controlled at few % level, while in the case of $\mathcal{D} = \Delta M$ the only systematic uncertainty is introduced by the modeling of the π^0 mass peak, which has been corrected by the photon energy calibration and whose effect on the veto efficiency is controlled at the 0.1% level. Therefore, we decided to avoid using the improved definition of $\mathcal{P}$, even if we suggest further investigation of this variable for future analysis.

Similarly, $\mathcal{P}$ could be used instead of the mass window to define good π^0 and good η to be used in the analysis. Also in this case, the same considerations made on the large systematic uncertainty made us decide not to use it an to opt for a much simpler definition. However, we report here the performances we obtained, and again we suggest that this method could be used in analysis that require the selection of high momentum π^0 or η, or that are not based on the analysis of the recoil mass spectrum. In both the π^0 (Figure A.4) and the η case (Figure A.5), we observe that the selection based on $\mathcal{P}$ increases the sample purity in the low momentum region, but decreasing by a significant amount the reconstruction efficiency. This effect is primary due to the strong correlation among $\mathcal{P}$ and the $\gamma\gamma$ momentum.

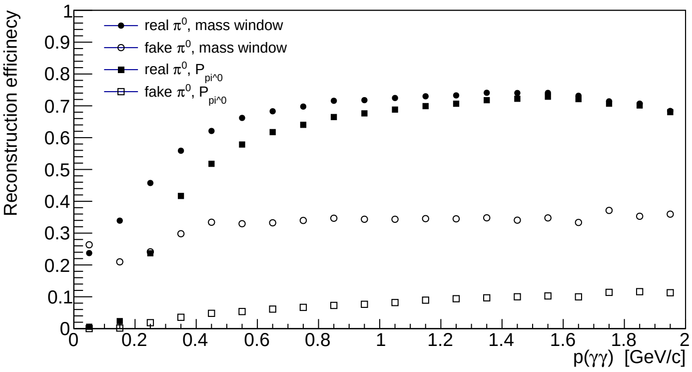

Figure A.4: Comparison between the π^0 reconstruction efficiency and the π^0 purity obtained using different signal selection criteria

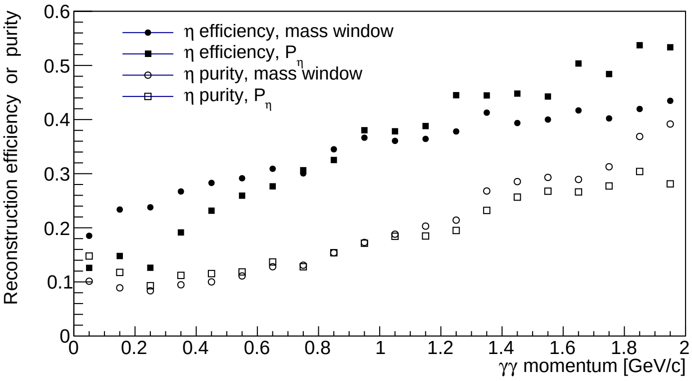

Figure A.5: Comparison between the η reconstruction efficiency and the η purity obtained using different signal selection criteria

Appendix B

Prospects for an improved continuum rejection

The rejection of the continuum has been never deeply studied for bottomonium physics inside the Belle Collaboration. This issue is indeed a central problem only for the $\Upsilon(4S)$ and $\Upsilon(5S)$ samples, which showed their rich potential for bottomonium physics only very recently with large di-pion transition that did appeared prominently even with a simple R_2-based selection. The bulk of the samples collected for bottomonium studies by Belle are at $\Upsilon(1S)$ and $\Upsilon(2S)$ energies, where the continuum contribution is much smaller than the resonant one. Therefore few studies have been done on this problem, which revived little attention in the past years inside the collaboration.

To try to fill this gap we made a first pilot study following the same approach used for the B-meson analyses, combining different event-shape observable in one single Fisher discriminant to improve the continuum rejection. We compared the separation power archived with different observables and different combinations, using both single observables and Fisher discriminants obtained by different combinations. The study is performed using an MC sample of continuum events and one of $\Upsilon(1S)$

annihilation, both at the same energy in the CM frame. We will consider 14 observables: the sphericity S and the thrustness T (Figure B.1), the fox-wolfram ratios $R_n$of oder from 1 to 4 (Figure B.2 and B.3), the multipole moments M_l^z of order 1 to 4 calculated with respect to the beam axis (Figure B.4 and B.5, and the multipole moments M_l^t of order 1 to 4 calculated with respect to the thrust axis (Figure B.6 and B.7. In order to discriminate

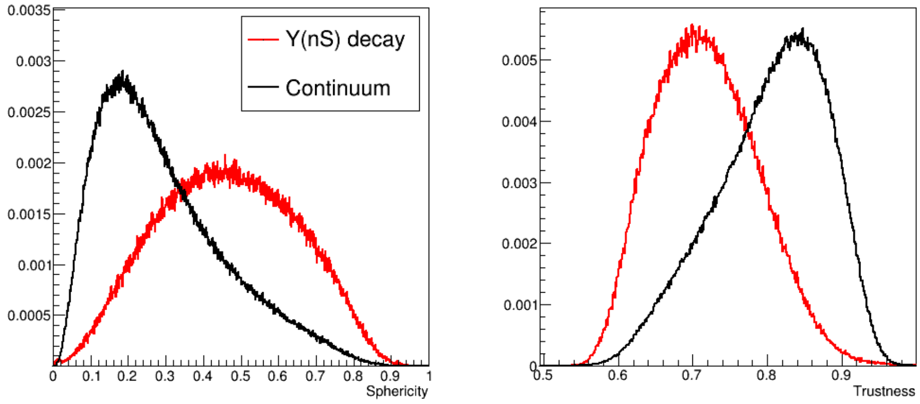

Figure B.1: *Left*: Sphericity S for jet-like and spherical events *Right*: Thrust T for jet-like and spherical events.

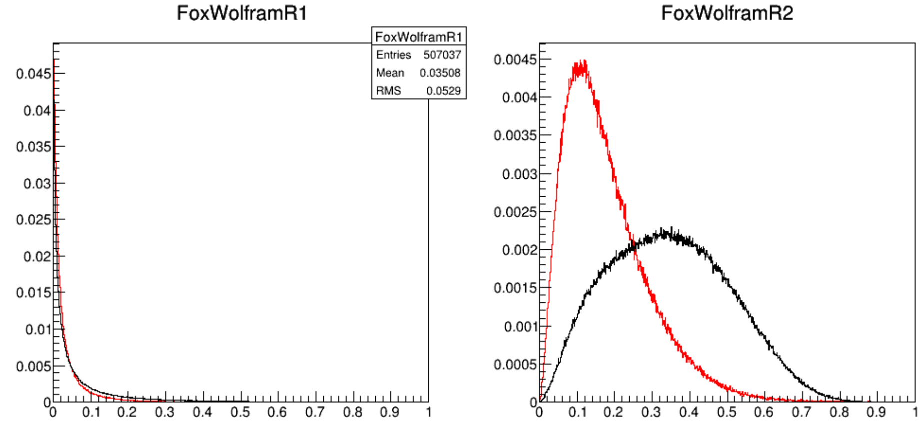

Figure B.2: *Left*: $R1$ Fox-Wolfram momentum for jet-like and spherical events *Right*: $R2$ Fox-Wolfram momentum for jet-like and spherical events.

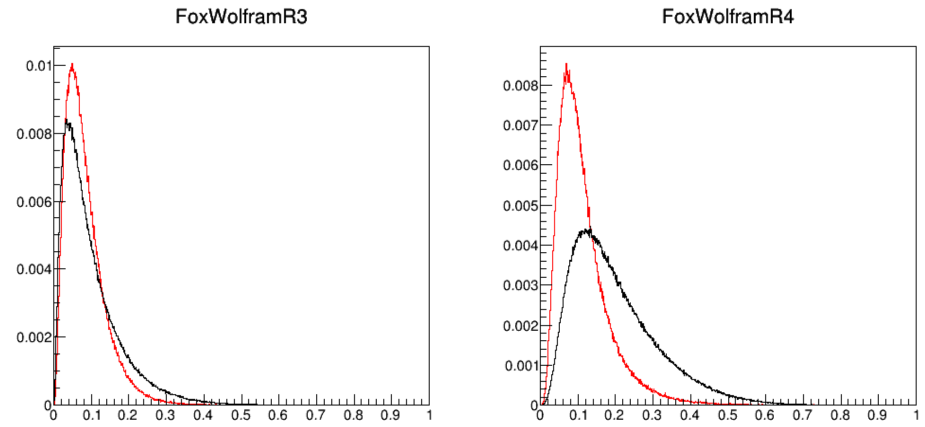

Figure B.3: *Left*: $R3$ Fox-Wolfram momentum for jet-like and spherical events *Right*: $R4$ Fox-Wolfram momentum for jet-like and spherical events.

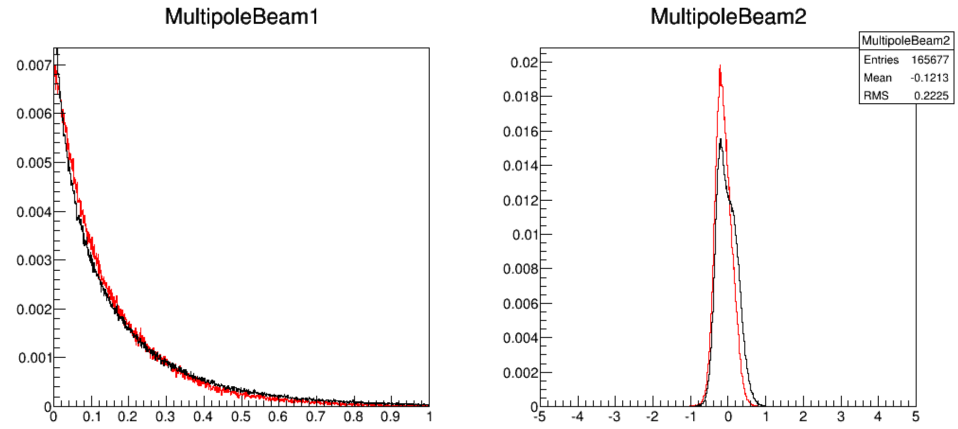

Figure B.4: *Left*: M_1^z multipole moment for jet-like and spherical events *Right*: M_2^z multipole moment for jet-like and spherical events.

between different combinations an determine what is the best strategy for the continuum rejection we define the *discriminating power* p of an event shape variable (or their combination) x as

$$p(x) = \frac{| < x_{\Upsilon} > - < x_{q\bar{q}} > |}{\sqrt{\sigma^2_{x_{\Upsilon}} + \sigma^2_{x_{q\bar{q}}}}},$$

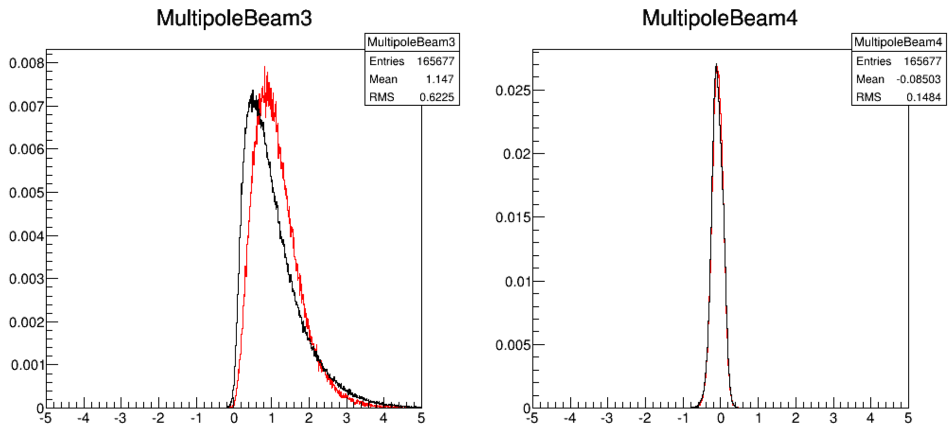

Figure B.5: *Left*: M_3^z multipole moment for jet-like and spherical events *Right*: M_3^z multipole moment for jet-like and spherical events.

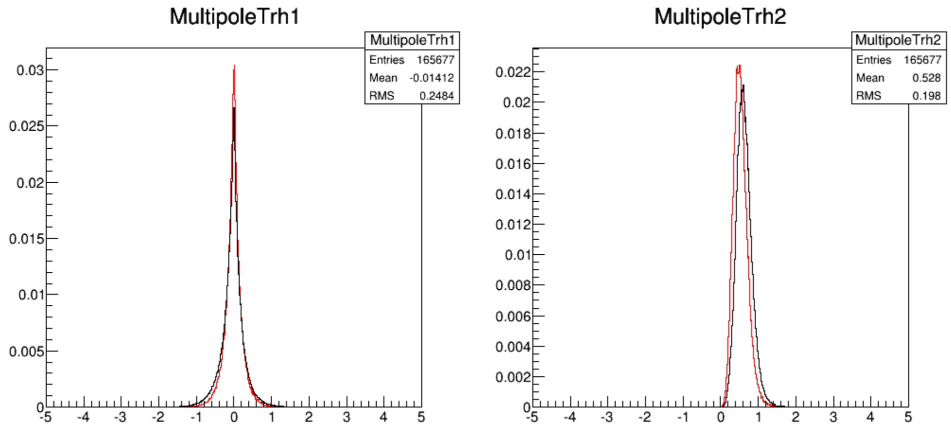

Figure B.6: *Left*: M_1^t multipole moment for jet-like and spherical events *Right*: M_2^t multipole moment for jet-like and spherical events.

where $< x >$ is the average value of x in each sample and σ^2 is its variance [1].

As it appears immediately from the distributions, not all the variables we use have the same discriminating power, as reporter in Figure B.8. The

---

[1] In general these observables are not Gaussian, therefore σ^2 should not be interpreted as the width of a peak and, in general, $< x >$ do not correspond to the maximum of the probability distribution.

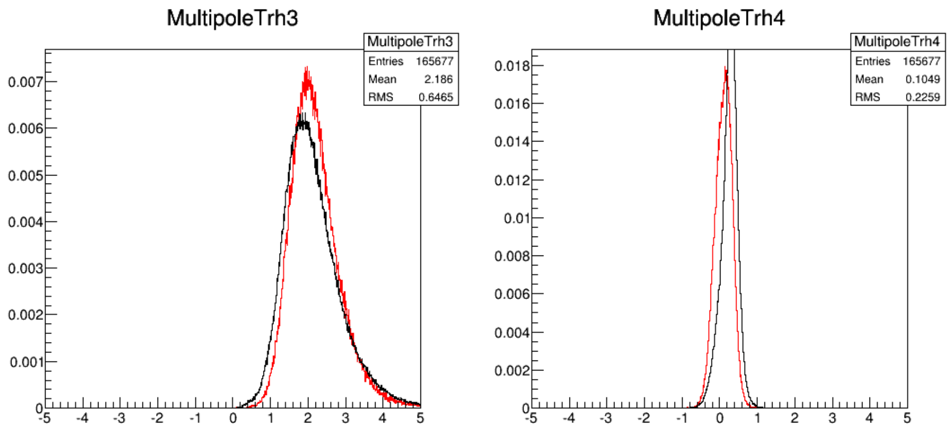

Figure B.7: *Left*: M_3^t multipole moment for jet-like and spherical events *Right*: M_4^t multipole moment for jet-like and spherical events.

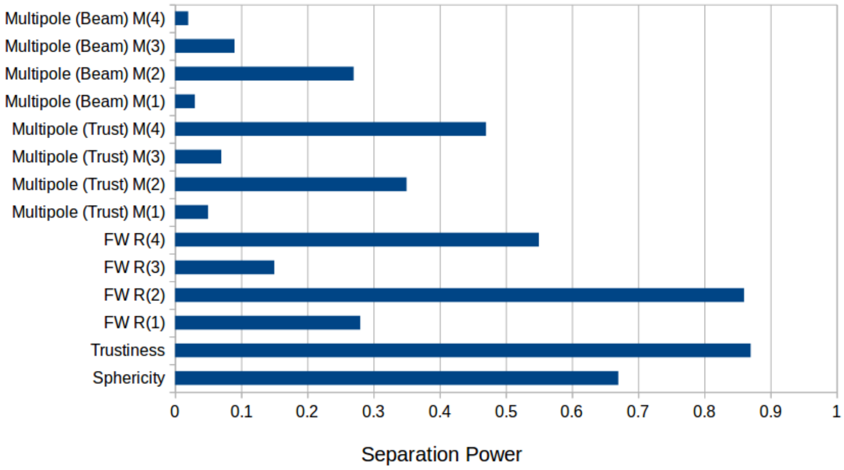

Figure B.8: Separation power of different event-shape observable.

$R2$ moment, the sphericity S and the thrustness T grants the hist separation power, but are also strongly correlated one with the other as shown in Figure B.9. Indeed, they all carry the same underlying information and it is even possible to obtain analytically one from the other. The separation power is useful to understand which variables can be useful and which are not, but nevertheless it is not directly connected with the improvement of the signal significances. Since the distributions are neither Gaussian

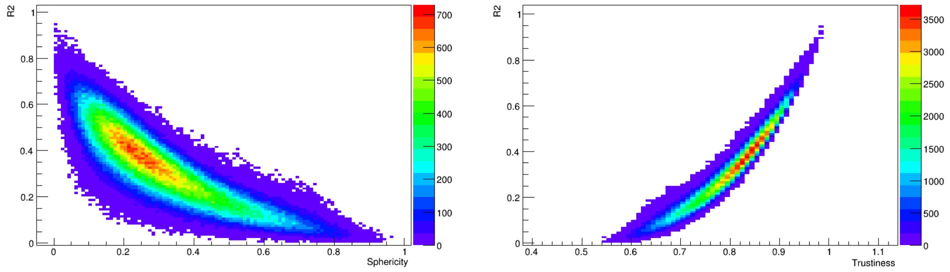

Figure B.9: *Left*: Correlation between S and R_2 in spherical events *Right*: Correlation between T and R_2 in spherical events.

nor even symmetric, variables with lower discriminating power can allow a larger increase o the signal over background ratio after the optimization procedure. Therefore, in order to test the fisher discriminants we will construct, we will use the signal over background ration rather than the separation power as defined above. For this analysis, we consider as *signal* the spherical events and as *background* the jet-like ones, therefore the significance should not be interpreted directly as significance of the η recoil mass peaks. In the light of the results of the analysis of the separating power, we decided not to use for the calculation of the Fisher discriminant the multipole moments M^z_i. Among the remaining combinations, we tested the most promising ones: $(R_1 ... R_4)$, $(M^t_1 ... M^t_4)$ and $(R_1 ... R_4, M^t_{2,4})$, where $M^t_{1,3}$ are excluded since they are carrying a very low separation power. In order to test the construction of the discriminant against over-training and to proof its capability to handle the correlations among observables we also tested the combinations (R_2, S) and (R_2, T), which are expected to give results comparable to the one obtained with the most powerful observable in the pair, i.e. R_2. Finally, as reference, we study the result of the optimization made using R_2, S and T separately. Figure **??** presents the signal over background ratio obtained optimizing the continuum rejection cut on different observables, normalized to the value obtained if no selection is applied.

From the analysis of the signal significance increase, we can deduce many characteristics of the event shape observables we used. Clearly the sphericity is the less powerful among the single observables, while R_2 and T are behaving similarly. The Fisher discriminant is able to correctly handle the correlations, since the results obtained with (R_2, S) and (R_2, T) are identical to the result obtained with R_2 only. Despite non of the M_i^z variable has separating power comparable to R_2, their combination allows to reach a similar level of significance. Finally a good improvement is archived if the four Fox-Wolfram moments are combined together, while the further addition of $M_{2,4}^t$ is not increasing the significance, indicating that these two observables are strongly correlated with R_i.

From this analysis we would conclude that the best strategy is to use the Fisher discriminant obtained by the combination $(R_1 ... R_4$, shown in Figure **??** instead of the traditional R_2 only. However, the increased signal significance is obtained with a significant reduction of the selection efficiency, as reported in Table **??**. Since one our main goal is to measure with high statistics the $h_b(1P)$ and the $\eta_b(1S)$ masses, a high selection efficiency is required, while background levels even rather high are not limiting the precision of the measurements, assuming that the recoil peaks are observed with reasonable significance. Furthermore a major limiting factor to the application of the Fisher discriminant technique is again represented by the mis-modeling in the MC simulation. The combination of more FW moments increases significantly the impact of the MC simula-

Table B.1: Reconstruction efficiency and MM(η) resolution in MC. The peak position corresponds to the fitted recoil mass in MC events.

Method	Signal efficiency [%]	Background efficiency [%]
R_2	66.4	21.7
$R_1 ... R_4$	39.5	8.7

tion quality on the matching with the data. After consultations withing the $\Upsilon(5S)$ working group and in the light of these reasons, we finally opted for a more conservative approach, basing our continuum rejection on R_2 only. However we wish here to point out that the combination of different events shape observables, combined with a better tuning of the MC simulation, is definitively more promising than the selection based on R_2 only.

Bibliography

[1] A. J. Bevan *et al.* [BaBar and Belle Collaborations], Eur. Phys. J. C **74** (2014) 3026 doi:10.1140/epjc/s10052-014-3026-9 [arXiv:1406.6311 [hep-ex]].

[2] S. Kurokawa, E. Kikutani, Nucl. Instrum. Meth. A **499**, 1 (2003). and other papers included in this volume.

[3] W. Kozanecki, Nucl. Instrum. Meth. A **446**, 59 (2000). doi:10.1016/S0168-9002(00)00022-X

[4] P. Krizan *et al.* [HERA-B Collaboration], Nucl. Instrum. Meth. A **351**, 111 (1994). doi:10.1016/0168-9002(94)91071-5

[5] A. A. Alves, Jr. *et al.* [LHCb Collaboration], JINST **3**, S08005 (2008). doi:10.1088/1748-0221/3/08/S08005

[6] J. H. Christenson, J. W. Cronin, V. L. Fitch and R. Turlay, Phys. Rev. Lett. **13**, 138 (1964). doi:10.1103/PhysRevLett.13.138

[7] N. Cabibbo, Phys. Rev. Lett. **10**, 531 (1963). doi:10.1103/PhysRevLett.10.531

[8] M. Kobayashi and T. Maskawa, Prog. Theor. Phys. **49**, 652 (1973). doi:10.1143/PTP.49.652

[9] L. Wolfenstein, Phys. Rev. Lett. **51**, 1945 (1983). doi:10.1103/PhysRevLett.51.1945

[10] J. Brodzicka *et al.* [Belle Collaboration], PTEP **2012**, 04D001 (2012) doi:10.1093/ptep/pts072 [arXiv:1212.5342 [hep-ex]].

[11] T. Abe *et al.*, PTEP **2013**, 03A001 (2013). doi:10.1093/ptep/pts102

[12] K. Kanazawa *et al.*, Nucl. Instrum. Meth. A **499**, 75 (2003). doi:10.1016/S0168-9002(02)01784-9

[13] T. Abe *et al.*, Conf. Proc. C **070625**, 27 (2007) [arXiv:0706.3248 [physics.ins-det]].

[14] A. Abashian *et al.*, Nucl. Instrum. Meth. A **479**, 117 (2002). doi:10.1016/S0168-9002(01)02013-7

[15] N. Brambilla *et al.*, Eur. Phys. J. C **74**, no. 10, 2981 (2014) doi:10.1140/epjc/s10052-014-2981-5 [arXiv:1404.3723 [hep-ph]].

[16] N. Brambilla *et al.* [Quarkonium Working Group Collaboration], hep-ph/0412158.

[17] N. Brambilla *et al.*, Eur. Phys. J. C **71**, 1534 (2011) doi:10.1140/epjc/s10052-010-1534-9 [arXiv:1010.5827 [hep-ph]].

[18] M. Gell-Mann, Phys. Lett. **8**, 214 (1964). doi:10.1016/S0031-9163(64)92001-3

[19] G. Zweig, CERN-TH-401.

[20] G. Zweig, Developments in the Quark Theory of Hadrons, Volume 1. Edited by D. Lichtenberg and S. Rosen. pp. 22-101

[21] F. Wilczek, Phys. Today **53N8**, 22 (2000). doi:10.1063/1.1310117

[22] J. D. Bjorken and E. A. Paschos, Phys. Rev. **185**, 1975 (1969). doi:10.1103/PhysRev.185.1975

[23] D. J. Gross and F. Wilczek, Phys. Rev. Lett. **30**, 1343 (1973). doi:10.1103/PhysRevLett.30.1343

[24] H. D. Politzer, Phys. Rev. Lett. **30**, 1346 (1973). doi:10.1103/PhysRevLett.30.1346

[25] D. J. Gross, In *Stanford 1992, The rise of the standard model* 199-232 [hep-ph/9210207].

[26] R. L. Jaffe, Phys. Rev. D **15**, 281 (1977). doi:10.1103/PhysRevD.15.281

[27] G. S. Bali, hep-ph/9809351.

[28] M. N. Chernodub, arXiv:1001.0570 [hep-ph].

[29] E. Witten, Nucl. Phys. B **223**, 433 (1983). doi:10.1016/0550-3213(83)90064-0

[30] A. Casher, H. Neuberger and S. Nussinov, Phys. Rev. D **20**, 179 (1979). doi:10.1103/PhysRevD.20.179

[31] J. E. Augustin *et al.* [SLAC-SP-017 Collaboration], Phys. Rev. Lett. **33**, 1406 (1974) [Adv. Exp. Phys. **5**, 141 (1976)]. doi:10.1103/PhysRevLett.33.1406

[32] J. J. Aubert *et al.* [E598 Collaboration], Phys. Rev. Lett. **33**, 1404 (1974). doi:10.1103/PhysRevLett.33.1404

[33] G. S. Abrams *et al.*, Phys. Rev. Lett. **33**, 1453 (1974) [Adv. Exp. Phys. **5**, 150 (1976)]. doi:10.1103/PhysRevLett.33.1453

[34] S. W. Herb *et al.*, Phys. Rev. Lett. **39**, 252 (1977). doi:10.1103/PhysRevLett.39.252

[35] A. De Rujula and S. L. Glashow, Phys. Rev. Lett. **34**, 46 (1975). doi:10.1103/PhysRevLett.34.46

[36] E. Eichten, S. Godfrey, H. Mahlke and J. L. Rosner, Rev. Mod. Phys. **80**, 1161 (2008) doi:10.1103/RevModPhys.80.1161 [hep-ph/0701208].

[37] E. Eichten, K. Gottfried, T. Kinoshita, K. D. Lane and T. M. Yan, Phys. Rev. D **17**, 3090 (1978) [Phys. Rev. D **21**, 313 (1980)]. doi:10.1103/PhysRevD.17.3090, 10.1103/PhysRevD.21.313

[38] C. Quigg and J. L. Rosner, Phys. Lett. B **71**, 153 (1977). doi:10.1016/0370-2693(77)90765-1

[39] C. Quigg, AIP Conf. Proc. **424**, 173 (1998) doi:10.1063/1.55117 [hep-ph/9707493].

[40] M. B. Voloshin, Prog. Part. Nucl. Phys. **61**, 455 (2008) doi:10.1016/j.ppnp.2008.02.001 [arXiv:0711.4556 [hep-ph]].

[41] J. Pumplin, W. Repko and A. Sato, Phys. Rev. Lett. **35**, 1538 (1975). doi:10.1103/PhysRevLett.35.1538

[42] D. Ebert, R. N. Faustov and V. O. Galkin, Phys. Rev. D **67**, 014027 (2003) doi:10.1103/PhysRevD.67.014027 [hep-ph/0210381].

[43] W. Buchmuller, Y. J. Ng and S. H. H. Tye, Phys. Rev. D **24**, 3003 (1981). doi:10.1103/PhysRevD.24.3003

[44] A. M. Badalian, A. I. Veselov and B. L. G. Bakker, Phys. Rev. D **70**, 016007 (2004). doi:10.1103/PhysRevD.70.016007

[45] J. N. Pandya, A. K. Rai and P. C. Vinodkumar, Frascati Phys. Ser. **46**, 1519 (2007) [arXiv:0808.1077 [hep-ph]].

[46] S. Okubo, Phys. Lett. **5**, 165 (1963). doi:10.1016/S0375-9601(63)92548-9

[47] J. Iizuka, Prog. Theor. Phys. Suppl. **37**, 21 (1966). doi:10.1143/PTPS.37.21

[48] H. Severini *et al.* [CLEO Collaboration], Phys. Rev. Lett. **92**, 222002 (2004) doi:10.1103/PhysRevLett.92.222002 [hep-ex/0307034].

[49] X. H. He *et al.* [Belle Collaboration], Phys. Rev. Lett. **113**, no. 14, 142001 (2014) doi:10.1103/PhysRevLett.113.142001 [arXiv:1408.0504 [hep-ex]].

[50] W. E. Caswell and G. P. Lepage, Phys. Lett. B **167**, 437 (1986). doi:10.1016/0370-2693(86)91297-9

[51] U. Van Kolck, L. J. Abu-Raddad and D. M. Cardamone, AIP Conf. Proc. **631**, 191 (2002) doi:10.1063/1.1513681 [nucl-th/0205058].

[52] N. Brambilla, A. Pineda, J. Soto and A. Vairo, Rev. Mod. Phys. **77**, 1423 (2005) doi:10.1103/RevModPhys.77.1423 [hep-ph/0410047].

[53] G. P. Lepage, L. Magnea, C. Nakhleh, U. Magnea and K. Hornbostel, Phys. Rev. D **46**, 4052 (1992) doi:10.1103/PhysRevD.46.4052 [hep-lat/9205007].

[54] J. Soto, Eur. Phys. J. A **31**, 705 (2007) doi:10.1140/epja/i2006-10255-9 [nucl-th/0611055].

[55] A. Pineda and J. Soto, Nucl. Phys. Proc. Suppl. **64** (1998) 428 doi:10.1016/S0920-5632(97)01102-X [hep-ph/9707481].

[56] N. Brambilla, A. Pineda, J. Soto and A. Vairo, Nucl. Phys. B **566**, 275 (2000) doi:10.1016/S0550-3213(99)00693-8 [hep-ph/9907240].

[57] G. S. Bali *et al.* [UKQCD Collaboration], Phys. Lett. B **309**, 378 (1993) doi:10.1016/0370-2693(93)90948-H [hep-lat/9304012].

[58] M. Luscher, Phys. Lett. B **118**, 391 (1982). doi:10.1016/0370-2693(82)90210-6

[59] M. Luscher, Commun. Math. Phys. **104**, 177 (1986). doi:10.1007/BF01211589

[60] M. Luscher, Commun. Math. Phys. **105**, 153 (1986). doi:10.1007/BF01211097

[61] G. P. Lepage and B. A. Thacker, Nucl. Phys. Proc. Suppl. **4**, 199 (1988). doi:10.1016/0920-5632(88)90102-8

[62] B. A. Thacker and G. P. Lepage, Phys. Rev. D **43**, 196 (1991). doi:10.1103/PhysRevD.43.196

[63] H. D. Trottier, Phys. Rev. D **55** (1997) 6844 doi:10.1103/PhysRevD.55.6844 [hep-lat/9611026].

[64] N. A. Tornqvist, Phys. Rev. Lett. **53**, 878 (1984). doi:10.1103/PhysRevLett.53.878

[65] N. A. Tornqvist, Acta Phys. Polon. B **16**, 503 (1985) [Acta Phys. Polon. B **16**, 683 (1985)].

[66] J. F. Liu and G. J. Ding, Eur. Phys. J. C **72**, 1981 (2012) doi:10.1140/epjc/s10052-012-1981-6 [arXiv:1105.0855 [hep-ph]].

[67] P. Moxhay, Phys. Rev. D **39**, 3497 (1989). doi:10.1103/PhysRevD.39.3497

[68] H. Y. Zhou and Y. P. Kuang, Phys. Rev. D **44**, 756 (1991). doi:10.1103/PhysRevD.44.756

[69] E. Klempt and A. Zaitsev, Phys. Rept. **454**, 1 (2007) doi:10.1016/j.physrep.2007.07.006 [arXiv:0708.4016 [hep-ph]].

[70] S. K. Choi *et al.* [Belle Collaboration], Phys. Rev. Lett. **91**, 262001 (2003) doi:10.1103/PhysRevLett.91.262001 [hep-ex/0309032].

[71] D. Acosta *et al.* [CDF Collaboration], Phys. Rev. Lett. **93**, 072001 (2004) doi:10.1103/PhysRevLett.93.072001 [hep-ex/0312021].

[72] V. M. Abazov *et al.* [D0 Collaboration], Phys. Rev. Lett. **93**, 162002 (2004) doi:10.1103/PhysRevLett.93.162002 [hep-ex/0405004].

[73] B. Aubert *et al.* [BaBar Collaboration], Phys. Rev. D **71**, 071103 (2005) doi:10.1103/PhysRevD.71.071103 [hep-ex/0406022].

[74] B. Aubert *et al.* [BaBar Collaboration], Phys. Rev. Lett. **102**, 132001 (2009) doi:10.1103/PhysRevLett.102.132001 [arXiv:0809.0042 [hep-ex]].

[75] P. del Amo Sanchez *et al.* [BaBar Collaboration], Phys. Rev. D **82**, 011101 (2010) doi:10.1103/PhysRevD.82.011101 [arXiv:1005.5190 [hep-ex]].

[76] V. Bhardwaj *et al.* [Belle Collaboration], Phys. Rev. Lett. **107**, 091803 (2011) doi:10.1103/PhysRevLett.107.091803 [arXiv:1105.0177 [hep-ex]].

[77] S. K. Choi *et al.* [Belle Collaboration], Phys. Rev. Lett. **100**, 142001 (2008) doi:10.1103/PhysRevLett.100.142001 [arXiv:0708.1790 [hep-ex]].

[78] R. Mizuk *et al.* [Belle Collaboration], Phys. Rev. D **80**, 031104 (2009) doi:10.1103/PhysRevD.80.031104 [arXiv:0905.2869 [hep-ex]].

[79] K. Chilikin *et al.* [Belle Collaboration], Phys. Rev. D **88**, no. 7, 074026 (2013) doi:10.1103/PhysRevD.88.074026 [arXiv:1306.4894 [hep-ex]].

[80] B. Aubert *et al.* [BaBar Collaboration], Phys. Rev. D **79**, 112001 (2009) doi:10.1103/PhysRevD.79.112001 [arXiv:0811.0564 [hep-ex]].

[81] K. F. Chen *et al.* [Belle Collaboration], Phys. Rev. Lett. **100**, 112001 (2008) doi:10.1103/PhysRevLett.100.112001 [arXiv:0710.2577 [hep-ex]].

[82] A. Bondar *et al.* [Belle Collaboration], Phys. Rev. Lett. **108**, 122001 (2012) doi:10.1103/PhysRevLett.108.122001 [arXiv:1110.2251 [hep-ex]].

[83] R. Aaij *et al.* [LHCb Collaboration], Phys. Rev. Lett. **112**, no. 22, 222002 (2014) doi:10.1103/PhysRevLett.112.222002 [arXiv:1404.1903 [hep-ex]].

[84] C. Baglin *et al.* [R704 and Annecy(LAPP)-CERN-Genoa-Lyon-Oslo-Rome-Strasbourg-Turin Collaborations], Phys. Lett. B **171**, 135 (1986). doi:10.1016/0370-2693(86)91013-0

[85] T. A. Armstrong *et al.* [E760 Collaboration], Phys. Rev. Lett. **68**, 1468 (1992). doi:10.1103/PhysRevLett.68.1468

[86] C. Patrignani *et al.* [FNAL-E835 Collaboration], AIP Conf. Proc. **717**, 581 (2004) [Nucl. Phys. Proc. Suppl. **142**, 98 (2005)]. doi:10.1016/j.nuclphysbps.2005.01.017

[87] M. F. M. Lutz *et al.* [PANDA Collaboration], arXiv:0903.3905 [hep-ex].

[88] P. Spiller and G. Franchetti, Nucl. Instrum. Meth. A **561**, 305 (2006). doi:10.1016/j.nima.2006.01.043

[89] M. Ablikim *et al.* [BESIII Collaboration], Phys. Rev. Lett. **111**, no. 24, 242001 (2013) doi:10.1103/PhysRevLett.111.242001 [arXiv:1309.1896 [hep-ex]].

[90] R. Mizuk *et al.* [Belle Collaboration], Phys. Rev. D **78**, 072004 (2008) doi:10.1103/PhysRevD.78.072004 [arXiv:0806.4098 [hep-ex]].

[91] J. P. Lees *et al.* [BaBar Collaboration], Phys. Rev. D **85**, 052003 (2012) doi:10.1103/PhysRevD.85.052003 [arXiv:1111.5919 [hep-ex]].

[92] K. Chilikin *et al.* [Belle Collaboration], Phys. Rev. D **90**, no. 11, 112009 (2014) doi:10.1103/PhysRevD.90.112009 [arXiv:1408.6457 [hep-ex]].

[93] Z. Q. Liu *et al.* [Belle Collaboration], Phys. Rev. Lett. **110**, 252002 (2013) doi:10.1103/PhysRevLett.110.252002 [arXiv:1304.0121 [hep-ex]].

[94] M. Ablikim *et al.* [BESIII Collaboration], Phys. Rev. Lett. **110**, 252001 (2013) doi:10.1103/PhysRevLett.110.252001 [arXiv:1303.5949 [hep-ex]].

[95] M. Ablikim *et al.* [BESIII Collaboration], Phys. Rev. Lett. **112**, no. 2, 022001 (2014) doi:10.1103/PhysRevLett.112.022001 [arXiv:1310.1163 [hep-ex]].

[96] A. Esposito, A. L. Guerrieri, F. Piccinini, A. Pilloni and A. D. Polosa, Int. J. Mod. Phys. A **30**, 1530002 (2015) doi:10.1142/S0217751X15300021 [arXiv:1411.5997 [hep-ph]].

[97] X. Liu, Z. G. Luo and Z. F. Sun, Phys. Rev. Lett. **104**, 122001 (2010) doi:10.1103/PhysRevLett.104.122001 [arXiv:0911.3694 [hep-ph]].

[98] J. Ferretti, G. Galatà and E. Santopinto, Phys. Rev. C **88**, no. 1, 015207 (2013) doi:10.1103/PhysRevC.88.015207 [arXiv:1302.6857 [hep-ph]].

[99] E. J. Eichten, K. Lane and C. Quigg, Phys. Rev. D **69**, 094019 (2004) doi:10.1103/PhysRevD.69.094019 [hep-ph/0401210].

[100] S. L. Olsen [Belle Collaboration], Int. J. Mod. Phys. A **20**, 240 (2005) doi:10.1142/S0217751X05021403 [hep-ex/0407033].

[101] Y. c. Yang, Z. Xia and J. Ping, Phys. Rev. D **81** (2010) 094003 doi:10.1103/PhysRevD.81.094003 [arXiv:0912.5061 [hep-ph]].

[102] E. S. Swanson, Phys. Rept. **429**, 243 (2006) doi:10.1016/j.physrep.2006.04.003 [hep-ph/0601110].

[103] S. Godfrey and S. L. Olsen, Ann. Rev. Nucl. Part. Sci. **58**, 51 (2008) doi:10.1146/annurev.nucl.58.110707.171145 [arXiv:0801.3867 [hep-ph]].

[104] N. A. Tornqvist, Phys. Rev. Lett. **67**, 556 (1991). doi:10.1103/PhysRevLett.67.556

[105] A. E. Bondar, A. Garmash, A. I. Milstein, R. Mizuk and M. B. Voloshin, Phys. Rev. D **84**, 054010 (2011) doi:10.1103/PhysRevD.84.054010 [arXiv:1105.4473 [hep-ph]].

[106] N. Drenska, R. Faccini, F. Piccinini, A. Polosa, F. Renga and C. Sabelli, Riv. Nuovo Cim. **33**, 633 (2010) doi:10.1393/ncr/i2010-10059-8 [arXiv:1006.2741 [hep-ph]].

[107] L. Maiani, A. D. Polosa and V. Riquer, arXiv:0708.3997 [hep-ph].

[108] D. Ebert, R. N. Faustov and V. O. Galkin, Eur. Phys. J. C **58**, 399 (2008) doi:10.1140/epjc/s10052-008-0754-8 [arXiv:0808.3912 [hep-ph]].

[109] A. Ali, C. Hambrock and W. Wang, Phys. Rev. D **85**, 054011 (2012) doi:10.1103/PhysRevD.85.054011 [arXiv:1110.1333 [hep-ph]].

[110] G. 't Hooft, G. Isidori, L. Maiani, A. D. Polosa and V. Riquer, Phys. Lett. B **662**, 424 (2008) doi:10.1016/j.physletb.2008.03.036 [arXiv:0801.2288 [hep-ph]].

[111] L. Maiani, F. Piccinini, A. D. Polosa and V. Riquer, Phys. Rev. D **89**, 114010 (2014) doi:10.1103/PhysRevD.89.114010 [arXiv:1405.1551 [hep-ph]].

[112] S. Dubynskiy and M. B. Voloshin, Phys. Lett. B **666**, 344 (2008) doi:10.1016/j.physletb.2008.07.086 [arXiv:0803.2224 [hep-ph]].

[113] K. Gottfried, Phys. Rev. Lett. **40**, 598 (1978).

[114] G. Bhanot, W. Fischler and S. Rudaz, Nucl. Phys. B **155**, 208 (1979).

[115] M. E. Peskin, Nucl. Phys. B **156**, 365 (1979).

[116] G. Bhanot and M. E. Peskin, Nucl. Phys. B **156**, 391 (1979).

[117] M. B. Voloshin, Nucl. Phys. B **154**, 365 (1979).

[118] M. B. Voloshin and V. I. Zakharov, Phys. Rev. Lett. **45**, 688 (1980).

[119] Y. P. Kuang and T. M. Yan, Phys. Rev. D **24**, 2874 (1981). doi:10.1103/PhysRevD.24.2874

[120] Y. P. Kuang, Front. Phys. China **1**, 19 (2006) doi:10.1007/s11467-005-0012-6 [hep-ph/0601044].

[121] J. Segovia, F. Fernandez and D. R. Entem, arXiv:1507.01607 [hep-ph].

[122] K.-F. Chen *et al.* [Belle Collaboration], Phys. Rev. D **82**, 091106 (2010) doi:10.1103/PhysRevD.82.091106 [arXiv:0810.3829 [hep-ex]].

[123] A. Ali, C. Hambrock, I. Ahmed and M. J. Aslam, Phys. Lett. B **684**, 28 (2010) doi:10.1016/j.physletb.2009.12.053 [arXiv:0911.2787 [hep-ph]].

[124] D. Santel *et al.* [Belle Collaboration], arXiv:1501.01137 [hep-ex].

[125] Q. He *et al.* (CLEO Collaboration), Phys. Rev. Lett. **101**, 192001 (2008).

[126] J. P. Lees *et al.* (BaBar Collaboration), Phys. Rev. D **84**, 092003 (2011).

[127] U. Tamponi *et al.* (Belle Collaboration), Phys. Rev. D **87**, 011104 (2013).

[128] B. Aubert *et al.* (BaBar Collaboration), Phys. Rev. D **78**, 112002 (2008).

[129] U. Tamponi, EPJ Web Conf. **70**, 00034 (2014). doi:10.1051/epjconf/20147000034

[130] J. Segovia, D. R. Entem and F. Fernández, Phys. Rev. D **91**, no. 1, 014002 (2015) doi:10.1103/PhysRevD.91.014002 [arXiv:1409.7079 [hep-ph]].

[131] Y. A. Simonov and A. I. Veselov, Phys. Rev. D **79**, 034024 (2009) doi:10.1103/PhysRevD.79.034024 [arXiv:0804.4635 [hep-ph]].

[132] Y. A. Simonov and A. I. Veselov, Phys. Lett. B **671**, 55 (2009) doi:10.1016/j.physletb.2008.12.001 [arXiv:0805.4499 [hep-ph]].

[133] Y. A. Simonov and A. I. Veselov, arXiv:0806.2919 [hep-ph].

[134] Y. A. Simonov, Phys. Atom. Nucl. **71**, 1048 (2008) doi:10.1134/S1063778808060094 [arXiv:0711.3626 [hep-ph]].

[135] C. Meng and K. T. Chao, Phys. Rev. D **77**, 074003 (2008) doi:10.1103/PhysRevD.77.074003 [arXiv:0712.3595 [hep-ph]].

[136] F. K. Guo, C. Hanhart and U. G. Meissner, Phys. Rev. Lett. **105**, 162001 (2010) doi:10.1103/PhysRevLett.105.162001 [arXiv:1007.4682 [hep-ph]].

[137] E.Eicthen, talk given at the "BelleII theory interface platform", Krakow (2015).

[138] D. Y. Chen, X. Liu and T. Matsuki, Phys. Rev. D **87**, no. 9, 094010 (2013) doi:10.1103/PhysRevD.87.094010 [arXiv:1304.0372 [hep-ph]].

[139] S. Godfrey and J. L. Rosner, Phys. Rev. D **64**, 074011 (2001) [Phys. Rev. D **65**, 039901 (2002)] doi:10.1103/PhysRevD.64.074011, 10.1103/PhysRevD.65.039901 [hep-ph/0104253].

[140] S. Godfrey and J. L. Rosner, Phys. Rev. D **66**, 014012 (2002) doi:10.1103/PhysRevD.66.014012 [hep-ph/0205255].

[141] I. Adachi *et al.* (Belle Collaboration), Phys. Rev. Lett. **108**, 032001 (2012).

[142] R. Mizuk *et al.* (Belle Collaboration), Phys. Rev. Lett. **109**, 232002 (2012).

[143] D. -Y. Chen, X. Liu and T. Matsuki, Phys. Rev. D **87**, 094010 (2013).

[144] G. Aarts, C. Allton, T. Harris, S. Kim, M. P. Lombardo, S. M. Ryan and J. I. Skullerud, JHEP **1407**, 097 (2014) doi:10.1007/JHEP07(2014)097 [arXiv:1402.6210 [hep-lat]].

[145] R. J. Dowdall *et al.* [HPQCD Collaboration], Phys. Rev. D **85**, 054509 (2012) doi:10.1103/PhysRevD.85.054509 [arXiv:1110.6887 [hep-lat]].

[146] S. Meinel, Phys. Rev. D **82**, 114502 (2010) doi:10.1103/PhysRevD.82.114502 [arXiv:1007.3966 [hep-lat]].

[147] T. Burch *et al.*, Phys. Rev. D **81**, 034508 (2010) doi:10.1103/PhysRevD.81.034508 [arXiv:0912.2701 [hep-lat]].

[148] T. Wei-Zhao, C. Lu, Y. You-Chang and C. Hong, Chin. Phys. C **37**, 083101 (2013) doi:10.1088/1674-1137/37/8/083101 [arXiv:1308.0960 [hep-ph]].

[149] S. N. Gupta, J. M. Johnson, W. W. Repko and C. J. Suchyta, III, Phys. Rev. D **49**, 1551 (1994) doi:10.1103/PhysRevD.49.1551 [hep-ph/9312205].

[150] S. F. Radford and W. W. Repko, Phys. Rev. D **75**, 074031 (2007) doi:10.1103/PhysRevD.75.074031 [hep-ph/0701117].

[151] B. A. Kniehl, A. A. Penin, A. Pineda, V. A. Smirnov and M. Steinhauser, Phys. Rev. Lett. **92**, 242001 (2004) [Phys. Rev. Lett. **104**, 199901 (2010)] doi:10.1103/PhysRevLett.92.242001 [hep-ph/0312086].

[152] G. Bonvicini *et al.* [CLEO Collaboration], Phys. Rev. D **81**, 031104 (2010) doi:10.1103/PhysRevD.81.031104 [arXiv:0909.5474 [hep-ex]].

[153] B. Aubert *et al.* [BaBar Collaboration], Phys. Rev. Lett. **101**, 071801 (2008) [Phys. Rev. Lett. **102**, 029901 (2009)] doi:10.1103/PhysRevLett.101.071801 [arXiv:0807.1086 [hep-ex]].

[154] B. Aubert *et al.* [BaBar Collaboration], Phys. Rev. Lett. **103**, 161801 (2009) doi:10.1103/PhysRevLett.103.161801 [arXiv:0903.1124 [hep-ex]].

[155] M. Benayoun, S.I. Eidelman, V.N. Ivanchenko, Z.K. Silagadze, Mod. Phys. Lett. A **14**, 2605 (1999).

[156] G. C. Fox and S. Wolfram, Nucl. Phys. B **149** (1979) 413 [Nucl. Phys. B **157** (1979) 543]. doi:10.1016/0550-3213(79)90003-8

[157] J. R. Ellis, M. K. Gaillard and G. G. Ross, Nucl. Phys. B **111**, 253 (1976) [Nucl. Phys. B **130**, 516 (1977)]. doi:10.1016/0550-3213(76)90542-3

[158] E. Farhi, Phys. Rev. Lett. **39**, 1587 (1977). doi:10.1103/PhysRevLett.39.1587

[159] S. Y. Pi, R. L. Jaffe and F. E. Low, Phys. Rev. Lett. **41**, 142 (1978). doi:10.1103/PhysRevLett.41.142

[160] A. De Rujula, J. R. Ellis, E. G. Floratos and M. K. Gaillard, Nucl. Phys. B **138**, 387 (1978). doi:10.1016/0550-3213(78)90388-7

[161] H. Georgi and M. Machacek, Phys. Rev. Lett. **39**, 1237 (1977). doi:10.1103/PhysRevLett.39.1237

[162] G. C. Fox and S. Wolfram, Phys. Rev. Lett. **41**, 1581 (1978). doi:10.1103/PhysRevLett.41.1581

[163] T. Junk, Nucl. Instrum. Meth. A **434**, 435 (1999).

[164] A. Read, J. Phys. G: Nucl. Part. Phys. **28**, 2693 (2002).

[165] R. Brun and F. Rademakers, Nucl. Instrum. Meth. A **389**, 81 (1997). doi:10.1016/S0168-9002(97)00048-X

[166] D. J. Lange, Nucl. Instrum. Meth. A **462**, 152 (2001). doi:10.1016/S0168-9002(01)00089-4

[167] T. Sjostrand, S. Mrenna and P. Z. Skands, JHEP **0605**, 026 (2006) doi:10.1088/1126-6708/2006/05/026 [hep-ph/0603175].

[168] E. Barberio, Z. Waş, Comput. Phys. Commun. **79**, 291 (1994).

[169] R. Brun, F. Bruyant, M. Maire, A. C. McPherson and P. Zanarini, CERN-DD-EE-84-1.

[170] B. Andersson, G. Gustafson, G. Ingelman and T. Sjostrand, Phys. Rept. **97**, 31 (1983). doi:10.1016/0370-1573(83)90080-7

[171] T. Sjostrand, Phys. Lett. B **142**, 420 (1984). doi:10.1016/0370-2693(84)91354-6

[172] B. Andersson, Camb. Monogr. Part. Phys. Nucl. Phys. Cosmol. **7**, 1 (1997).